Synthesis and Characterization of Magnesium and Manganese Doped $LiCoO_2$

by

Aaron Liu

Submitted in partial fulfilment of the requirements
for the degree of Master of Science

at

Dalhousie University
Halifax, Nova Scotia
July 2017

To the ones who push me to be better, to the one who saves.

Table of Contents

List of Tables

List of Figures

Abstract

$LiCo_{1-2x}Mg_xMn_xO_2$ ($0 \leq x \leq 0.05$) positive electrode materials were prepared from $Co_{1-2x}Mg_xMn_x(OH)_2$ ($0 \leq x \leq 0.05$) co-precipitated precursor materials by mixing precursor materials with Li_2CO_3 and heating. All precursor and lithiated materials were characterized by Scanning Electron Microscopy, X-ray Diffraction (XRD), Inductively Coupled Plasma – Optical Emissions Spectroscopy, in situ XRD, and electrochemical testing.

Increasing Mg/Mn content in the material was found to slightly increase the 1st charge capacity, decrease the 1st discharge capacity, and increase the 1st cycle irreversible capacity when cycling up to 4.7 V, likely due to oxygen loss at high voltage. Cells with even 1% Mg/Mn doping were shown to have markedly improved cycling performance, but cells with higher Mg/Mn content did not further improve cycling performance. Results suggest that the cycling improvements stem from suppressing the cell resistance growth and not from the suppression of the O3-O6-O1 phase transitions at high voltage.

List of Abbreviations and Symbols Used

a,b,c	Unit Cell Lattice Parameters
atm	Standard Atmosphere
BMF	Propylene Blown Microfiber Separator (3M)
BOC	Bottom of Charge
C. Cap.	Charge Capacity
C/n	C-rate, where n is the hours needed to fully charge
CCD	Charge Coupled Device
CSTR	Continuously Stirred Tank Reactor
d	Atomic Plane Spacing
D. Cap.	Discharge Capacity
DEC	Diethyl Carbonate
DW	Debye-Waller Factor
EC	Ethylene Carbonate
EV	Electric Vehicle
F	Geometric Structure Factor
f_n	Scattering Factor for the atom n
(h,k,l)	Miller Indices

ICP-OES	Inductively Coupled Plasma Optical Emission Spectrometry
Irrev. Cap.	Irreversible Capacity
L	Lorentz Factor
LCO	$LiCoO_2$
LFP	$LiFePO_4$
LMO	$LiMn_2O_4$
M	Multiplicity of (h,k,l) planes, or Molecular Weight of the Formula Unit
Moli	E-One Moli Energy Limited Canada
N	Number of Formula Units per Unit Cell
NCA	$Li[Ni_xCo_yAl_{1-x-y}]O_2$
NMC	$Li[Ni_xMn_xCo_{1-2x}]O_2$
NMP	N-methyl-2-pyrrolidone
P	Polarization Factor
PVDF	Polyvinylidene Fluoride
q	Capacity
r	ionic radius
R_B	Bragg R-factor
Rel. D. Cap.	Relative Discharge Capacity
S	Scale Factor

SEI	Solid Electrolyte Interface
SEM	Scanning Electron Microscopy
TOC	Top of Charge
UCV	Upper Cutoff Voltage
US DOE	United States Department of Energy
USD	United States Dollar
V	Voltage, or Unit Cell Volume
XRD	X-Ray Diffraction
Z	Atomic Number
ΔV_{TOC}	Voltage change at top of charge
θ	Scattering Angle
θ_m	Angle between monochromator and the diffracted beam
λ	Wavelength
μ_{Li}^{n}	Change of the free energy of the negative electrode with lithium content
μ_{Li}^{p}	Change of the free energy of the positive electrode with lithium content

Acknowledgements

First and foremost, I would like to thank my supervisor Dr. Jeff Dahn for his guidance, feedback, and insights. The opportunities I got here in this lab and in Halifax have produced many valuable learning experiences. I am thankful for my co-op supervisors at Moli for sparking my interest in this field and pointing me to Jeff. I would like to thank my other committee member Dr. Mark Obrovac for providing feedback on my work and this thesis.

Many thanks go to the Dahn lab group for the great working environment. My gratitude goes to Stephen Glazier for all his help at the beginning and throughout this work, and to Jim Li and Ramesh Shunmugasundaram for their collaborations and discussions on positive electrode materials. I would also like to thank Robbie Sanderson, David Stevens, and Jessie Harlow for keeping the lab and network going smoothly.

I would like to thank Simon Trussler for his assistance with the cell crimper and in situ XRD cells, and Andy George, Gordon Hall, Susan Batchilder, and Alicia Oickle for their support with SEM and ICP-OES experiments. I would also like to thank Giselle Andrews for all the administrative support throughout this program.

I would like to thank my ultimate and church community and friends who helped keep my life balanced. To my girlfriend Catherine and my one big family, I am thankful for all the love and support you provide. Finally, to the one who saves, I am eternally grateful for the light shining on my path.

Chapter 1 – Introduction

This chapter will provide an introduction to relevant topics involved in, as well as set the stage for, the studies included in this work. To begin, this chapter will detail the motivation behind this research (Section 1.1). Next, an introduction to lithium ion batteries (Section 1.2) and positive electrode materials (Section 1.3) will be given. In Section 1.4, the focus will be on lithium cobalt oxide and studies looking at increasing the upper cutoff voltage (UCV) to increase energy density. With the stage set, Section 1.5 will detail the aim and outline of this work.

1.1 Motivation to Study Lithium Ion Battery Technology

One aspect of reducing greenhouse gas emissions is to decrease the reliance of fossil fuels in transportation. In 2012, the US announced the *EV Everywhere* Grand Challenge, aiming to encourage the development and mass adoption of electric vehicle (EV) technology and reduce dependence on foreign oil as well as greenhouse gas emissions. In order to meet objectives, the US Department of Energy (DOE) set a target for battery technology to cost 125USD/kWh with a specific energy of 250 Wh/kg and an energy density of 400 Wh/L by the year 2022.[1,2] In addition, the resilience of the battery pack to last through most of the EV's lifetime is important, so battery packs should last upwards of 10 years and thousands of cycles.

Traditionally, lithium ion (Li-ion) batteries have been used to power cell phones, laptops, power tools, and other portable electronics. The intensified attention on energy storage solutions for renewable energy and electric vehicle battery technology, combined with the increasing capabilities of Li-ion batteries, has shone a spotlight on Li-ion batteries as a frontrunner technology to fit both requirements. The implementation and growth of Li-ion battery technology for both energy storage and for electric vehicles has accelerated, but it remains on the cusp of mass adoption due to limitations in capabilities and cost.

Panasonic's NCR18650G 3600mAh Li-ion cell[3] (batteries refer to a set of connected cells) has a specific energy of ~265 Wh/kg and an energy density of ~760 Wh/L, which may seem like it has already surpassed the US DOE 2022 targets. However, the targets are for complete battery packs, which contain complex systems to monitor cells, control operations, and ensure the performance and safety of the battery packs.[4] Any and all additions in the battery pack that are not part of a cell will decrease both the specific energy and the energy density. Currently, battery packs cost as low as 227USD/kWh,[5] with claims and projections (with the right plant design) of less than 190USD/kWh.[6,7]

With an ever-increasing demand for energy, battery manufacturers and researchers constantly look for ways to increase the energy density while maintaining a long lifetime. Other areas of Li-ion battery research include improving the safety and reducing the costs of the technology. The Tesla Model S can already go more than 400 km per charge, and the Model 3 will get 345 km per charge,[8] which will be suitable for most consumer requirements. Figure 1.1 shows the straight line round trip driving range of a fully charged Tesla Model 3 in Halifax. However, any improvements from the mentioned areas of focus will make the product more attractive, bringing EV technology closer to widespread use. Improved energy density of Li-ion cells will decrease the number of cells needed in the battery pack, allowing for more EVs to be manufactured with the same number of cells. Longer cell lifetimes lead to better warranties and product reliability, as do safety improvements. Reducing the cost of cells will allow for lower pricing of EVs, which is a main concern for many consumers.

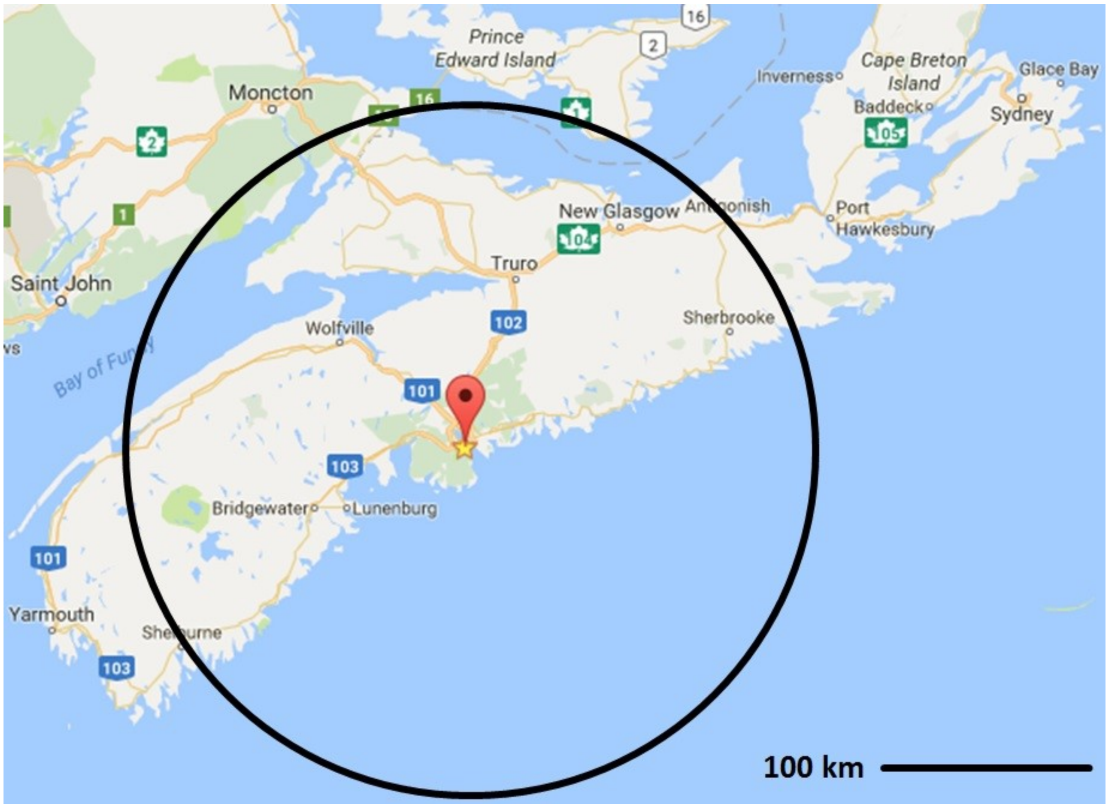

Figure 1.1: Round trip driving range for a fully charged Tesla Model 3 starting in Halifax. Only the distance was used in the determination of this driving range, roads and driving surfaces were not taken into account.[8,9]

1.2 Lithium-ion Batteries

Li-ion cells contain 4 main components: the positive electrode, the negative electrode, the separator, and the electrolyte. The positive electrodes are coated double sided on aluminum foil and negative electrodes are coated double sided on copper foil, the foils serving as current collectives for the electrodes. The electrodes are then rolled or stacked together in a "jelly roll" manner in between layers of the separator and placed in the cell. Separators are usually a thin, porous polyolefin film and are electronic insulators. When filled with electrolyte, separators allow Li^+ ions, but not electrons, to travel in between electrodes. The exact jelly roll shape and dimensions will depend on the cell type that it is placed in, which include cylindrical (like the Panasonic cell mentioned previously), pouch, prismatic, and coin cells.[4] An electrolyte solution is then injected into the cell before the cell is sealed to prevent exposure to ambient atmosphere.

Figure 1.2 shows a schematic of $LiCoO_2$/graphite Li-ion cell operation. During cell operation, Li^+ ions and electrons are reversibly inserted and removed from the electrode materials, in a process called intercalation or deintercalation, respectively. When the cell is being charged, Li^+ ions are deintercalated from the positive electrode and intercalated into the negative electrode. When the cell is charging, a current is applied to the cell and Li^+ ions move through the electrolyte and separator to the negative electrode, with an equal amount of electrons moving through the external circuit. The cell discharges when a load is connected, and then the Li^+ ions spontaneously deintercalate from the negative electrode and reintercalate back into the positive electrodes while the corresponding electron current flows through the circuit, doing work.

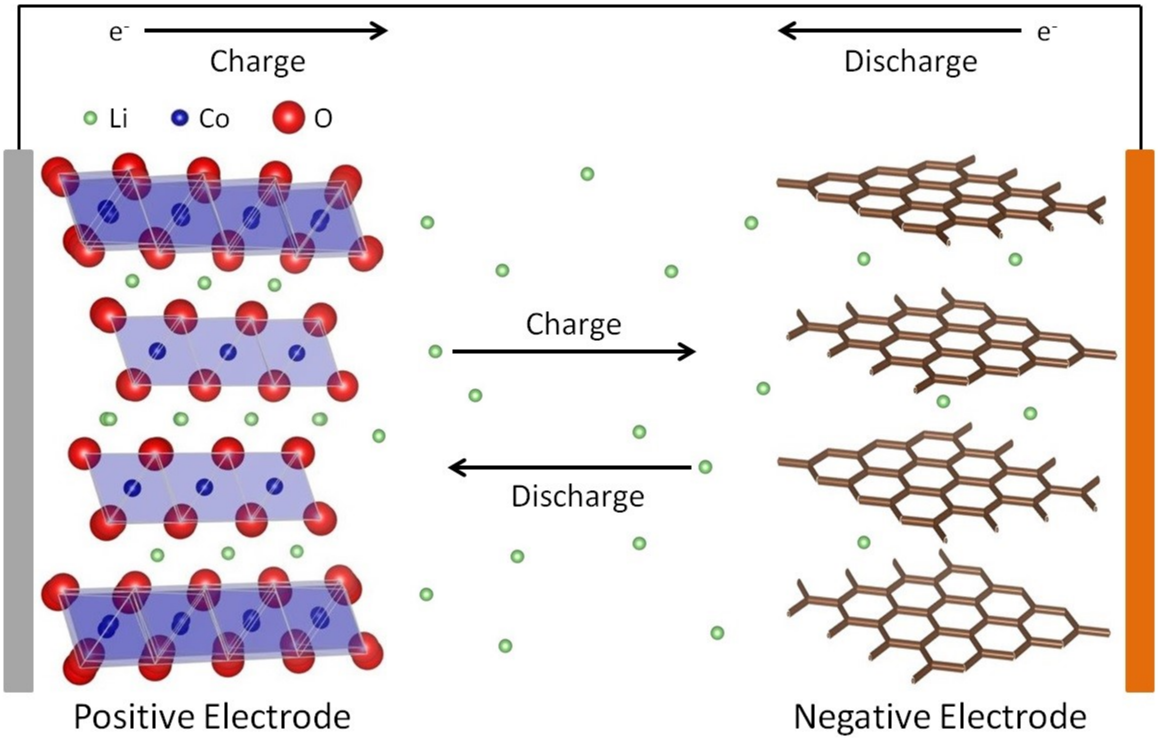

Figure 1.2: Schematic of a Li-ion cell with a $LiCoO_2$ positive electrode and a graphite negative electrode on charge and discharge. The electrolyte and separator are omitted for simplicity.

The processes occurring while the cell shown in Fig. 1.2 is operating are given by the following equations:

Positive electrode:
$$LiCoO_2 \underset{discharge}{\overset{charge}{\rightleftarrows}} Li_{(1-x)}CoO_2 + xLi + xe^- \tag{1.1}$$

Negative electrode:
$$yC + xLi + xe^- \underset{discharge}{\overset{charge}{\rightleftarrows}} yLi_{\frac{x}{y}}C \tag{1.2}$$

Overall cell:
$$LiCoO_2 + yC \underset{discharge}{\overset{charge}{\rightleftarrows}} Li_{(1-x)}CoO_2 + yLi_{\frac{x}{y}}C, \tag{1.3}$$

where x and y are selected based on the molar capacity of the two electrode materials.[4] Equations 1.1-3 assume that no Li^+ ions or electrons are consumed in other processes and that there is only ever one phase at each electrode. Neither assumptions are realistic and will be discussed later.

The difference in chemical potential with respect to lithium content between the positive electrode and negative electrode gives rise to a potential difference between the electrodes, given by

$$V = -\frac{\mu_{Li}^{p} - \mu_{Li}^{n}}{F}, \tag{1.4}$$

where F is the Faraday constant and μ_{Li}^{p} and μ_{Li}^{n} is the change of the free energy of the positive and negative electrode with lithium content, respectively. However, the chemical potentials of the two electrodes vary depending on the material and lithium content in the material. Figure 1.3 shows a typical voltage versus capacity curve of the cell shown in Fig. 1.2 during charging. The $LiCoO_2$ (LCO) and graphite curves were plotted using Li metal foil as the counter and reference electrode. Cells that use Li metal as one electrode are known as half cells. Half cells are useful for evaluating only one electrode material at a time, as the process that occurs on the Li metal foil occurs at a constant potential.

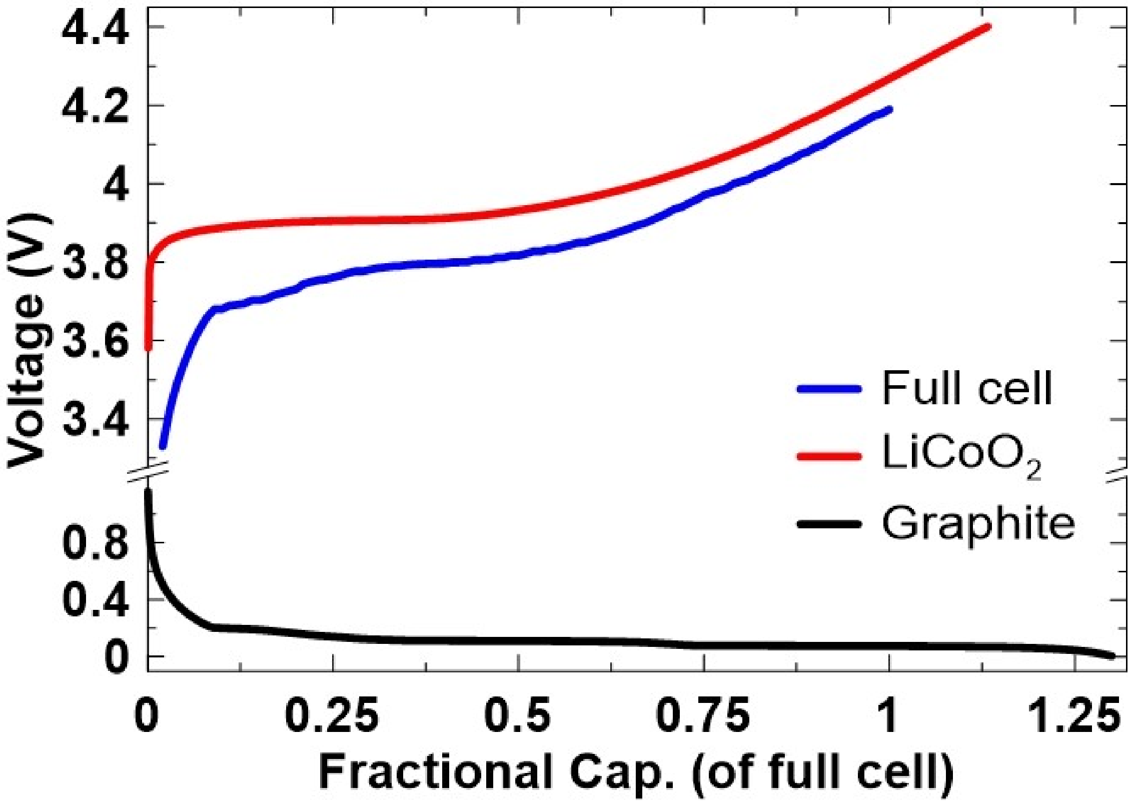

Figure 1.3: Voltage versus capacity (normalized to the full cell capacity) plots of $LiCoO_2$ and graphite half cells and a full cell composed of $LiCoO_2$ and graphite. Half cells are assembled using Li foil as the counter/reference electrode.

Besides LCO, there are many different materials that can function as the positive electrode. This will be discussed the next section. Likewise, there are other negative electrode materials other than graphite. Graphite is the most common negative electrode material due to its low cost, long lifetime, and good energy density. However, it can only accommodate 1 Li atom for every 6 carbon atoms, so attention has been given to other compounds, such as silicon or tin, which can alloy more Li per atom, dramatically increasing theoretical capacity. The increased capacity comes with a drawback though, and the alloys swell to a much larger size than the unalloyed material. The repeated swelling and shrinking of the material can be detrimental to the lifetime of the electrode. Graphite will also swell and shrink slightly, but not to the extent of silicon or tin.

Interestingly, lithiated graphite, and most other negative electrode materials, are not stable in the electrolyte at the voltage ranges of cell operation. Fortunately, initial reactions form a passivating layer on the surface of the electrode, shielding the electrode from further reaction, much like an oxide passivation layer for many metals, but still allowing Li to diffuse through.[10–12] This passivating layer is called the solid electrolyte interface (SEI). It is known that SEI formation will consume electrolyte and contribute to irreversible capacity (Li is consumed and can no longer contribute to cell operation) both in the beginning and throughout the lifetime of the cell. Additionally, the type of electrolyte can influence the makeup of the SEI, and strategic use of electrolyte additives can form SEI species that benefit the lifetime of the cell.[13–17]

As seen in Fig. 1.3, the full cell voltage is very dependent on the voltage of the positive electrode if graphite is chosen as the negative electrode. While increasing the voltage is an effective method of increasing the energy density of the cell, there are often detrimental consequences to the lifetime of the cell when operating at a higher voltage. Research focused on trying to increase the voltage of cells will invariably have to involve evaluating positive electrode materials. This will be discussed in more detail later in this chapter.

1.3 Positive Electrode Materials

In the previous section, LCO was referred to as the positive electrode. However, the positive electrode actually contains several different components. LCO takes on the role of the active material, which participates in the electrochemical operation of the cell. Other components in the electrode include the binder and the conductive agent. Binders, such as polyvinylidene fluoride (PVDF), help keep the electrode materials adhered to the current collector after coating. Conductive agents, such as carbon black, provide a connected network which enhances the conductivity of the electrode. The use of binders and conductive agents also occur in the negative electrode, although some materials, such as graphite, are conductive already and do not require conductive agents.

The active material is where a lot of the attention focuses concerning the positive electrode. Positive electrode active materials need to reversibly accommodate the insertion/extraction of Li at a chemical potential lower than the negative electrode. Other considerations include the amount of Li the material can accommodate (capacity), the number of times the material can accommodate the repeated process (cycle life), material properties (density, safety and Li diffusion rate), and cost of the materials including synthesis and processing steps.

This section will first discuss LCO (Section 1.3.1), the material involved in this work, before discussing some other positive electrode materials (Section 1.3.2) that are used in Li-ion cells.

1.3.1 Lithium Cobalt Oxide (LCO)

Lithium cobalt oxide was demonstrated to be a good candidate as a positive electrode material by the Goodenough group in 1980.[18,19] The first commercial Li-ion batteries from Sony utilized LCO as the positive electrode,[20] and LCO continues to have a strong market presence today (27% of market share as of 2015).[21]

Figure 1.4 shows the structure of LCO. LCO is a layered structure with the rhombohedral $R\bar{3}m$ space group,[18,22] with Li, Co, and O all arranged into separate layers with the Li located in between layers of CoO_2 (shown by the shaded polyhedra in Fig. 1.4).

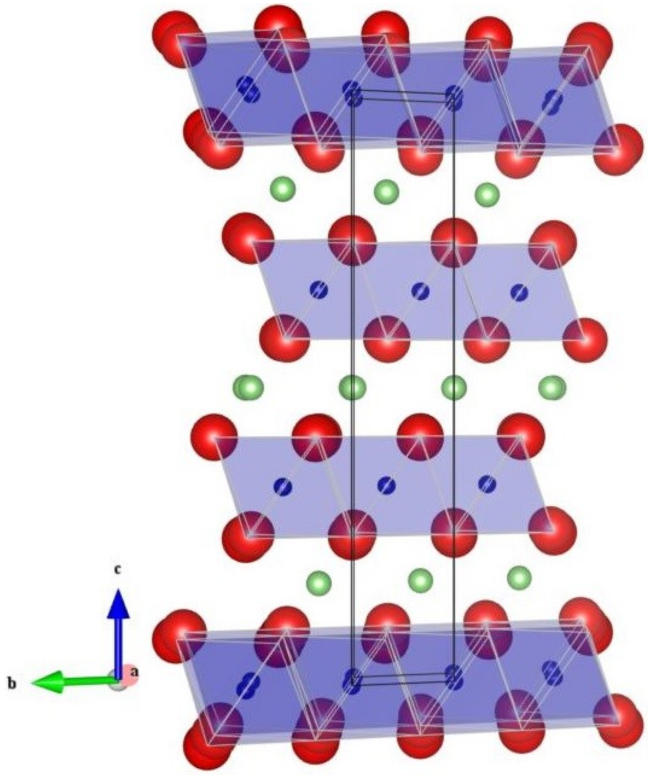

Figure 1.4: Structure of the $LiCoO_2$ layered material. Lithium atoms are represented by green spheres, oxygen atoms by red spheres, and cobalt atoms by blue spheres.

LCO has several different structure configurations, and the configuration seen in Fig. 1.4 is known as the O3 structure. This signifies that the Li and Co occupy the octahedral sites and that the unit cell contains 3 layers (usually the CoO_2 layers are counted) before repetition. The diffusion of the Li is two dimensional within the Li layers when the cell is operating. The intercalation/deintercalation of Li in LCO is accommodated by the Co^{+3}/Co^{+4} redox couple.

LCO has been a mainstay positive electrode material since the beginning of the market because of its electrochemical performance, structure, composition, and simple processing. The specific capacity of a material is given by

$$Specific\ Capacity = \frac{nF}{M}, \tag{1.5}$$

where n is the number of Li per formula unit participating in the electrochemical reaction, F is the Faraday constant (using the units Ah/mol), and M is the molar mass. LCO has a theoretical specific capacity of 274 mAh/g if all the Li is utilized. In practicality, LCO rarely goes beyond ~0.7 Li per LCO, which corresponds to a capacity of ~190 mAh/g, because there are drawbacks to the lifetime of the cell, which will be discussed later in this chapter. Still, the widespread documentation of LCO's electrochemical performance, including the ability to cycle reversibly for hundreds of cycles, have contributed to LCO's continued attractiveness as a positive electrode material.[13,20,23–39]

LCO continues to be an attractive positive electrode material for several reasons. Owing to its compact layered structure, the density of LCO is quite high compared to some other positive electrode materials. LCO's high density, when combined with its respectable capacity, results in an electrode material that has a very competitive energy density. Additionally, the synthesis of LCO is generally simple, and can be done by combining powders of a Co source and a lithium source and heating in an oven to an adequately high temperature (this process is known as solid state synthesis).[23,24,27,29,37,40,41]

Unfortunately, the use of LCO in cells also has some drawbacks. The most serious issue with LCO is the thermal instability of the material when charged, especially at higher voltages.[24,42,43] If cells experience an internal short, a large current flows through the short, creating lots of heat. The thermal instability of LCO will lead LCO to react with the electrolyte, causing even more heat to be released uncontrollably. This phenomenon is called thermal runaway, and is the major contributor to safety incidents in Li-ion batteries. The use of coatings, electrolyte additives, or dopants may aid the thermal stability of LCO, but the processing necessary will incur a higher cost.

Another disadvantage of LCO is the use of cobalt. Table 1.1 shows a cost comparison of several metals commonly used in positive electrode materials. Cobalt is very expensive compared to other positive electrode materials. Recently, it has come to light that human rights abuses, including hazardous working conditions and child labour, are occurring in certain parts of the Democratic Republic of Congo, which accounts for more than half of the world's cobalt production in 2016.[44,45] Cobalt is also toxic, and care must be taken during synthesis and processing.

Table 1.1: Cost of some commonly used metals in positive electrode materials.[45,46]

Metal	**Price in 2015[45] (USD/kg)**	**Price in May 2017[46] (USD/kg)**
Aluminum	1.94	1.89
Manganese	N/A	1.97
Iron	0.081	0.095
Cobalt	29.57	54.38
Nickel	11.81	8.98

1.3.2 Other Positive Electrode Materials

Besides layered structures, positive electrode candidate materials also come in the spinel and olivine structures. Most Li-ion positive electrode materials come in the form of Li[Transition Metal]Anion, although not all metals in the transition metal role are actually transition metals. Figure 1.5 shows three common structure schemes and a positive electrode material with that structure. Different structures will influence the energy density, stability and ease of Li diffusion of the material.

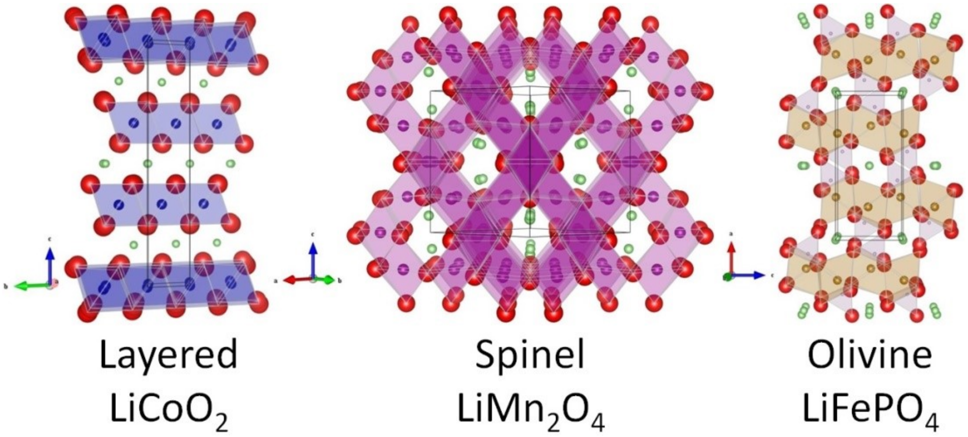

Figure 1.5: Structures of some common positive electrode materials in the layered, spinel, and olivine structure schemes.[18,22,47–49]

With the disadvantages of the Co laid out previously, there has been lots of research on finding alternative metals, usually transition metals, that can replace cobalt but retain the layered structure. The successful replacement of 2 Co^{+3} with Ni^{+2} and Mn^{+4} to form $Li[Ni_xMn_xCo_{1-2x}]O_2$ (NMC) was first demonstrated in 2001[50,51] and have since become a popular positive electrode material (rivalling LCO at 28% of market share as of 2015).[21] Depending on the transition metal ratio of NMC, improvements can be made to the safety, capacity or lifetime, and at a lower cost than LCO.[52–54]

Another layered material in commercial use today is $Li[Ni_xCo_yAl_{1-x-y}]O_2$ (NCA), which has 10% of the market share as of 2015.[21] Research originated from $LiNiO_2$, but it was found that the material has lower thermal stability than even LCO, and also experienced severe capacity fade upon cycling due to nickel migration into the Li layer.[55–57] NCA was then formed from the substitution of Ni with Co to stabilize cycling performance and Al to improve thermal stability.[58–60]

Materials with the spinel structure have the fastest Li diffusion when compared to other structure schemes due to three dimensional Li diffusion. $LiMn_2O_4$ (LMO)[47,61] is often used for power applications which require high current densities (market share of 12% as of 2015).[21] Drawbacks such as short lifetime and middling energy density have lead battery designers to sometimes combine LMO with materials such as NMC.[62,63]

Materials with an olivine structure, such as $LiFePO_4$ (LFP),[64] are very stable and can withstand cycling at room temperature for longer than most other positive electrode materials. Furthermore, olivine materials with iron or manganese as the transition metal have attracted lots of attention due to their low cost (LFP has a market share of 23% as of 2015).[21] One disadvantage of olivine materials is that Li diffusion is slow due because diffusion only occurs in one dimensional tubes. Another disadvantage of olivine materials is a low energy density stemming from bulky phosphate ions.

1.4 Understanding LCO to Increase Energy Density

LCO has been a mainstay positive electrode material since the beginning of the Li-ion battery industry due to its aforementioned energy density and resilience. However, utilizing only about 70% of theoretical capacity means there are still opportunities to increase the energy density of LCO cells. This section will discuss the ongoing progress in efforts to increase the upper cutoff voltage (Section 1.4.1), various approaches to mitigating high voltage performance issues (Section 1.4.2), and more specifically, the use of magnesium as a dopant to improve LCO performance (Section 1.4.3)

1.4.1 Pushing LCO to Higher Upper Cutoff Voltages (UCVs)

Significant improvements have been made since the first commercial LCO batteries were introduced, but commercially available batteries have yet to push LCO electrodes past 4.48 V (vs Li/Li^+), corresponding to the deintercalation/intercalation of ~0.7 Li (per LCO) or a capacity of ~190 mAh/g (out of a theoretical capacity of ~274 mAh/g). In order to unlock more capacity and increase the energy density, the LCO electrodes have to cycle to voltages above 4.5 V (vs Li/Li^+). However, pushing cells with LCO electrodes to an even higher voltage result in a dramatic decrease in long term cycling performance.[13,24,28–30,65,66] There are multiple causes for this drop in performance, including structural instability of highly delithiated LCO,[28–30,67,68] electrolyte oxidation,[13,26,28,29,32,66,67,69] and Co dissolution.[29,30,37,65,66,69,70]

To further understand the structural instability that arises from high voltage cycling, X-ray diffraction (XRD) has been instrumental in studying the unit cell lattice parameter changes and phase transitions.[67,68,71,72] Theoretical work has also confirmed the majority of these phase changes and helped shed light in understanding phases formed at low lithium content.[73,74] As Li deintercalates from LCO, the material undergoes a series of phase changes. The first is an insulator-metal transition, resulting in a 2-phase region.[67,71] As deintercalation continues, LCO will undergo an order-disorder transition around 0.5 Li.[71,74] Both of these transitions occur reversibly and are not detrimental to cycling performance. These transitions occur below 4.5 V vs Li/Li^+.

However, as all the lithium deintercalates and cell voltage rises above 4.5 V, LCO shifts from its original O3 structure to an O1 structure.[67,68,72] More in-depth investigation revealed an intermediate phase with an O6 structure as O3 transitions to O1.[72–74] Van der Ven and co-workers calculated that the O6 structure stems from a stage II compound[73,74] (this was confirmed experimentally by Chen *et al.*[72]), allowing a full understanding of the O3-O6-O1 phase transition. As Li delithiates from the O3 structure, the material at low lithium content will preferentially empty out alternating Li layers, and the CoO_2 slabs above and below the empty layer will shift to O1 stacking. Thus, the stage II phase consists of alternating O1 and O3 stacked CoO_2 slabs requiring 6 CoO_2 slabs in the unit cell, hence an O6 structure. The O1 phase forms when the rest of the lithium layers become empty and all the CoO_2 slabs shift to O1 stacking. During these phase transitions, the c lattice of the unit cell contracts sharply. These transitions are quite reversible, but it is suspected that the repeated CoO_2 slab shifting and the resulting unit cell lattice variations contribute to poor cycling performance. Figure 1.6 shows the structures of the O3, O6, and O1 phases. Arrows are included in the figure to help illustrate how CoO_2 slabs are offset in O3 but not in O1, and how the O6 structure includes both aspects.

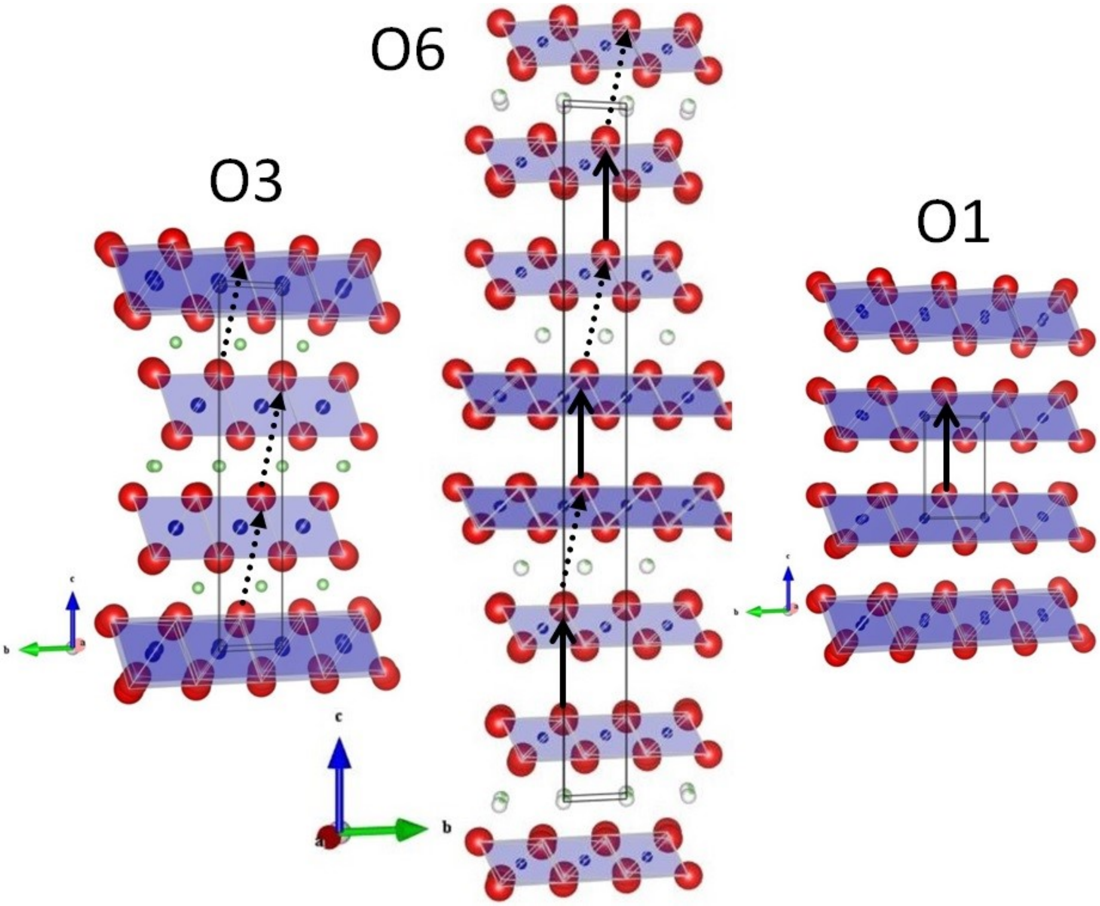

Figure 1.6: Structure of the $LiCoO_2$ material in the O3, O6, and O1 phases. Arrows show how CoO_2 slabs are offset in O3 but not in O1. Lithium atoms are represented by green (or fractionally green) spheres, oxygen atoms by red spheres, and cobalt atoms by blue spheres.

1.4.2 Addressing Performance Issues at Higher UCVs

There have been continual efforts in addressing the issues that LCO experiences when cycled to higher UCVs. Various approaches have been taken, and different approaches have even been combined to look for synergistic benefits. One approach is to cover the LCO particles with a coating to limit electrolyte oxidation and increase structural stability. Coatings have been attempted using oxides,[26,66,70] phosphates,[75,76] and even other positive electrode materials.[24,77] Most, if not all, of the coatings investigated improved LCO cycling, but many studies did not show more than 150 cycles. It is unknown how the coatings benefit LCO cycling beyond 150 cycles, and whether the benefits imparted by coatings offset the extra processing requirements.

The use of electrolyte additives to modify the SEI is another approach. While many additives have been show to improve LCO cycling,[13,32,41,69,78–84] additives only bring about modest improvements. However, only small amounts of additives are needed to improve performance.

Another approach to improving LCO performance involves doping LCO with various metals. These attempts have met varying degrees of success[23,27,31,33,40,85–94] and some dopants did not improve LCO performance, some improved LCO cycling but lowered initial capacity, and results for some metals, like Zr, were contradictory regarding whether they provide benefits.

Some of the most successful attempts to address LCO performance issues used different approaches concurrently. Studies involving the doping of LCO with Mg along with various coatings have shown that the two concurrent approaches performed better than either approach individually.[37–39] Shim *et al.* demonstrated that some Mg dopants diffused into the coating layer during heat treatment, which improved the conductivity of the coating layer and improved Li diffusion.[38] Shim *et al.* took it another step further in

2016, combining electrolyte additives with the synergistic Mg doping and coating with great success.[39] It is likely that the pathway to making LCO viable during high voltage cycling will include combinations of the approaches discussed.

1.4.3 Magnesium Doping to Improve Performance

Of the different metals used to dope positive electrode materials to try to improve cycling performance, Mg has repeatedly come up as a dopant that provides a benefit. Mg, as a dopant, has been shown to improve cycling performance of various positive electrode materials, including $LiNiO_2$,[55–57] NMC,[95–97] and NCA.[60,98–100]

Cycling performance improvements from Mg doping have been shown for LCO as well.[23,27,31,33,37–39,85,88,89] Most studies attribute the improvements in LCO cycling performance to Mg either providing structural stability[33,37,85,88] or improving the conductivity of the material.[23,31,38,39] Recently, Shim *et al.* reported a retention of 85% capacity after 500 cycles and 60% after 700 cycles in 2900mAh prismatic full cells (LCO/graphite) cycling up to 4.4V (4.48V vs Li/Li^+) utilizing a combination of ionic conductor coating, electrolyte additives, and Mg doping mentioned previously.[39]

While much progress has been made for cycling below 4.5 V (vs. Li/Li^+), there are no studies, as far as the author is aware of, on the long term effect of Mg doping on the O3-O6-O1 phase transitions which occur around 4.55 V and 4.63 V (vs. Li/Li^+), respectively.[72] A few studies reporting results for one high voltage cycle showed a suppression of those phase transitions.[85,87] If Mg doping provides structural stability and suppresses the O3-O6-O1 phase transitions, it may be of interest to investigate the long term effects of cycling repeatedly through these transitions.

Additionally, while doping LCO with Mg has been shown to provide performance benefits, it has been noted that the substitution of Mg leads to the creation of Co^{+4} ions[23,87,101] or oxygen deficiencies[85,86,89] in the synthesized material. Manganese is a common positive electrode metal, and have been used in the past as Mn^{+4} along with Ni^{+2} to replace cobalt and form NMC. Doping LCO with equal amounts of Mg^{+2} and Mn^{+4} ions may ease synthesis and focus the investigation on dopant effects.[87,96]

1.5 Scope of This Thesis

The aim of this work was to investigate the effects of Mg and Mn co-doping on LCO cycled through the O3-O6-O1 phase transitions. Of particular interest were how Mg/Mn doping affected the phase transitions and whether these effects on the phase transitions influenced long term cycling performance. Other points of interest included the amount of Mg/Mn doping required to observe differences in electrochemical performance and the behavior of Mg/Mn doped LCO materials across a range of upper cutoff voltages.

$Co_{1-2x}Mg_xMn_x(OH)_2$ ($0 \leq x \leq 0.05$) precursor materials were synthesized by the co-precipitation method and then lithiated to produce $LiCo_{1-2x}Mg_xMn_xO_2$ ($0 \leq x \leq 0.05$). Precursor materials were characterized physically and lithiated materials were physically and electrochemically characterized. In situ X-ray diffraction was performed on certain samples to track electrode material behaviour as cells cycled.

Chapter 2 will discuss the various synthesis and characterization methods and techniques involved in this work. Chapter 3 will discuss the physical characterization of the precursor and lithiated materials as well as the initial electrochemical characterization of the lithiated materials cycling to an upper cutoff voltage of 4.7 V. Chapter 4 will discuss further in-depth investigations of selected materials, cycled either over a range of upper cutoff voltages or in conjunction with X-ray diffraction. Chapter 5 will discuss several miscellaneous studies that arose during the course of this work. Finally, Chapter 6 will summarize the conclusions of this work and identify opportunities for future work.

Chapter 2 – Experimental

Numerous experimental methods and characterization techniques were utilized in this work and this chapter will discuss each procedure. First, the procedures for synthesis of the materials used in this work will be reviewed (Section 2.1) before covering various materials characterization methods. These methods include inductively coupled plasma optical emission spectrometry (ICP-OES, Section 2.2), X-ray diffraction (XRD, Section 2.3), scanning electron microscopy (SEM, Section 2.4), and electrochemical characterization methods (Sections 2.5 and 2.6). Finally, the procedure for in situ XRD experiments will be covered in Section 2.7.

2.1 Synthesis of Mg/Mn doped LCO

LCO can be synthesized using various methods, and several procedures were investigated in Chapter 5. The selected procedure involved the synthesis of $Co_{1-2x}Mg_xMn_x(OH)_2$ ($0 \leq x \leq 0.05$) precursor materials by the co-precipitation method (Section 2.1.1) followed by the lithiation of the synthesized precursors (Section 2.1.2). This method was used to synthesize the samples studied in Chapters 3 and 4. Procedures studied in Chapter 5 were usually variants of procedures discussed in Sections 2.1.1 or 2.1.2, with the exception of a trial synthesis using the continuously stirred tank reactor, which will be discussed in Section 2.1.3.

2.1.1 Synthesis of Precursor Materials by the Co-precipitation Method

$Co_{1-2x}Mg_xMn_x(OH)_2$ ($0 \le x \le 0.05$) precursor materials were synthesized by the co-precipitation method. While the synthesis of LCO via co-precipitation is uncommon due to the existence of simpler processes,[4,102] lithium mixed metal oxides are often prepared by co-precipitation.[4,54,103–109] Co-precipitation synthesis allows for atomic mixing of the metal components before lithium is added by sintering with Li_2CO_3. This method generally involves the slow mixing of an aqueous solution of metal salts with a hydroxide solution, precipitating metal hydroxide precursors out of solution. It is known that co-precipitation in the presence of ammonia produced metal hydroxides that were dense and spherical via a dissolution-recrystallization mechanism and so syntheses in this work were carried out in an ammonia solution.

In this work, aqueous solutions of $Co(NO_3)_2 \cdot 6H_2O$ (Sigma-Aldrich, 98%), $Mg(NO_3)_2 \cdot 6H_2O$ (Sigma-Aldrich, 99%), and $Mn(NO_3)_2 \cdot 4H_2O$ (Sigma-Aldrich, 97%) were prepared in Co:Mg:Mn molar ratios of 100:0:0 to 90:5:5 (0% to 5% Mg/Mn doping). A hydroxide solution and an ammonia solution were also prepared using NaOH (Fisher, 98.9%) and $NH_3(aq)$ (Sigma-Aldrich, 28-30%), respectively. Deionized water, deaerated by boiling, was used to prepare solutions for precursor synthesis as well as for rinsing the precipitate after filtration.

Figure 2.1 shows the experimental setup of a typical co-precipitation synthesis. The mixed solution (100 mL, 1 M) and hydroxide solution (100 mL, 2 M) were simultaneously added dropwise, using peristaltic pumps (Masterflex L/S, 07524 series), to a stirred reaction vessel containing the ammonia solution (100 mL, 1M). The solutions were added over the course of 17 hours using a pump rate of 0.10 mL/min. The reaction vessel was kept around 50°C and N_2 was bubbled into solution to maintain an inert atmosphere.

Figure 2.1: Picture of a typical experimental setup for precursor synthesis by co-precipitation in this work.

After the solutions were completely added into the vessel, the vessel was cooled to room temperature while still stirring. The precipitate was then suction filtered and rinsed four times with water before drying overnight in an oven at 80°C in air. The precursor materials were then weighed and characterized as needed (Sections 2.2-4). Each synthesis batch produced around 9 g of precursor materials after overnight drying.

2.1.2 Preparation of Mg/Mn doped LCO

The process used to lithiate the precursor materials is analogous to the solid state synthesis of LCO used in most industrial manufacturing processes.[102] The precursor materials ($Co_{1-2x}Mg_xMn_x(OH)_2$, $0 \le x \le 0.05$) were mixed with Li_2CO_3 (Alfa Aesar, 99%) in a Li:M ratio of 1.05:1 (M = Co, Mg, Mn) to obtain 5 g of each mixture. The excess Li content was to account for lithium loss during the heating process, and Section 5.3 will discuss a study in which the Li content was varied during the lithiation process. The mixtures were then ground together by mortar and pestle until homogenous. Samples were placed in alumina heating “boats” and heated in a box furnace (Vulcan 3-550) for 10 hours at 900°C. A heating rate of 10°C/min and a cooling rate of 20°C/min were used. After the heating process, lithiated samples ($LiCo_{1-2x}Mg_xMn_xO_2$, $0 \le x \le 0.05$) were weighed and ground once more before characterization.

As mentioned, solid state synthesis is a simple method often used to synthesize LCO[23,24,27,29,37,40,41] and this method was explored in Section 5.1.1. $CoCO_3$ (Alfa Aesar, 99%), $MgCO_3 \bullet xH_2O$ (Sigma Aldrich), and $MnCO_3$ (Sigma Aldrich, 99%) were mixed together in Co:Mg:Mn molar ratios of 100:0:0 to 90:5:5. Li_2CO_3 was then added to the mixture in a Li:M ratio of 1.02:1 (M = Co, Mg, Mn) to obtain 5 g of each mixture. The mixture was then ground, heated, weighed and ground in the same manner as described above.

2.1.3 Precursor Synthesis Using a Continuously Stirred Tank Reactor (CSTR)

Co-precipitation synthesis through the use of a continuously stirred tank reactor (CSTR) allows for a greater degree of control of reaction conditions and has been explored in previous work, mainly for NMC synthesis.[54,103,105–109] Work by Zhou *et al.* showed that parameters such as ammonia content, temperature, pH, and atmosphere of the reaction are all factors influencing hydroxide precursor synthesis.[104] Other factors include reaction time, stir rate, transition metal composition, and concentration.[107,109] In a well-designed CSTR synthesis, most, if not all, of the mentioned factors can be controlled through the use of a system of pumps, mechanical stirrer, pH probe, and thermometer that are all integrated into a graphical programming software. This allows for optimization of the synthesis protocol, producing precursor materials with desired properties.

In this work, only one batch of synthesis (discussed in Chapter 5) was performed due to the large amount of precursor materials produced per batch. Solutions of 2 M $M(NO_3)_2$ (M = Co, Mg, Mn), 10 M NaOH, 5 M $NH_3(aq)$, and 1 M $NH_3(aq)$ were prepared, using deaerated deionized water as necessary. The 1 M $NH_3(aq)$ solution (1 L) was poured into the CSTR, and the other solutions set up for addition via pumps. The NaOH solution was programmed to be added to maintain a set pH, whereas the $M(NO_3)_2$ and 5 M $NH_3(aq)$ solutions were added at a programmed rate. The pH electrode (Mettler-Toledo) was calibrated at room temperature using two buffer solutions (pH 4.0 and 10.0 at 20°C, Fisher Scientific). The CSTR, with the ammonia solution in the vessel, was set up with pumps, stirrer, pH probe, and thermometer. The solution, which was being stirred at 650 rpm, was then heated to 60°C with N_2 bubbling through the solution. When the solution reached the set temperature, the $M(NO_3)_2$ and 5 M $NH_3(aq)$ solutions were added at a rate of 0.5 mL/min and 0.14 mL/min, respectively. The pH range during the synthesis was kept between 9.8 and 10.2. The synthesis proceeded for 18 hours, then the CSTR was allowed to cool to room temperature while still stirring and maintaining the pH range. Similar to Section 2.1.1, the precipitate was then suction filtered, rinsed four times and dried overnight at 80°C in air before precursor materials were weighed and characterized. Figure 2.2 shows the CSTR as well as some of the equipment and software involved in the experiment.

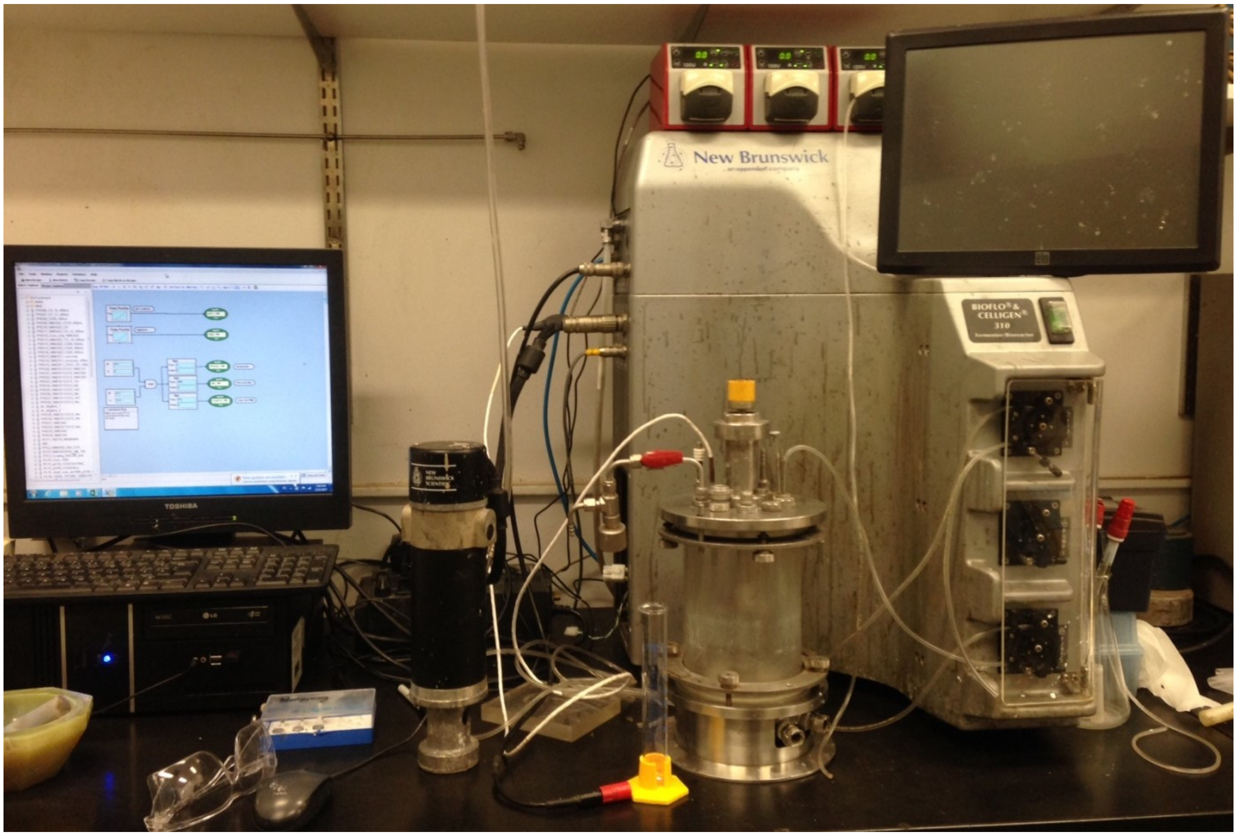

Figure 2.2: Picture of the continuously stirred tank reactor equipment and software.

2.2 Inductively Coupled Plasma Optical Emission Spectrometry (ICP-OES)

Elemental analysis is a technique used to confirm the elemental composition of samples. There are various elemental analysis methods, and ICP-OES measurements were carried out in this work using a Perkin Elmer Optima 8000 ICP-OES Spectrometer (Department of Dentistry, Dalhousie University). ICP-OES is a technique suitable for detecting trace metals and was used to determine metal atomic ratios of samples produced.

In ICP-OES samples are introduced into a high temperature argon plasma and the resulting radiation emitted is measured.[110,111] The dissolved sample (sample preparation described below) is drawn up using an autosampler and transported into a nebulizer. The nebulizer converts the sample into a fine mist which is then introduced directly into the plasma. The argon plasma, with temperatures exceeding 6000 K, then proceeds to cause the sample to undergo a series of processes including desolvation, vaporization, and atomization. The atomized sample then undergoes excitation and/or ionization. The excited atoms and ions emit photons when relaxing to states of lower energy, and these photons are emitted at wavelengths that are characteristic of the element. The emissions are collected by an optical system and sorted by wavelength. The emissions are then detected by charge coupled device (CCD) photodetectors and converted into electronic signals and processed by a program. By measuring the intensity of radiation of a specific wavelength being emitted, the concentration of a sample can be determined with the use of calibration curves.

Sample preparation was performed using Nanopure water (Barnstead Thermo Scientific 18.2 MΩ·cm) and ICP-dedicated glassware to minimize metal contamination for this highly sensitive technique. The standard solutions used to create the calibration curves were prepared from Li, Co, Mg, and Mn ICP-grade standards (1000 µg/mL in water with dilute nitric acid, Ultra Scientific). Standard solutions of 0, 0.5, and 1 µg/mL for Li, Mg, and Mn and 0, 1, and 2 µg/mL for Co were prepared. This was first done by pipetting 1 mL (Li, Mg, Mn) or 2 mL (Co) of the standard into a 1000 mL volumetric flask and filling 2% HNO_3 up to the mark to produce the 1 µg/mL (Li, Mg, Mn) and 2 µg/mL (Co) solution. Half of this solution was then diluted by a factor of 2 to produce the 0.5 µg/mL and 1 µg/mL solution, with the 0 µg/mL blank solution being the 2% HNO_3 in Nanopure water.

8-10 mg of sample was dissolved in 2 mL of aqua regia (1:3 HNO_3:HCl (both reagent grade, Sigma Aldrich)) overnight to ensure thorough digestion. 10 µL aliquots of each dissolved sample were then pipetted into 15 mL polypropylene conical tubes (Falcon) and diluted to 12-14 mL with 2% HNO_3. The 3 solutions used to create the calibration curve (blank, 0.5/1 µg/mL, and 1/2 µg/mL) were poured into 50 mL tubes (Falcon) and a large plastic bottle of 2% HNO_3 was prepared as the wash for the ICP-OES measurements.

ICP-OES results (triplicate measurements with an uncertainty of 2%) were provided in units of mg/L for each element, which were then converted to molarity to determine the metal atomic ratios reported in this work. ICP-OES results for precursor materials were normalized to 1 for the atomic ratios to correspond with the formula unit $M_1(OH)_2$ (M = Co, Mg, Mn). ICP-OES results for lithiated samples were normalized to

2 for the atomic ratios to correspond with the formula unit $Li_xM_yO_2$ ($x + y = 2$, M = Co, Mg, Mn).

2.3 X-ray Diffraction (XRD)

X-rays have wavelengths (λ) in the range of 10 nm to 0.01 nm, which are comparable to the size of atoms. This makes X-rays useful for probing structural arrangements and compositions of materials. X-rays interact with materials in various ways, including elastic scattering, inelastic scattering, and absorption of the X-rays. X-ray diffraction (XRD) is a technique that uses elastic scattering to gain information about the phases present, their structure, and lattice parameters in a sample.

When an X-ray beam probes a sample, the X-ray photons interact with the electrons of the sample.[112,113] Elastic scattering occurs when the ensuing X-ray photons retain the same wavelength, but the momentum changes. Like a wave of water encountering an object, the photons are scattered in all directions. In samples with a periodically repeating arrangement of atoms, which include Li-ion positive electrode materials (Section 1.3) of interest in this work, X-rays are scattered off all the atoms interacting with the X-ray beam. While the majority of the scattered X-rays interfere destructively with each other, constructive interference may occur when the scattered X-rays are in phase.

Figure 2.3 shows a depiction of X-ray diffraction. In order for the two X-rays to remain in phase after diffraction, the extra distance travelled by the lower X-ray must be a multiple of the wavelength.

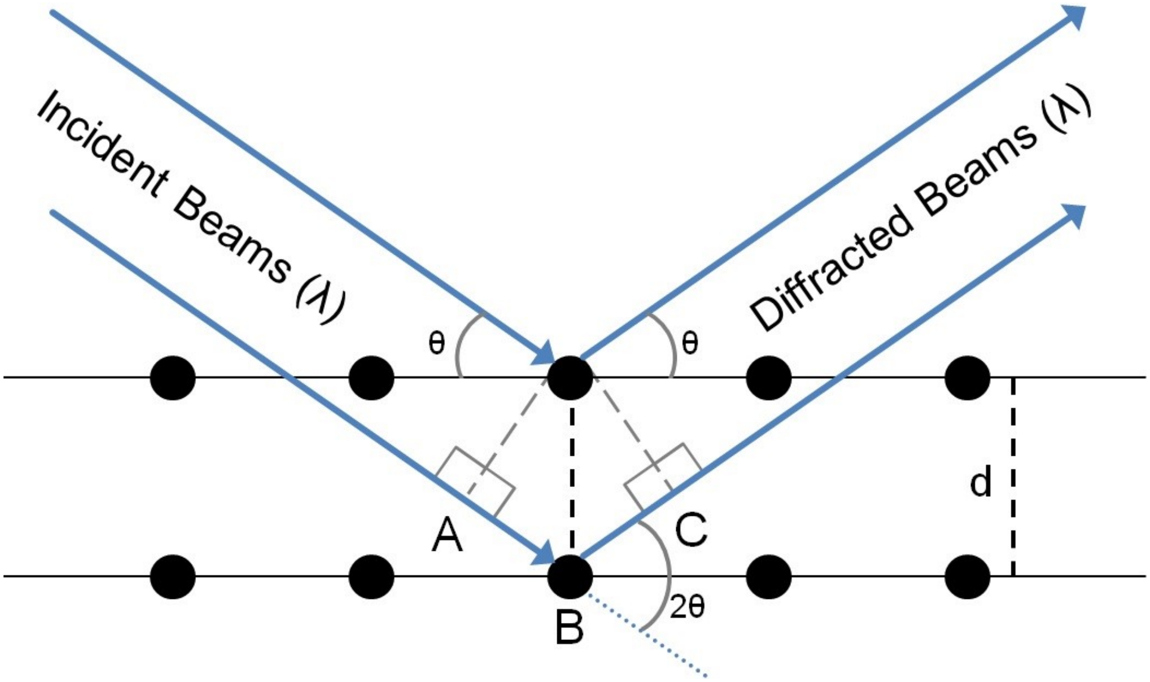

Figure 2.3: A diagram of X-ray diffraction, as described by Bragg's Law, due to the ordered planes of a sample.

The extra distance is depicted as the distance AB + BC in Fig. 2.3, but can also be denoted generally as 2 x d sin(θ). Thus, the constructive interference of X-ray scattering is governed by Bragg's Law,

$$n\lambda = 2d\ \sin\theta, \tag{2.1}$$

where n is an integer, λ is the X-ray wavelength, d is the spacing between particular planes, and θ is the incident angle of the X-ray with respect to the plane of the sample.

Crystalline samples, which have an ordered arrangement of atoms, contain numerous planes which will satisfy Bragg's Law, giving rise to diffraction peaks that occur at different scattering angles (2θ). XRD patterns show the intensity of diffraction peaks as a function of the scattering angles and can be used to determine the atom arrangement of the sample. The arrangements can only occur in a limited number of ways, and space groups are used to designate the symmetry of the sample. Once the space group of the sample is known, diffraction peaks can be assigned a known (*h,k,l*) plane, known as Miller indices, and unit cell parameters can be determined. Since XRD patterns are affected by a multitude of factors, the fitting of patterns to extract information is generally accomplished through "Rietveld refinement".[114]

The method used to collect XRD patterns in this work will be discussed in Section 2.3.1, and the analysis of these patterns by Rietveld refinement will be discussed in Section 2.3.2.

2.3.1 XRD Data Collection

XRD patterns of precursor and lithiated materials were collected with a Siemens D5000 diffractometer in this work. The D5000 utilizes a Bragg-Brentano θ-θ focusing geometry, which situates the X-ray source and detector at a fixed radius from the fixed sample.[115,116] The D5000 can detect diffracted X-rays between scattering angles (2θ) of 0°-130°. Figure 2.4 shows the schematic, as well as a picture, of the D5000 goniometer. The D5000 diffractometer produces X-rays using a copper source. A current of 30 mA is produced by thermionic heating of the tungsten cathode, which is then accelerated at the copper at 40 kV. Electrons in the inner shell (1s) of copper are ejected, and X-rays are emitted when allowed electron transitions from 2p (Cu-Kα, 1.5418 Å) or 3p (Cu-Kβ, 1.3922 Å) fill the 1s electron hole.[117] Exiting through the Be window of the source, the X-ray width is defined by the divergent slit before interacting with the sample. Some of the diffracted beams then reach the scintillation detector after passing through the anti-scatter slit, receiving slit and monochromator which removes Cu-Kβ and fluorescence X-rays.[112]

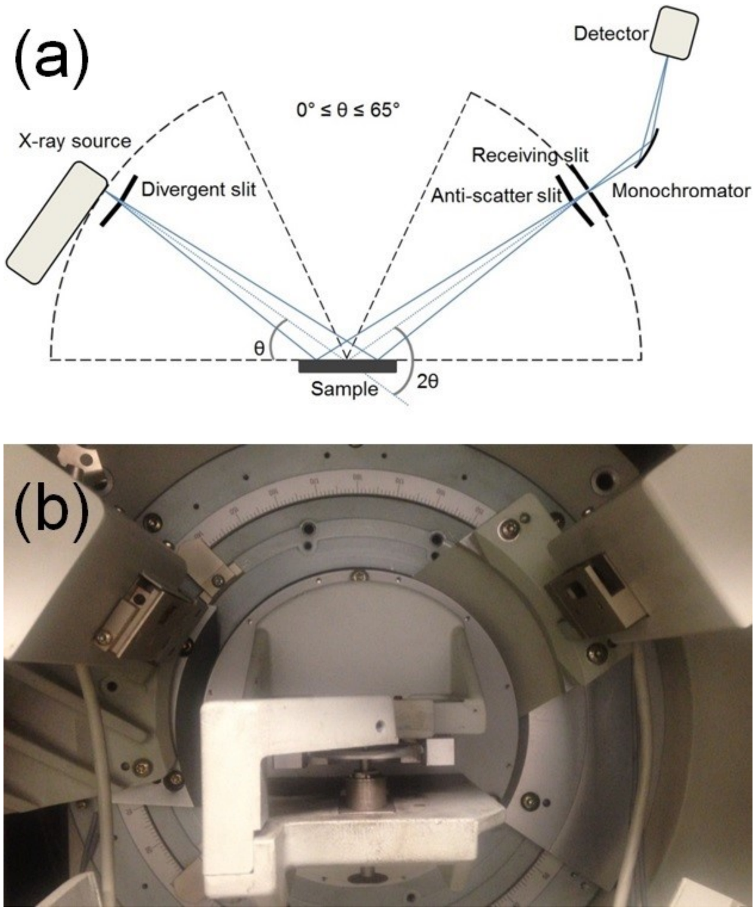

Figure 2.4: A schematic (a) and a picture (b) of the D5000 Bragg-Brentano goniometer.

The scattering vector, which bisects the angle between the incident and diffracted beam, is always normal to the sample surface in the Bragg-Brentano geometry. This means that an orientation will only contain one family of planes that are properly aligned to produce diffraction peaks. Therefore, samples should be prepared to ensure that all orientations are exposed to the X-ray beam over the range of scattering angles.

Both precursor and lithiated samples were lightly ground before XRD measurements. Powders were then packed into the well of a stainless steel sample holder and levelled so the sample was flush with the holder. The sample holder was then mounted onto the diffractometer. Samples were measured in the scattering angle (2θ) range of 10-85° for 3 s at intervals of 0.05° per step. A 1° divergent slit, a 1° anti-scatter slit, and a 0.2 mm receiving slit were used. A slightly different XRD pattern collection protocol was used for in situ XRD experiments, which will be discussed later in Section 2.7.

2.3.2 Rietveld Refinement of XRD Patterns

Samples with consistent structure will generate characteristic XRD patterns. Analysis of these patterns can extract a wide range of information, but many factors affect the patterns. The Rietveld refinement method, a least-squares refinement procedure, was used in this work to calculate XRD patterns through the software Rietica 2.1 for Windows (Rietica).[114,118–120]

In order to calculate and fit XRD patterns, parameters such as the space group and approximate lattice parameters, atomic positions, and site occupations are required to begin refinement. Phases can be identified using software like Match!,[121] which was used in this work, that compares experimental patterns with those in diffraction pattern databases such as PDF-4+.[122] Approximate structural information can be found for identified phase(s).[123] The intensity of a diffraction peak is given by

$$I(2\theta) = I_0\, P(2\theta)\, L(2\theta)\, F^2(h,k,l)\, M(h,k,l)\, DW(h,k,l), \tag{2.2}$$

where I_0 is the intensity of the incident beam, P is the polarization factor, L is the Lorentz factor, F is the geometric structure factor, M is the multiplicity of the (h, k, l) planes, and DW is the Debye-Waller factor.[112]

The polarization factor accounts for the difference in X-ray scattering depending on electric field polarization. The polarization factor is defined as

$$P(2\theta) = \frac{1}{2}(1 + cos^2 2\theta\; cos^2 2\theta_m), \tag{2.3}$$

where θ_m is the angle between the monochromator and the diffracted beam. The Lorentz factor accounts for the random orientation of planes in the sample. Only a fraction of scattered X-rays will be detected, and the Lorentz factor takes the form of

$$L(2\theta) = (4\, sin^2\theta\; cos\theta)^{-1}. \tag{2.4}$$

The geometric structure factor is the sum of the scattering power of all the atoms in the particular (h, k, l) plane, and is given by

$$F(h,k,l) = \sum_1^N f_n\, e^{2\pi i\,(hx_n + ky_n + lz_n)}, \tag{2.5}$$

where f_n is the scattering factor for the atom n with the fractional atomic position (x_n, y_n, z_n). Atomic scattering factors can be found in literature or databases.[113,117] Atomic scattering factors vary depending on the atomic number, Z, since materials with more electrons will experience more interaction with the X-rays.

The multiplicity factor accounts for the number of (h, k, l) planes that will produce a diffracted peak in the same scattering angle.

The Debye-Waller factor accounts for the thermal vibrations of the atoms and is defined as

$$DW(h,k,l) = e^{-B\,(\frac{sin^2\theta}{\lambda})^2}, \tag{2.6}$$

where $B = 8\pi^2u^2$, with u being the root mean square of the thermal displacement of an atom from its equilibrium position.[124] Thermal vibrations increase the effective size of atoms, which increases the probability of destructive interference.

When fitting XRD data, Rietica utilizes Eq. 2.2 as the basis of its calculations, along with a few other parameters such as peak shape, background, preferred orientation, and phase intensities (the functions treating those parameters are given in Chapter 2 of a Rietveld manual).[120] To begin XRD pattern fitting for precursor materials, parameters for $Co(OH)_2$ were used as a starting template. $Co(OH)_2$ can be indexed based on a hexagonal CdI_2-like structure with the $P\bar{3}m1$ space group.[68,125] In the $P\bar{3}m1$ space group, Co was assumed to occupy the 1a sites. OH was assumed to occupy the 2d sites. Lithiated samples used $LiCoO_2$ parameters, indexed based on a hexagonal α-NaFeO2 structure with the $R\bar{3}m$ space group,[18,22] as a starting template. In the $R\bar{3}m$ space group, Li was assumed to occupy the 3a sites (Li layer) while the 3b sites (M layer) contained Co. Oxygen was assumed to occupy the 6c sites. Li (if applicable) and O/OH occupancies were assumed to be 1 and 2, respectively, while the Co occupancy was replaced by the M ratios (M = Co, Mg, Mn) as determined by ICP-OES (Section 2.2).

Initial refinements of phase scale, then lattice parameters, were performed before the background parameters were refined. After background refinement, peak shape parameters were refined carefully by varying parameters individually before collective refinement of the parameters. The oxygen site positions and the sample displacement were the next parameters to be refined. The asymmetry of the peak, the preferred orientation, and overall thermal parameters were then refined if necessary, with parameters reviewed to ensure validity (negative thermal parameters are unphysical, for example).

For lithiated samples, the next sets of refinements were to check for cation mixing. The first check allowed for Li migration into the M layer, with the constraint that the other metal occupancies were reduced by their corresponding ratios to maintain stoichiometry. The exchange of Mg and Li atoms between the 2 layers was refined next, with the constraint of maintaining full occupancy in the Li and M layers.

The lattice parameters were the main information extracted from Rietveld refinements. The lattice parameters were then used to determine the unit cell volume of each sample. Errors reported for the lattice parameters were generated through Rietica, and the unit cell volume errors were calculated by propagating the lattice parameter errors. The Bragg R-factor (R_B) was used in this work to indicate how well the calculated pattern matched the experimental pattern, and is given by

$$R_B = \frac{\sum |I_{ko} - I_{kc}|}{\sum I_{ko}}, \tag{2.7}$$

where I_{ko} and I_{kc} are the observed and calculated integrated intensity of reflection k, respectively. Since the Bragg R-factor only takes the differences between calculated integrated intensities and observed intensities into account,[109,126] the aim of minimizing R_B only served as a guide for pattern fitting, not a rule.

2.4 Scanning Electron Microscopy (SEM)

A common technique used to image the surface topography and particle size of samples is scanning electron microscopy (SEM). SEM offers better resolution than optical microscopes and without the extensive sample preparation required for transmission electron microscopy, making it suitable to characterize the samples synthesized in this work.

SEM imaging of precursor and lithiated materials in this work was carried out using a NanoScience Phenom G2 Pro Desktop SEM which can image samples at a maximum magnification of 45000x. In an evacuated chamber, the SEM probes the surface with a focused electron beam,[111,127] which is produced by thermionic heating of a CeB_6 electron source in the Phenom Pro SEM and accelerated at 5 kV. The electron beam, through a system of condenser lenses and scanning coils, is directed onto the sample and raster scanned across the surface. The interaction between the electron beam and the sample produces various signals, including the scattering of electrons (both elastic and inelastic) and the emission of photons, which can be detected by specialized detectors. The Phenom Pro SEM uses a backscattered electron detector to detect elastically scattered electrons which are higher in energy (>50 eV). Compositional differences can be detected since elements with a higher atomic number backscatter electrons more strongly. The detector lies above the sample in a doughnut shape, allowing the electron beam to shine through the center. The detector is separated into four quadrants, so it can image the topography and composition of the sample based on the signals produced from the different intensities and directions of backscattered electrons.

To prepare powder samples for SEM imaging, samples have to be mounted on a sample stub rigidly so loose powder does not damage the instrument. An adhesive carbon tape was attached to the top of the stub, and a few milligrams of powder mounted onto the tape. The stub was then thoroughly air-blown to remove all loose powder before being placed into the SEM sample holder and imaged.

2.5 Fabrication of Coin Cells for Electrochemical Characterization

In order to characterize the Mg/Mn doped LCO electrochemically, electrodes were prepared with the synthesized materials as the electrochemically active component, which were then assembled into 2325-type (diameter of 23 mm, height of 2.5 mm) coin cells. This section will discuss the two steps of coin cell fabrication, starting first with electrode preparation (Section 2.5.1) before covering coin cell assembly (Section 2.5.2).

2.5.1 Electrode Preparation

The work of Marks *et al.* helped guide the procedure used in this work for electrode preparation.[128] Positive electrodes were prepared by combining the synthesized Mg/Mn doped LCO ($LiCo_{1-2x}Mg_xMn_xO_2$, $0 \leq x \leq 0.05$), Super-S carbon black (Timcal), and polyvinylidene fluoride (PVDF, Arkema, Kynar 301F) in a ratio of 96:2:2 by weight in a polycarbonate container with a ceramic milling bead. A total powder mass of 1 g was generally prepared, although a total powder mass of 0.75 g was prepared on a few occasions. Around 0.55 g (for 1 g powder) or 0.41 g (0.75 g powder) of N-methyl-2-pyrrolidone (NMP, Sigma-Aldrich, 99.5%) was added into the container to form a slurry, with the exact amount of NMP adjusted based on the viscosity of the slurry. The container was then placed in a dual-motion planetary mixer (KK-250 S Mazerustar, Kurabo) and mixed in 3 cycles of 100 s each. If the consistency of the mixed slurry was unsatisfactory, appropriate amounts of NMP were added and mixed for another cycle of 100 s.

A sheet of Al foil (approximately 16 cm x 6 cm, 16 μm thick) was placed on a glass plate and smoothed over using ethanol. The slurry was then coated onto Al foil using a 152 μm notch bar to produce an even coating approximately 4.5 cm wide.[128] The coated foil was then placed in an oven and dried overnight at 120°C. The dried electrode was then pressed at approximately 1000 atm with a roller press and punched into discs with a diameter of 1.3 cm. Electrode loadings generally ranged from 4-8 mg/cm^2.

2.5.2 Coin Cell Fabrication

Positive electrode discs (as prepared in Section 2.5.1) were generally assembled into coin cells within a day or two. The discs were weighed on a microbalance, along with punched discs of the same size of the Al foil. From these masses, along with the masses recorded of the lithiated material, carbon black, and PVDF, the mass of the active component of each electrode disc can be calculated. The discs were then transferred into an argon filled glovebox (Innovative Technologies). Discs that were not used immediately after preparation (Section 2.5.1) were dried overnight in the evacuated antechamber of the glovebox at 120°C.

Coin cells were fabricated inside the glove box to minimize degradation of the lithium metal negative electrode and the electrolyte. Figure 2.5 shows a diagram and a picture of the coin cell components. The electrolyte used in this work contained 1 M

$LiPF_6$ (BASF, 99.9%) in a mixture of 1:2 (v/v) ethylene carbonate (EC) and diethyl carbonate (DEC) (BASF, 99.99%).

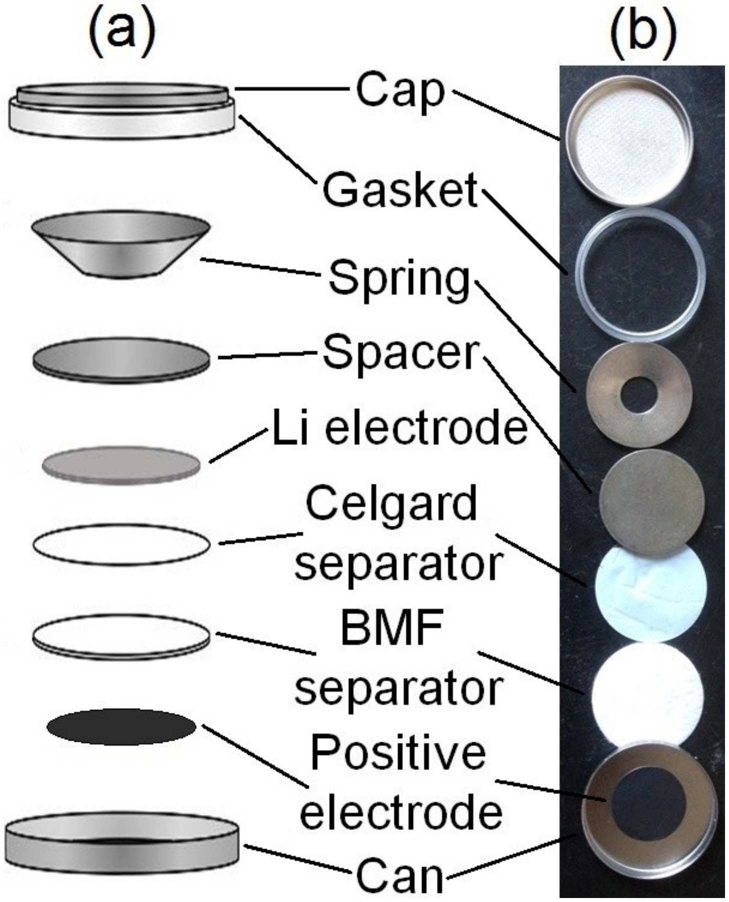

Figure 2.5: A diagram[129] (a) and a picture (b) of the components inside a coin cell. The picture does not show the lithium metal negative electrode, which would be in between the Celgard separator and the spacer.

The positive electrode disc was placed in the stainless steel can before wetting with 2-3 drops (~20 μL per drop) of electrolyte. A polypropylene blown microfiber (BMF) separator (3M) was placed on top of the electrode disc and 8-10 drops of electrolyte was added. Next, a Celgard 2320 thin film polypropylene separator (Celgard) was placed on the BMF separator and another drop of electrolyte was added. A 1.4 cm diameter disc was punched from a 150 μm thick Li metal foil (Chemetall, >99.99%) and placed on the Celgard separator, followed by a stainless steel spacer then a stainless steel spring. Care was taken to keep components centered, and to avoid contact between the Li foil, spacer and spring with the side of the can to avoid shorting the cell. The stainless steel cap and polypropylene gasket were placed on the spring, making sure the gasket kept the top components from contacting the side of the can. The assembled cell was then sealed with a pneumatic press, folding the crimping the can edge onto the gasket. The assembled coin cell was then removed from the glovebox, and stainless steel tabs (approximately 2 cm x 0.5 cm) was spot welded onto the top and bottom of the cell.

2.6 Electrochemical Characterization

Electrochemical characterization is a useful technique in evaluating the performance of a material in an electrochemical cell. Coin cells (Section 2.5) were connected to plastic “boats” before connection to a battery charger, which ensures a consistent and stable connection during measurements. Electrochemical testing was performed using an E-One Moli Energy Limited Canada (Moli) battery testing system in temperature controlled boxes maintained at 30 ± 0.1°C.

Cells were charged and discharged using a constant current, also known as galvanostatic cycling. The lower and upper voltage cutoffs, as well as the magnitude of the current, can be programmed in the testing protocol. The current rates were chosen by determining the theoretical capacity of the positive electrodes, calculated by multiplying the mass of the active component of each positive electrode disc (Section 2.5.2) with the theoretical capacity of the material (Eq. 1.5). Current rates in this work will be stated as a specific capacity (mAh/g) and/or as a C-rate (C/n, where n is equal to the time, in hours, needed to fully charge or discharge based on the expected capacity of the first charge). Due to the nature of coin cell fabrication, sets of 2-4 coin cells were cycled for each condition to help ensure reliability of the data collected.

In Chapters 3 and 5, cells were cycled between 3.6 V and 4.7 V (all voltages reported vs Li/Li^+). The expected capacities of the materials were 250 mAh/g. A current of C/50 (~5 mA/g) was used for the first 2 cycles to carefully examine the features of the initial cycles. A current of C/5 (~50 mA/g) was used for subsequent cycles to evaluate long term cycling performance of the materials. A total of 52 cycles (2 at C/50 and the rest at C/5) were programmed for each cell, though not all cells lasted the full protocol. Section 4.1 explores the cycling of cells at varying upper cutoff voltages. Cells were cycled between 3.6 V and 4.3-4.7 V. Like the rest of this work, cells were programmed for 2 cycles at C/50 and 50 cycles at C/5 after. Since the capacity of materials varies with voltage (given in Table 4.1), the specific currents used were different and were not reported. The cycling protocol for the in situ XRD experiment (Section 4.2) will be discussed in Section 2.7.

The Moli battery charger regularly records the voltage (V), current and time at set time or voltage intervals. Capacity (q) is calculated by multiplying the current by the time taken to charge/discharge. The charger also tracks the voltage change when switching the current direction, and in this work the voltage change upon reaching the top of charge (TOC) will be reported as ΔV_{TOC} (values at the bottom of charge (BOC) are similar). From these measurements and active component masses, cycling data such as charge capacity (C. Cap.), discharge capacity (D. Cap.), and irreversible capacity (Irrev. Cap., reported as mAh/g or % (of C. Cap.)) can be determined and plots such as voltage curves (V vs. q), differential capacity plots (dq/dV vs. V), and cycling performance plots (D. Cap., relative discharge capacity (Rel. D. Cap., based on cycle 1 D. Cap.), and/or ΔV_{TOC} vs. cycle number) generated.

2.7 In Situ XRD

XRD (Section 2.3) is a great technique to characterize the structure of the material as synthesized. However, the technique, as described, is limited to characterizing pristine materials. As discussed in Chapter 1, the electrode materials undergo various changes as lithium is deintercalated/intercalated during cycling. In order to track the structure and lattice parameters shifts as well as phases present during electrochemical cycling, in situ XRD was carried out. This technique involves continuous scanning of a specially designed coin cell connected to a battery charger, allowing for concurrent cell cycling and XRD pattern collection. Similar to Section 2.3, this section will first discuss in situ XRD data collection (Section 2.7.1) before data processing through the use of Rietveld refinements (Section 2.7.2).

2.7.1 In Situ XRD Data Collection

In situ XRD was carried out using the Siemens D5000 diffractometer (Section 2.3.1) to collect patterns of the positive electrode in a purpose-made coin cell undergoing electrochemical cycling.[54,71,87,130] The coin cell had a hole cut into the stainless steel can, but otherwise contained the same hardware as the typical coin cell used for electrochemical testing. The can was precut with a 1.5cm diameter hole, which allowed a

2.0 cm diameter beryllium disc to be adhered onto the can. Be has a low atomic number and is significantly more transparent to X-rays than the stainless steel can. This allows the Be disc to effectively act as a window to collect XRD patterns of the positive electrode coated onto the Be disc.

Positive electrodes were prepared by combining the same 96:2:2 ratios as Section 2.5.1. A total powder mass of only about 0.2 g was prepared and proportionally less NMP was used, so as to produce a more viscous slurry. A 1.5 cm diameter hole was punched in a small strip of Al foil, and the foil was placed on a weighed Be disc with the hole centered above the Be disc. The slurry was coated directly onto the covered Be disc using a 660 μm notch bar. The electrode was dried in an oven overnight at 120°C. The dried electrode was pressed at 1000 atm and weighed. Roscobond, a pressure sensitive adhesive, was applied to the edges of the electrode side of the can and the Be disc was adhered to the can by firm pressing. The cell was then assembled in the same fashion as Section 2.5.2. Minimal amounts of epoxy resin (Torr Seal) was applied to the Be disc-can seam to seal any openings.

The cell was installed into an XRD sample holder connected to the Moli battery testing system and placed in the diffractometer. Figure 2.6 shows a picture of an in situ XRD coin cell in a sample holder and a picture of the sample holder set up in the diffractometer.

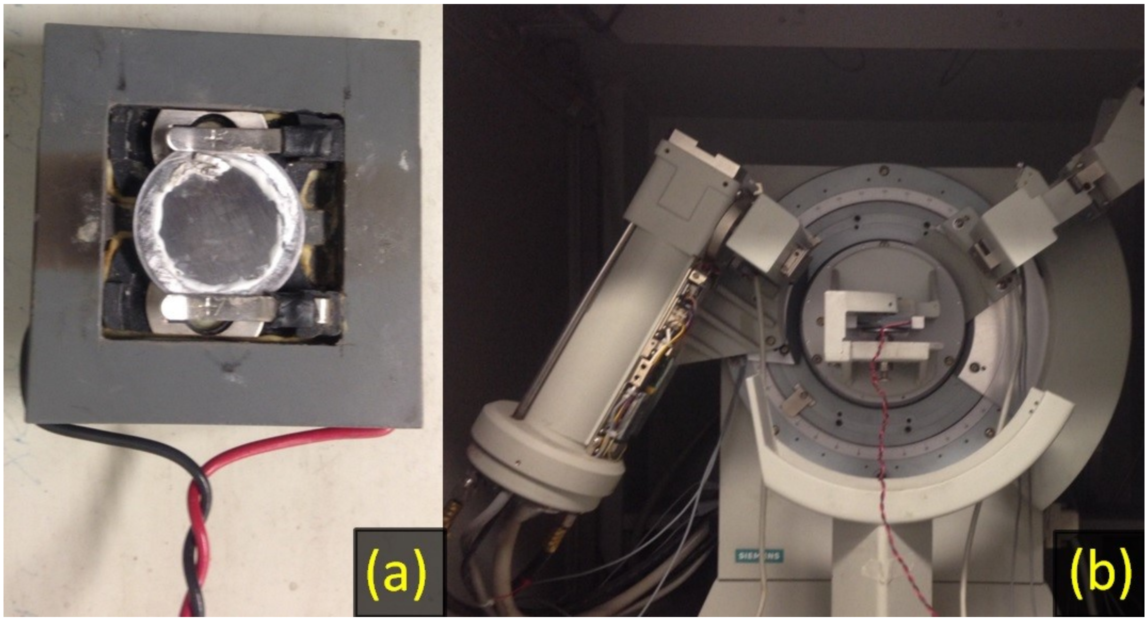

Figure 2.6: Picture of a typical in situ XRD setup: (a) the purpose-made coin cell installed in the in situ XRD sample holder and (b) the sample holder installed in the diffractometer.

XRD pattern collection and cycling protocols were slightly different for the three in situ XRD experiments. Scattering angle ranges were chosen initially based on reflections observed in the lithiated samples, but were later condensed. Dwell times and step sizes were adjusted for each experiment to ensure a balance between resolution and scan frequency. A target of 20-30 scans for the 1st charge, as well as a peak of at least 1500 counts for the (104) reflection, guided pattern collection protocol. All cells were cycled between 3.6 V and 4.7 V for 1.5 cycles (charge-discharge-charge) at room temperature.

A current of C/100 (~2.5 mA/g) was used for the 0% Mg/Mn sample. XRD patterns were collected in the scattering angle (2θ) ranges of 17.5-22°, 36-40.5°, 41.5-46.5°, 48-54°, 58-61°, 63-67.5°, and 69-70.5° at intervals of 0.02° for 8 s per step. To reduce the time of the experiment, both 2% and 5% Mg/Mn used a higher current of C/50 (~5 mA/g). XRD patterns were collected in the scattering angle (2θ) ranges of 18.5-20.7°, 36.5-39°, 43.5-46°, 58-60.5°, and 64-67.5° at intervals of 0.025° for either 12 s per step (2% Mg/Mn) or 15 s per step (5% Mg/Mn). X-ray beam widths at lower scattering angles were slightly wider than electrode size, which affected the intensity of the (003) peak compared to the rest of scattering angle regions.

2.7.2 Rietveld Refinement of In Situ XRD Patterns

Past in situ XRD work on NMC material was able to utilize the GSAS package,[131] which has an automated sequential fitting function to expedite Rietveld refinement on large amounts of XRD patterns collected.[54,132] The use of GSAS to analyze this work's in situ XRD experiments was explored, but was unfortunately found not suitable due to the sporadic presences of different phases. Instead, like Section 2.3.2, Rietica was used to perform Rietveld refinements.[114,118–120] Only every 2nd or 3rd scan was analyzed except at high voltage (> 4.5 V), where every scan was refined.

Since each in situ XRD scan only collected a limited number of scattering angle ranges, Rietveld refinements on any one pattern were futile due to the instability of refinements. Instead, refinements of the whole experiment were performed sequentially, with the first two sets of refinements being performed on an XRD pattern of the powder (Section 2.3) and a detailed scan (15-70° at intervals of 0.05° for 12 s per step) of the in situ cell before charging. With most of the parameters established from the previous pattern, refinements only required parameters to vary slightly in order to fit the current pattern, thus reducing instability while refining.

The Rietveld refinement protocols used for in situ XRD experiments were based on Section 2.3.2, with several adjustments. The O3 phases were refined as described (Section 2.3.2), with several other phases being refined as they appeared. An unused electrode phase, which was the O3 phase refined for the 1st scan, was included once two (003) reflection peaks could be seen. Only the phase scale and preferred orientation were varied for the unused electrode phase. Similar to the O3 phase, the O6 phase was refined with the $R\bar{3}m$ space group, but the *c* lattice parameter was doubled to account for 6 CoO_2 slabs instead of 3.[72,73] For the O6 phase, Li was assumed to occupy the 3a sites, with Co and two oxygens occupying the 6c site (starting $z = 0.42$, 0.27 and 0.11 respectively). The O1 phase was reduced to only 1 CoO_2 slab, which simplified the structure to be analogous to the precursor material.[68] No refinements were performed for the O1 phase because the observed peaks were not distinct enough to be refined stably. The monoclinic phase was refined in the C2 space group, with Li occupying 2a and 4c sites, Co occupying 2b and 4c sites, and three oxygens occupying 4c sites.[71] Due to the beam width issue, the preferred orientation of the (003) reflection was also refined ((006) reflection for the O6 phase).

For all phases, Li occupations were not refined as Li is not a strong scatterer (Z=3). Li occupancies were assumed to be 1 for O3, 0.5 for monoclinic, and 1/6 for O6 phases. For the 5% Mg/Mn experiment, Mg was checked for occupancy in the lithium layer with constraints to either stoichiometry or fixed Mg values. Oxygen occupancy,[86] which may give confirmation of oxygen loss, was not refined due to insufficient data.

Similar to Rietveld refinements of precursor and lithiated samples, the primary information extracted from each refinement were lattice parameters and their associated errors, as well as the Bragg R-factor. Phase scales for each phase, as well as Mg occupancy for 5% Mg/Mn, were also obtained. Scans were then coupled to Moli charger data by matching recorded Moli voltages and times to XRD ranges and scattering angles. Once Moli and D5000 data were coupled, capacity was used to determine state of charge as well as degree of delithiation.

The equation used to determine weight fractions of phases takes the form of

$$W_P = \frac{(SNMV)_p}{\sum_i (SNMV)_i}, \tag{2.8}$$

where S is the scale factor, N is the number of formula units per unit cell, M is the molecular weight of the formula unit, V is the unit cell volume, the subscript p is the phase in question, and i is an index running over all phases.[120] Hunter and Howard noted that S*V is proportional to the number of unit cells diffracting,[120] so this simplification was used in this work since the interest is in the proportion of the phases, not the weights. It is also noted that the preferred orientation parameter affected the phase scale value, but was not accounted for while determining phase fractions, and so analyses were qualitative, not quantitative. However, phase scale values were generally consistent with neighbouring scans and did not significantly affect phase weight fractions.

For lattice parameter and volume comparisons, the unit cells of the different phases were converted to the O3 unit cell. The O6 unit cell was converted by halving its *c* lattice parameter but retaining its original *a* lattice parameter. The monoclinic cell was converted by retaining its original *c* lattice parameter, and averaging the *a* lattice parameter divided by the square root of 3 with the *b* lattice parameter.[71]

Chapter 3 – Initial Investigation of Mg/Mn Doped LCO

This chapter will discuss the initial set of experiments carried out to study the Mg/Mn doped LCO that was synthesized and lithiated as discussed in Section 2.1. First the characterizations of precursor materials (Section 3.1) and lithiated materials (Section 3.2) will be covered before examining the electrochemical performance of the lithiated materials (Section 3.3).

3.1 Characterization of Precursor Materials

A series of $Co_{1-2x}Mg_xMn_x(OH)_2$ ($0 \leq x \leq 0.05$) precursor materials were synthesized by co-precipitation as discussed in Section 2.1.1. Table 3.1 lists the precursors synthesized by their target Mg/Mn content and their expected compositions based on masses used in the synthesis. Also included in Table 3.1 are the designations each precursor will be referred to in this thesis. The precursor materials were characterized by ICP-OES, XRD, and SEM, and these data will be discussed in Sections 3.1.1-3, respectively.

Table 3.1: List of $Co_{1-2x}Mg_xMn_x(OH)_2$ ($0 \leq x \leq 0.05$) precursor materials synthesized.

Target Content	Sample Designation	Expected Compositions
0% Mg/Mn	MM0p	$Co(OH)_2$
1% Mg/Mn	MM1p	$Co_{0.980}Mg_{0.010}Mn_{0.010}(OH)_2$
2% Mg/Mn	MM2p	$Co_{0.960}Mg_{0.020}Mn_{0.020}(OH)_2$
3% Mg/Mn	MM3p	$Co_{0.940}Mg_{0.030}Mn_{0.030}(OH)_2$
4% Mg/Mn	MM4p	$Co_{0.920}Mg_{0.040}Mn_{0.040}(OH)_2$
5% Mg/Mn	MM5p	$Co_{0.900}Mg_{0.050}Mn_{0.050}(OH)_2$

3.1.1 Elemental Analysis of Precursor Materials by ICP-OES

ICP-OES was used to determine the cation ratios of the precursor samples. As described in Section 2.2, the metal concentrations measured were converted to a ratio, which was then normalized to 1 for precursor ratios. Sample compositions were then assumed to have the formula unit $M_1(OH)_2$ (M = Co, Mg, Mn). Table 3.2 shows each precursor materials' expected composition and their determined ratio.

Table 3.2: Precursor material cation ratios as determined by ICP-OES assuming the formula unit $M_1(OH)_2$ (M = Co, Mg, Mn) and normalizing cation ratios to 1.

Sample	Determined Ratio (Co : Mg : Mn)	Expected Composition
MM0p	1.000 : 0.000 : 0.000	$Co(OH)_2$
MM1p	0.981 : 0.009 : 0.009	$Co_{0.980}Mg_{0.010}Mn_{0.010}(OH)_2$
MM2p	0.961 : 0.020 : 0.020	$Co_{0.960}Mg_{0.020}Mn_{0.020}(OH)_2$
MM3p	0.942 : 0.029 : 0.029	$Co_{0.940}Mg_{0.030}Mn_{0.030}(OH)_2$
MM4p	0.916 : 0.043 : 0.042	$Co_{0.920}Mg_{0.040}Mn_{0.040}(OH)_2$
MM5p	0.900 : 0.050 : 0.049	$Co_{0.900}Mg_{0.050}Mn_{0.050}(OH)_2$

Figure 3.1 shows graphs of the elemental analysis results listed in Table 3.2. As mentioned earlier, expected compositions were calculated based on the masses of the reagents used for the co-precipitation reactions. Figure 3.1 shows that measured ratios were close to expected ratios.

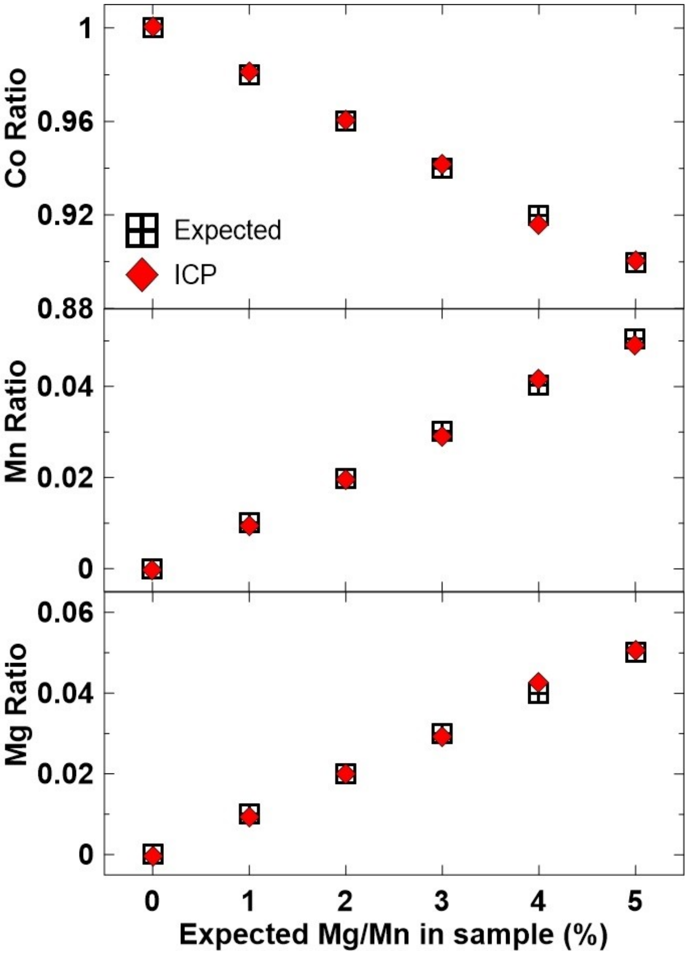

Figure 3.1: Metal atomic ratios as determined by ICP-OES for precursor samples. Ratios were normalized to 1 for precursors.

3.1.2 Structure Analysis of Precursor Materials by XRD

Figure 3.2 shows the XRD patterns of the precursor samples collected, as described in Section 2.3.1, along with an expanded view of the (110) reflection. Reflections, as indexed in the P$\overline{3}$m1 space group, are labeled in the figure as well. All precursors were single phase materials, with little effect from Mg/Mn substitution other than a broadening of peaks as seen in the expanded view and a slightly lower angle at which reflections appear, indicative of increasingly larger unit cells. Peak broadening may be occurring due to this synthesis forming small particles, which will be discussed in Section 3.1.3.

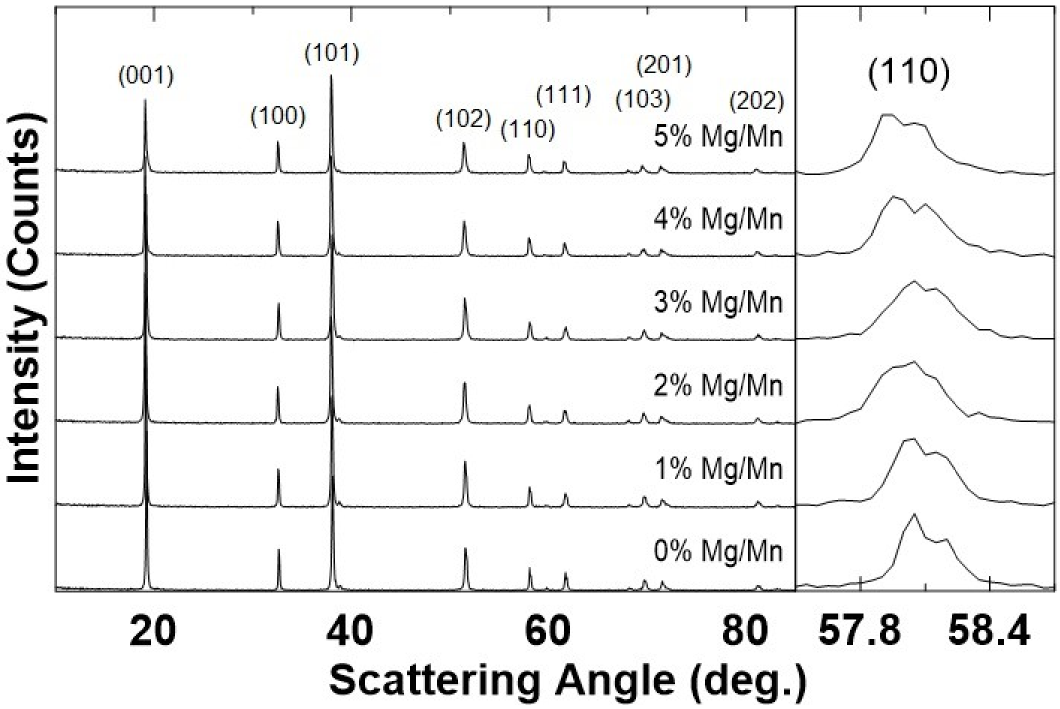

Figure 3.2: XRD patterns (Cu Kα radiation) of precursor samples collected from 10°–85°, along with reflections indexed in the $P\overline{3}m1$ space group and an expanded view of the (110) reflection.

Rietveld refinement was performed on the XRD patterns in Fig. 3.2 as detailed in Section 2.3.2. In the $P\overline{3}m1$ space group, Co, Mg, and Mn were assumed to occupy the 1a sites while O and H were assumed to occupy the 2d sites. Metal occupancies were set to match the ratios as determined by ICP-OES (Section 3.1.1). Figure 3.3 shows the XRD patterns as well as the pattern fitting for all 6 precursor XRD patterns seen in Fig. 3.2.

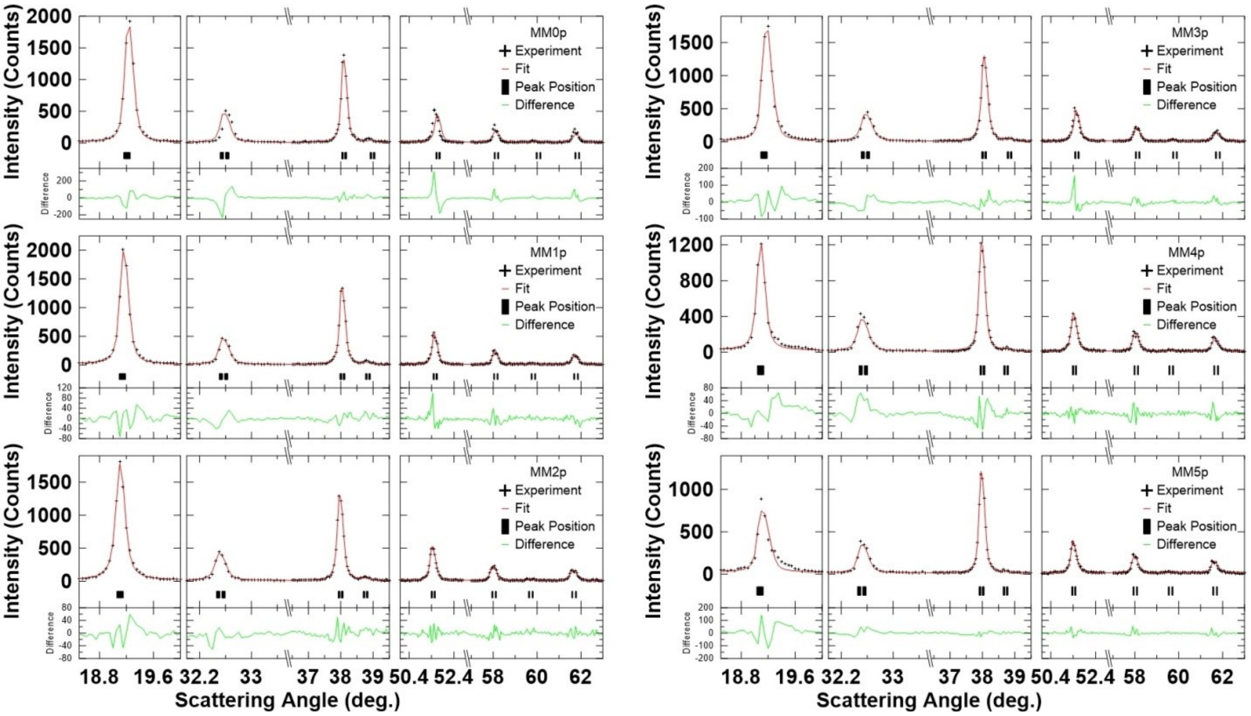

Figure 3.3: XRD Rietveld refinement pattern fitting for precursor materials. Only select reflections are shown in this figure. Sample displacement refinements were not included with these refinements.

The Rietveld refinements performed for these materials did not include refinements of sample displacement. Including refinements of sample displacement yielded better fits with a lower Bragg R-factor, but gave inconsistent sample displacements and the unit cell sizes did not correspond well with the trend seen in Fig. 3.2. Rietveld refinement results that included refinements of sample displacement can be found in Appendix A. It is unknown why including sample displacement refinements for this set of samples resulted in erroneous values whereas all other Rietveld refinements performed with sample displacement refinements in this thesis had no such issues. Table 3.3 shows the results from the refinements. Included in the table are the *a*-axis and *c*-axis lattice constants, the unit cell volume, their corresponding errors, and the Bragg R-factors.

Table 3.3: Rietveld refinement results for precursor XRD patterns. Refinements of sample displacement were not done with these refinements.

Sample	***a* (Å) (± 0.0002 Å)**	***c* (Å) (± 0.0003 Å)**	**Vol. (Å^3) (± 0.003 Å^3)**	**R_{Bragg}**
MM0p	3.1742	4.6229	40.338	7.10
MM1p	3.1758	4.6393	40.522	3.24
MM2p	3.1796	4.6472	40.688	2.01
MM3p	3.1754	4.6390	40.509	3.81
MM4p	3.1785	4.6516	40.698	3.01
MM5p	3.1807	4.6534	40.771	4.05

Figure 3.4 shows graphs of the results in Table 3.3. The values obtained from Rietveld refinements correspond well to the trends seen in Fig. 3.2, including a slight decrease in unit cell size for MM3p. As more Mg/Mn was incorporated into the samples, the unit cell enlarged from a = 3.1742 Å, c = 4.6229 Å, and cell volume = 40.338 Å^3 for MM0p to a = 3.1807 Å, c = 4.6534 Å, and cell volume = 40.771 Å^3 for MM5p. The trend of unit cell volume growth with increasing Mg/Mn content is reasonable due to the average sizes of the ions involved (radius of Co^{+3}, $r_{Co^{+3}}$ = 0.545 Å; $r_{Mg^{+2}}$ = 0.72 Å; $r_{Mn^{+4}}$= 0.53 Å).[133] It is uncertain why MM3p showed a slightly smaller volume (40.509 Å^3) than MM2p (40.688 Å^3) and MM4p (40.698 Å^3). After the lithiation process (Section 2.1.2) where samples reached a temperature of 900°C, the unit cell volumes increased consistently with increases of Mg/Mn content (Section 3.2.2).

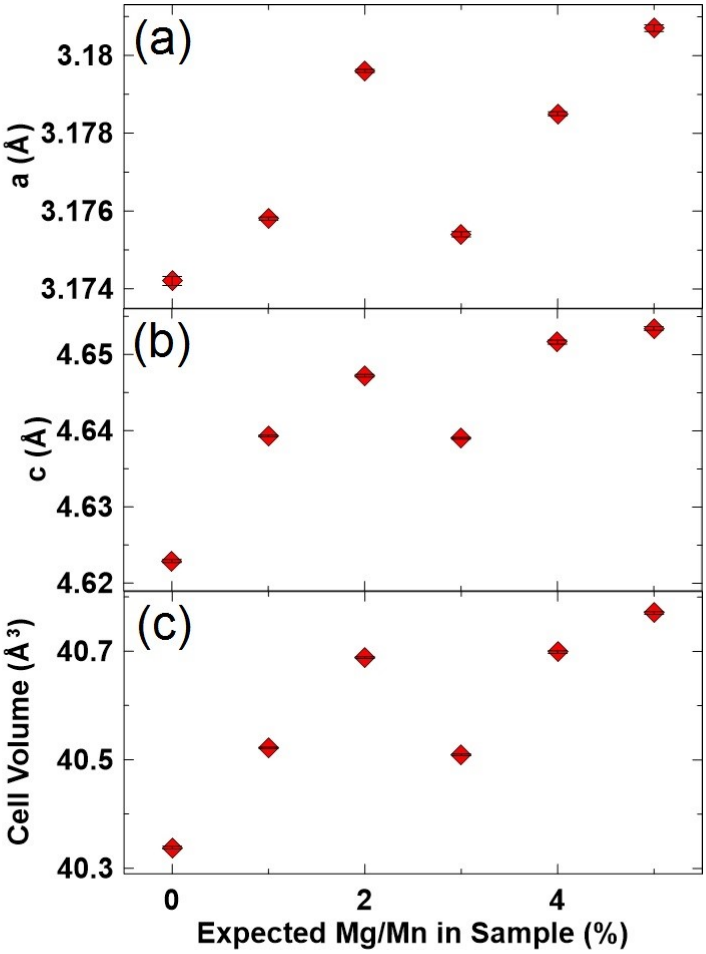

Figure 3.4: Lattice constants (panels a and b), obtained from Rietveld refinements of XRD patterns of precursor samples, and unit cell volume (c) calculated from the lattice constants. Refinements of sample displacement were not included with these refinements.

3.1.3 SEM Images of Precursor Materials

Figure 3.5 shows the SEM images of the precursor materials. While co-precipitation syntheses can be optimized to control precursor particle properties,[105,106,108] this experiment focused on the effects of Mg/Mn substitution. Optimization of particle size and shape was not carried out. As such, the SEM images of most of the precursor materials showed very small particles.

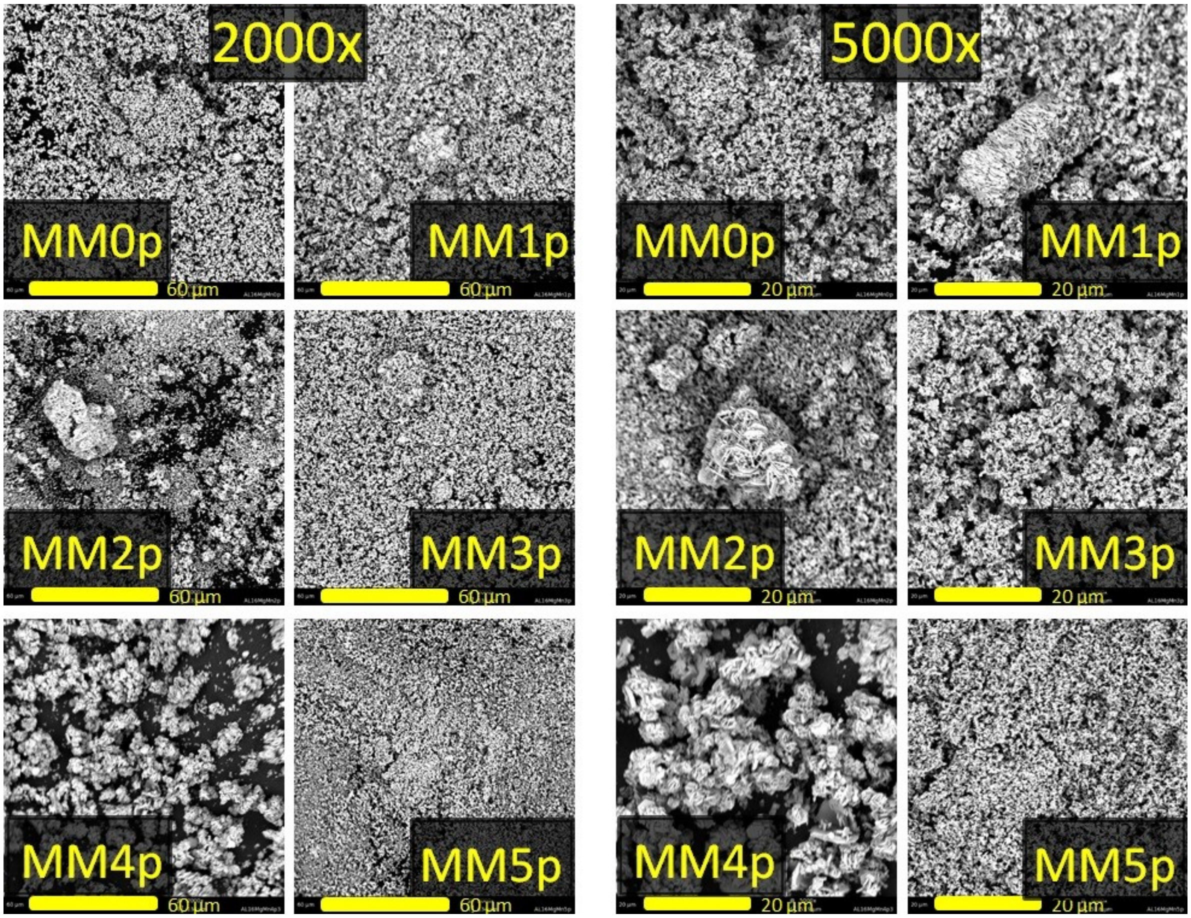

Figure 3.5: SEM images of precursor materials magnified at 2000x (left) and 5000x (right).

Figure 3.5 shows that most SEM images showed small particles. However, MM2p showed a few larger particles while MM4p3 showed almost exclusively larger particles. Synthesis conditions were examined, and attempts to recreate large particles were successful multiple times for 4% Mg/Mn but unsuccessful for 5% Mg/Mn using the co-precipitation method as described in Section 2.1.1. In fact, 3 batches of 4% Mg/Mn precursors were synthesized, with every batch containing mainly large particles. The most recent batch was used for subsequent experiments. It is uncertain why only 4%

Mg/Mn formed large particles consistently, as reaction conditions for all co-precipitation syntheses were very similar. However, co-precipiation synthesis using the tank reactor (Section 2.1.3) also formed similarly large particles for 5% Mg/Mn (to be discussed later in chapter 5), so a study controlling synthesis conditions could be undertaken if particle properties were to be optimized.

3.2 Characterization of Lithiated Materials

After precursor materials were characterized to confirm their structures and compositions, the precursors were lithiated as detailed in Section 2.1.2. Table 3.4 lists the lithiated materials prepared by their target Mg/Mn content and their expected compositions based on masses used in the lithiation process. Sample designations are also included in Table 3.4, and this thesis will refer to each sample by either their designation or by their target content (i.e.: $Li_{1.025}Co_{0.936}Mg_{0.019}Mn_{0.019}O_2$ is referred to as either 2% Mg/Mn or MM2). Like the precursor materials, lithiated materials were characterized by ICP-OES, XRD, and SEM, and these data will be discussed in Sections 3.2.1-3, respectively.

Table 3.4: List of $Li_yCo_{1-2x}Mg_xMn_xO_2$ ($0 \leq x \leq 0.05$) materials synthesized.

Target Content	Sample Designation	Expected Compositions
0% Mg/Mn	MM0	$Li_{1.024}Co_{0.976}O_2$
1% Mg/Mn	MM1	$Li_{1.025}Co_{0.955}Mg_{0.010}Mn_{0.010}O_2$
2% Mg/Mn	MM2	$Li_{1.025}Co_{0.936}Mg_{0.019}Mn_{0.019}O_2$
3% Mg/Mn	MM3	$Li_{1.024}Co_{0.917}Mg_{0.029}Mn_{0.029}O_2$
4% Mg/Mn	MM4	$Li_{1.023}Co_{0.899}Mg_{0.039}Mn_{0.039}O_2$
5% Mg/Mn	MM5	$Li_{1.025}Co_{0.877}Mg_{0.049}Mn_{0.049}O_2$

3.2.1 Elemental Analysis of Lithiated Materials by ICP-OES

ICP-OES was used to determine the cation ratios of the lithiated samples. As described in Section 2.2, the cation concentrations measured were converted to a ratio, which was then normalized to 2 for lithiated material ratios. Sample compositions were then assumed to have the formula unit $Li_yM_xO_2$ (x + y = 2; M = Co, Mg, Mn). Table 3.5 shows the expected composition and the determined ratio of the samples.

Table 3.5: Lithiated material cation ratios as determined by ICP-OES assuming the formula unit $Li_yM_xO_2$ (x + y = 2; M = Co, Mg, Mn) and normalizing cation ratios to 2.

Sample	Determined Ratio (Li : Co : Mg : Mn)	Expected Composition
MM0	1.000 : 0.999 : 0.000 : 0.000	$Li_{1.024}Co_{0.976}O_2$
MM1	0.982 : 0.996 : 0.010 : 0.012	$Li_{1.025}Co_{0.955}Mg_{0.010}Mn_{0.010}O_2$
MM2	0.992 : 0.967 : 0.021 : 0.020	$Li_{1.025}Co_{0.936}Mg_{0.019}Mn_{0.019}O_2$
MM3	0.991 : 0.947 : 0.031 : 0.031	$Li_{1.024}Co_{0.917}Mg_{0.029}Mn_{0.029}O_2$
MM4	0.981 : 0.931 : 0.044 : 0.044	$Li_{1.023}Co_{0.899}Mg_{0.039}Mn_{0.039}O_2$
MM5	0.995 : 0.900 : 0.053 : 0.052	$Li_{1.025}Co_{0.877}Mg_{0.049}Mn_{0.049}O_2$

Figure 3.6 shows graphs of the elemental analysis results listed in Table 3.5. As discussed earlier, expected compositions were calculated based on the masses used for the lithiation process. Unlike Fig. 3.1, the measured ratios were not as close to the expected ratios. Discrepancies between measured and expected ratios for the lithiated samples stem from lithium loss during the heating step, which was expected, but not accounted for, in the calculation of the expected ratio. The decrease in lithium content produced a corresponding increase when calculating the ratio of the other metals.

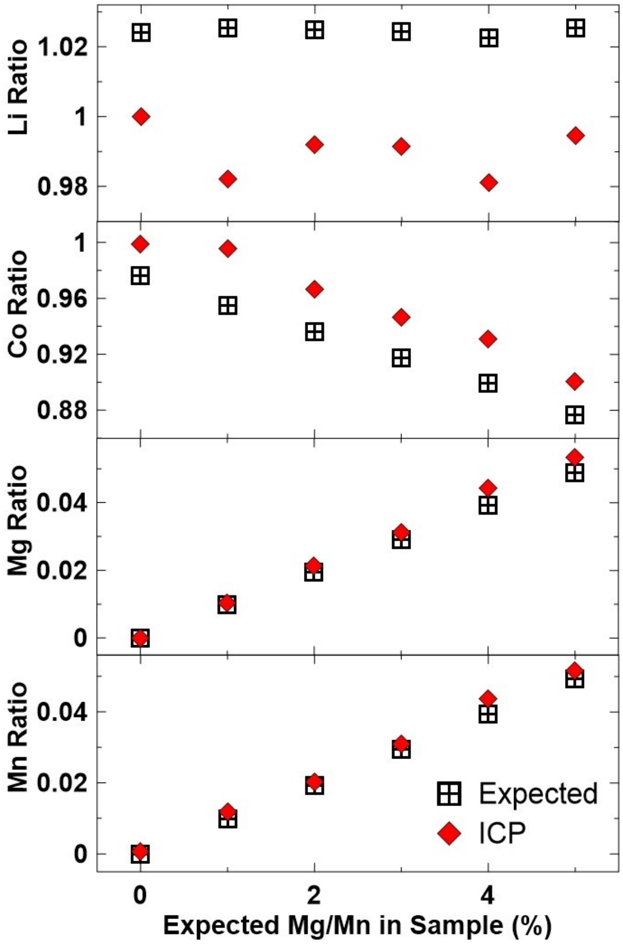

Figure 3.6: Metal atomic ratios as determined by ICP-OES for lithiated materials. Ratios were normalized to 2 for lithiated samples.

3.2.2 Structure Analysis of Lithiated Materials by XRD

Figure 3.7 shows XRD patterns of the lithiated samples collected (described in Section 2.3.1), along with an expanded view of the (108) and (110) reflections. Reflections, as indexed in the $R\bar{3}m$ space group, are labeled in the figure as well. Like the precursor samples seen in Fig. 3.2, lithiated samples were single phase materials, with similar effects from increasing Mg/Mn substitution such as some peak broadening as seen in the expanded view and a slightly lower angle at which reflections appear. As mentioned previously, reflections appearing at a lower angle indicate larger unit cells.

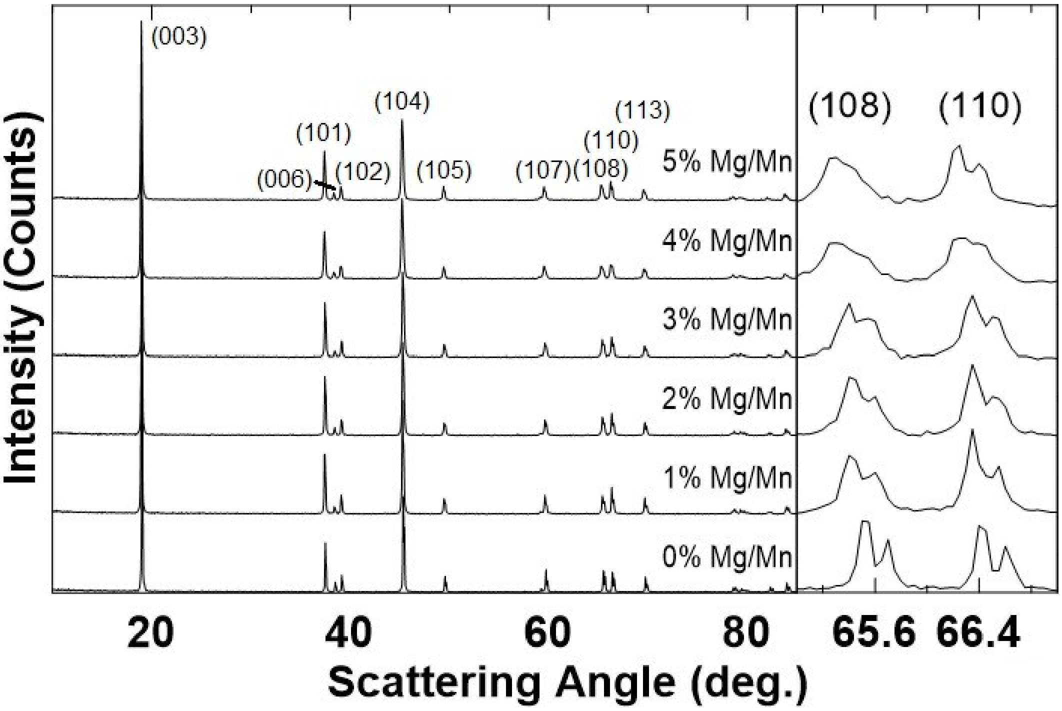

Figure 3.7: XRD patterns (Cu Kα radiation) of lithiated samples collected from 10°–85°, along with reflections indexed in the $R\bar{3}m$ space group and an expanded view of the (108) and (110) reflections.

Rietveld refinements were performed on the XRD patterns in Fig. 3.7 as detailed in Section 2.3.2. In the $R\bar{3}m$ space group, Li was assumed to occupy the 3a sites (lithium layer) while the 3b sites (metal layer) contained Co, Mg, Mn, and any excess Li. Oxygen was assumed to occupy the 6c sites. Metal occupancies were set to match the ratios as determined by ICP-OES (Section 3.2.1). Excess Li was allowed in the metal layer, with the constraint that the other metal occupancies were reduced by their corresponding ratios to maintain stoichiometry. The exchange of Mg and Li atoms between the 2 layers was also allowed with the constraint of maintaining stoichiometry, but no Mg was found in the lithium layers as reported previously.[31,33,85–87] Figure 3.8 shows the measured and calculated XRD patterns for all 6 lithiated sample XRD patterns seen in Fig. 3.7.

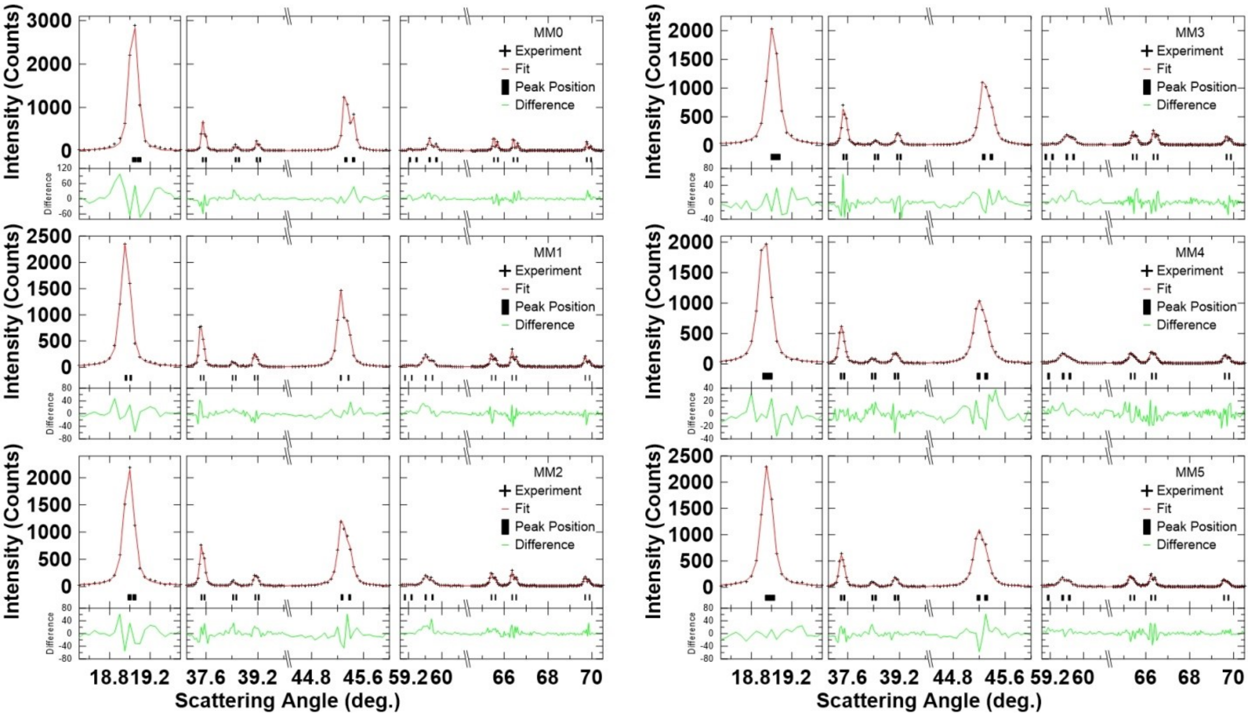

Figure 3.8: XRD Rietveld refinement pattern fitting for lithiated samples. Only select reflections are shown in this figure.

As discussed in Section 2.3.2 and unlike Rietveld refinements of precursor materials (Section 3.1.2), the Rietveld refinements performed for these materials included the refinement of sample displacement. Table 3.6 shows the results from the refinements. Included in the table are the *a*-axis and *c*-axis lattice constants, the unit cell volume, their corresponding errors, and the Bragg R-factors.

Table 3.6: Rietveld refinement results for lithiated material XRD patterns.

Sample	***a* (Å) (± 0.0001 Å)**	***c* (Å) (± 0.0002 Å)**	**Vol. (Å^3) (± 0.002 Å^3)**	**R_{Bragg}**
MM0	2.8161	14.0488	96.486	3.66
MM1	2.8164	14.0615	96.594	2.74
MM2	2.8178	14.0717	96.760	3.17
MM3	2.8194	14.0820	96.941	2.54
MM4	2.8200	14.0890	97.031	2.06
MM5	2.8223	14.0973	97.246	1.84

Figure 3.9 shows graphs of the results in Table 3.6. The values obtained from Rietveld refinements correspond well to the peak trends seen in Fig. 3.7.

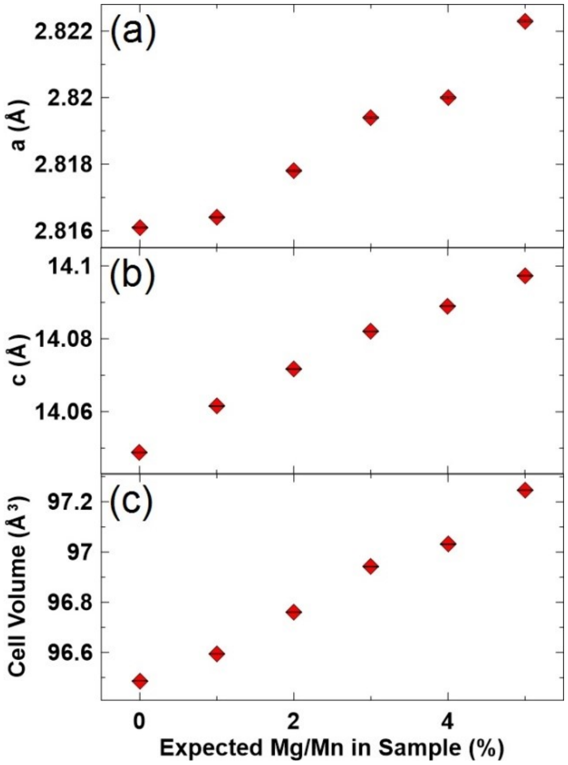

Figure 3.9: Lattice constants (panels a and b), obtained from Rietveld refinements of XRD patterns of lithiated materials, and unit cell volume (c) calculated from the lattice constants.

As more Mg/Mn was incorporated into the samples, the unit cell enlarged from *a* = 2.8161 Å, *c* = 14.0488 Å, and cell volume = 96.486 Å^3 for 0% Mg/Mn to *a* = 2.8223 Å, *c* = 14.0973 Å, and cell volume = 97.246 Å^3 for 5% Mg/Mn. The trend of unit cell volume growth due to increasing Mg/Mn content reaffirms the reasoning given in Section 3.1.2, and this trend is more consistent than seen with the precursors.

3.2.3 SEM Images of Lithiated Materials

Figure 3.10 shows the SEM images of the lithiated materials. As shown in Fig. 3.5, the SEM images of most of the precursor materials showed very small particles. During the lithiation process (Section 2.1.2), most of these particles then aggregated together to form clusters with ~20 μm diameter. Small particles that did not aggregate could still be seen in most of the lithiated samples.

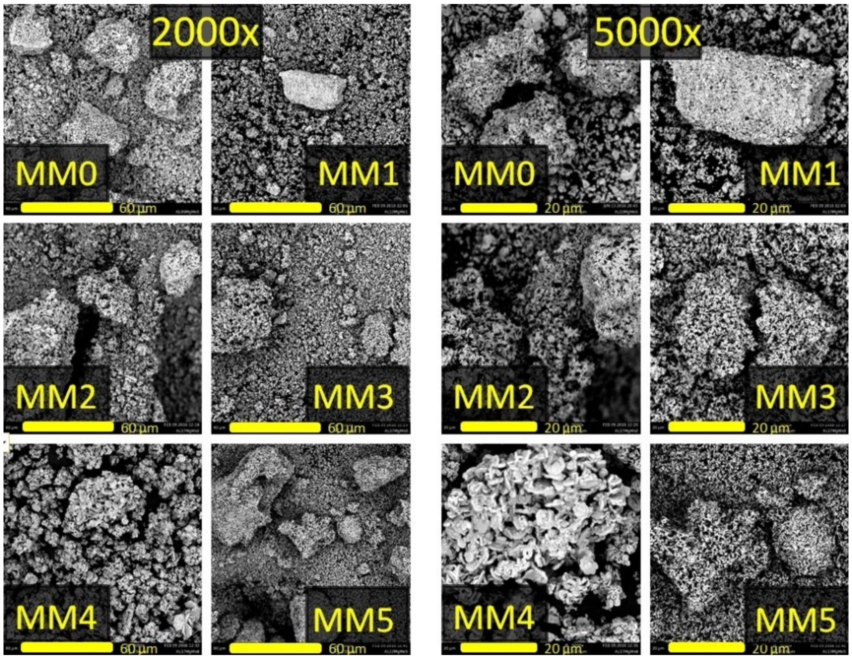

Figure 3.10: SEM images of lithiated samples magnified at 2000x (left) and 5000x (right).

As seen in Fig. 3.10, MM4 also seemed to undergo aggregation of particles and showed unaggregated particles as well. Aggregated cluster sizes in MM4 do not seem too much larger than with other lithiated samples.

3.3 Electrochemical Performance of Mg/Mn Doped LCO

Electrodes were prepared from the lithiated samples as detailed in Section 2.5.1, and coin cells were fabricated as described in Section 2.5.2. As described in Section 2.6, coin cells were cycled between 3.6 V and 4.7 V at 30°C. The first two cycles used a specific current of ~5 mA/g (C/50) while all subsequent cycles used a specific current of ~50 mA/g (C/5). Section 3.3.1 will discuss data from the first cycle of these coin cells, while data from the second cycle will be compared to the first cycle in Section 3.3.2, and long term cycling performance will be examined in Section 3.3.3. Several cells of each Mg/Mn content were fabricated, but only 1 of each will be shown for cell voltage versus capacity and differential capacity versus voltage plots.

3.3.1 First Cycle Data

Figure 3.11 shows first cycle data (cell voltage as a function of capacity (a), 1st charge capacity (b), 1st discharge capacity (c), and 1st cycle irreversible capacity (d)) from coin cells fabricated from the lithiated materials. Fig. 3.11a shows that as the Mg/Mn doping increases, cells returned less capacity during discharge, qualitatively indicating an increase in irreversible capacity. Additionally, the voltage plateaus seen at high voltage during both charge and discharge became more sloped, likely signaling a suppression of the phase transitions that occur in that voltage range. This will be explored further later.

First charge capacity (Fig.3.11b) increased slightly as Mg/Mn substitution increased, going from 249 mAh/g for 0% Mg/Mn to 260 mAh/g for 5% Mg/Mn. First discharge capacity (Fig. 3.11c) decreased from 204 mAh/g for 0% Mg/Mn to 144 mAh/g for 5% Mg/Mn. This lead to an increase in irreversible capacity (Fig. 3.11d) as doping increased (18.1% for 0% Mg/Mn and 44.7% for 5% Mg/Mn).

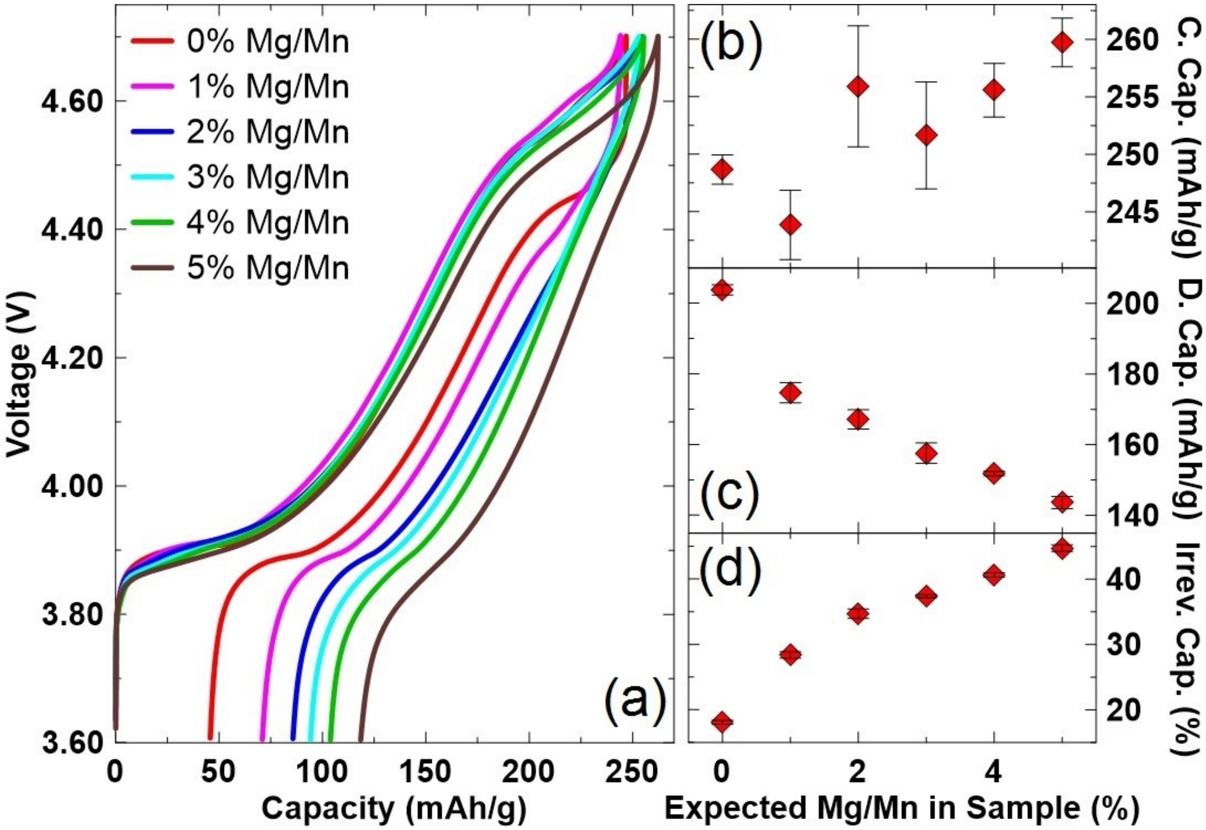

Figure 3.11: First cycle (a) cell voltage as a function of capacity, (b) charge capacity, (c) discharge capacity, and (d) irreversible capacity for MM0-MM5 cells cycled between 3.6 V and 4.7 V. The data was collected at 30°C using a specific current of ~5 mA/g (C/50).

Considering only the material composition, the substitution of electrochemically inactive Mg^{+2} and Mn^{+4} ions for electrochemically active Co^{+3} ions may explain the decrease in discharge capacity (Fig. 3.11c),[87] but it does not explain the slight increase in charge capacity (Fig. 3.11b). However, if we assume delithiation based on lithium content and disregard electrochemically inactive ions, the slight increase in charge capacity may be attributed to the slight decrease of the molecular weight as Mg/Mn is substituted for Co. Realistically, there are other factors, including electrolyte degradation or oxygen evolution, which may have contributed to the increase in irreversible capacity as doping increased. Some of these factors will be discussed later.

Another potential explanation for this increase in irreversible capacity may be that increasing Mg/Mn content prevented complete delithiation and the charge capacity stemmed from electrolyte degradation instead. This could explain the capacity trends seen in Fig. 3.11b and Fig. 3.11c, as well as provide reasoning as to why a suppression of phase transitions may have occurred. While this theory was valid when examining only the first cycle, data from subsequent cycles disproved it, and this will be discussed later.

Figure 3.12 shows dq/dV as a function of voltage, with the right panel showing a closer view of the high voltage region (~4.25-4.7 V). There are multiple features to note as Mg/Mn content increased, and these have been labelled as a, b, and c. Feature a is the sharp peak at 3.9 V shrinking and broadening within a voltage range of 3.87-3.9 V. Feature b indicates a gradual loss of the order-disorder transition. Feature c shows the transition of the 2 peaks between 4.55 V and 4.65 V to one broad peak at ~4.5 V.

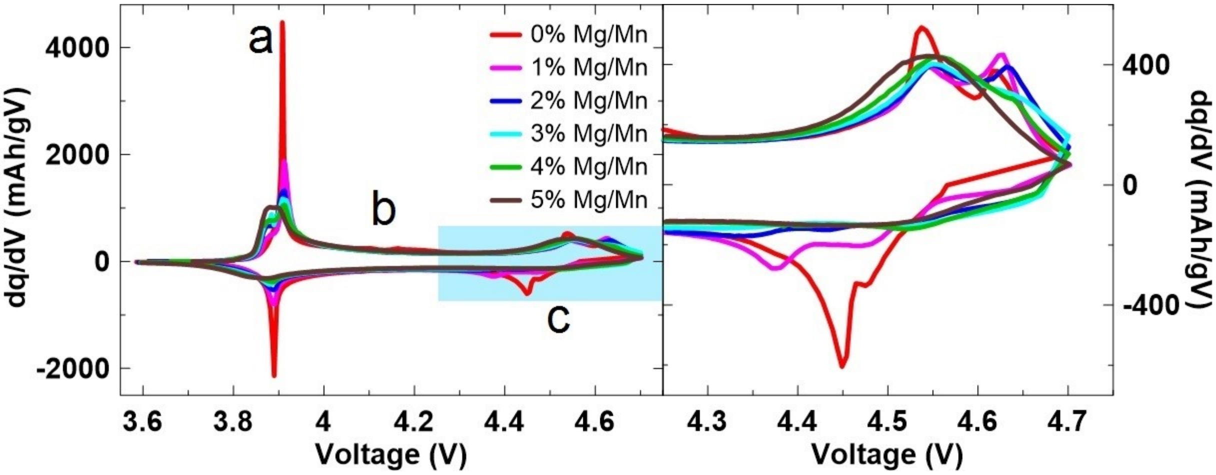

Figure 3.12: Differential capacity (dq/dV) as a function of voltage of MM0-MM5 cells cycled between 3.6 V and 4.7 V. An enlarged view of the high voltage region is shown in the right panel. The data was collected at 30°C using a specific current of ~5 mA/g (C/50).

The first feature, denoted as "a" in Fig. 3.12, is the sharp peak at 3.9 V, which signifies the 2 phase insulator-metal transition.[74] This peak shrank and broadened to a voltage range of 3.87-3.9 V as Mg/Mn substitution increased, and has been reported in past results.[23,85] Levasseur *et al.* reported $LiCo_{0.95}Mg_{0.05}O_2$ to be monophasic, but the dx/dV vs V data (Fig. 1 in the article, x = Li content) suggested the occurrence of a transition.[85] From this example as well as the current study, the inclusion of Mg appears to ease this transition as seen by the lower voltage of the peak, but it is uncertain at what Mg content the material ceased to undergo a 2 phase transition, if it did at all. The growth of the peak at 3.87 V along with the reduction of the 3.9 V peak suggest that Mg alters its local environment, facilitating this insulator-metal transition for Li, while further Li are unaffected and experience the transition at the usual 3.9 V. It is uncertain why only one other peak arose and why the peaks remained at the same voltage unlike past examples of different Li sites.[134] Perhaps the Mg/Mn content was low enough to only provide one alternative site for the Li. Interestingly, while this transition occurred in different voltage ranges depending on the Mg/Mn content, the Li content range seem to be consistent (discussed later in Chapter 4).

The next feature in Fig. 3.12, feature “b”, was the loss of the order-disorder transition at 0.5 Li. As Mg/Mn content increases, the dopants changed the lithium-host interaction and disrupted the stabilizing effect of ordering the Li ions.[135] The transition was reduced, but can still be seen at 1% Mg/Mn, and disappeared altogether after 2% Mg/Mn.

The third feature, shown as “c” in Fig. 3.12, was the transition of the 2 high voltage peaks to one broad peak. The dq/dV features associated with the O3-O6-O1 phase transitions seen at high voltage (> 4.5 V)[26,72] gradually disappear as Mg/Mn content increases. This will be discussed further in the next section (Section 3.3.2).

3.3.2 Comparing Second Cycle Data to First Cycle Data

Figure 3.13 shows cell voltage as a function of capacity for the 1st cycle (solid line) and the 2nd cycle (dashed line) for MM0-MM5 cells. The differing discharge capacities of the 1st cycle were retained in the 2nd cycle without much change, which lead the 6 sets of cells to return to similar capacities at the end of the 2nd cycle. This seems to indicate that the effects of Mg/Mn substitution remained consistent after the 1st cycle and that no new changes occurred. This was confirmed in the in situ XRD study (Chapter 4).

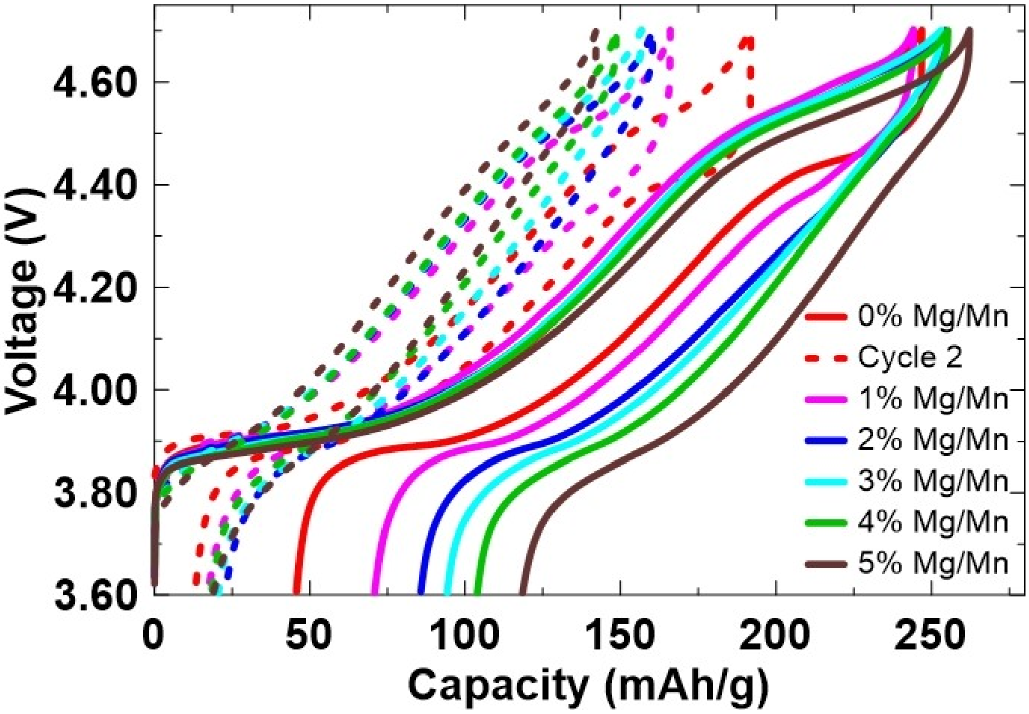

Figure 3.13: Cell voltage as a function of capacity for the first cycle (solid line) and second cycle (dashed line) for MM0-MM5 cells. The data was collected at 30°C using a specific current of ~5 mA/g (C/50).

As discussed in Section 3.3.1, a case can be made for how electrolyte decomposition can cause increasing irreversible capacity as Mg/Mn content increased based on the 1st cycle (Fig. 3.11). If that were the case, 2nd cycle capacity trends should be similar to the 1st cycle, where charge capacities were similar across all samples but discharge capacities would decrease as Mg/Mn content increased. However, based on the similar 2nd cycle irreversible capacities that all sets of cells experienced (Fig. 3.13), this clearly refutes that possibility. Another possible scenario is that electrolyte decomposition only occurred in the first charge to high voltage and the reaction formed an SEI which impedes further decomposition. This will be discussed in the next section.

Figure 3.14 shows a comparison of dq/dV vs V as a function of voltage for the 1st cycle (solid line) and the 2nd cycle (dashed line) in the high voltage region. As more Mg/Mn was incorporated into material, there was a decrease in high voltage capacity during the 2nd cycle. This suggests that as the Mg/Mn concentration increased, the material progressed from undergoing reversible phase transitions to experiencing irreversible oxygen loss.

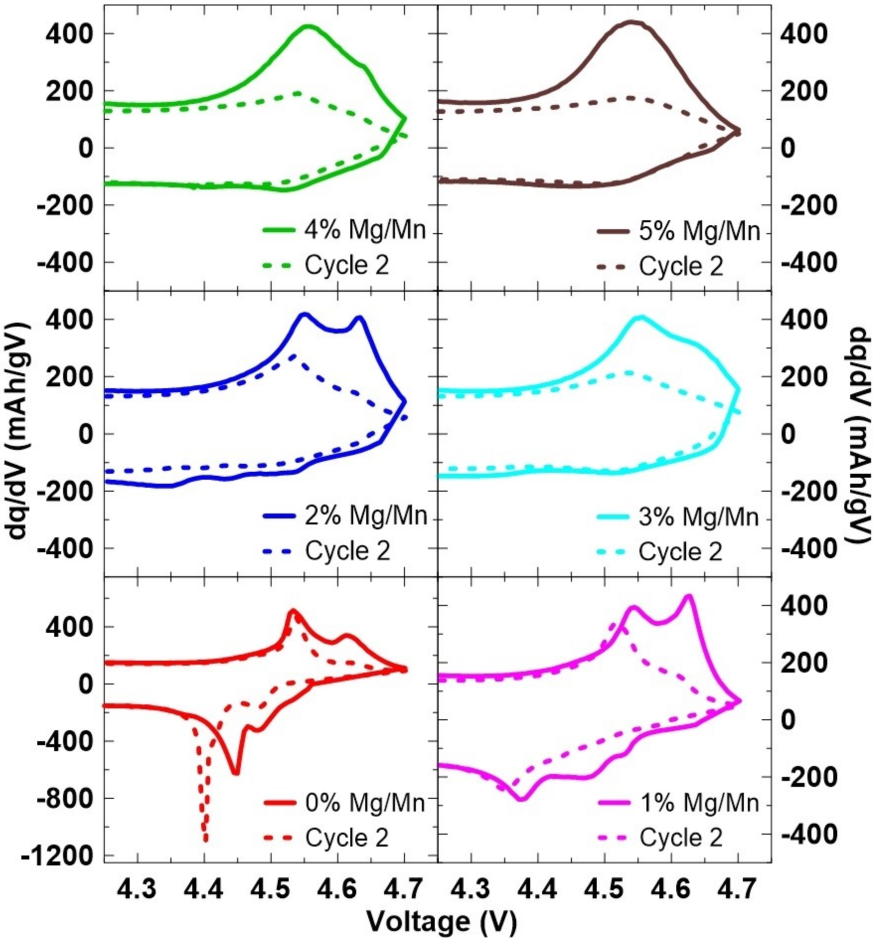

Figure 3.14: Differential capacity (dq/dV) as a function of voltage for the first cycle (solid line) and second cycle (dashed line) for MM0-MM5 cells at high voltage. The data was collected at 30°C using a specific current of ~5 mA/g (C/50).

Oxygen redox may be able to explain the 1st charge capacity trend noted in Fig. 3.11b. As discussed earlier, the trend may be explained by assuming delithiation to similar Li content, but there are not enough electrochemically active ions to obtain the capacities for samples with high Mg/Mn content (5% Mg/Mn has a theoretical capacity of 251 mAh/g based on the available Co^{+3}/Co^{+4}). The inclusion of an oxygen redox mechanism allows delithiation to continue.

Oxygen redox processes are reversible only if the oxygen oxidation is stabilized by the formation of peroxo-like species.[136] However, the formation of peroxo-like species only occurs under certain conditions which allow neighbouring oxidized oxygens to rotate. Theoretical studies by Seo *et al*. found that the rotation required to form peroxo-like species is facilitated when the oxygen is bonded to a low amount of metal ions, and when the metal ions do not have partially filled *d* shells.[137] This suggests that reversible oxygen oxidation is not occurring in this study, as stoichiometric Li ratios do not reduce the amount of metal ions bonded to oxygen. Out of the 3 metals in the M layer, only Mg does not have partially filled *d* shells. However, the low concentration of Mg makes it unlikely to form a significant amount of peroxo-like species, even if oxygens were bonded to fewer metal ions. Additionally, McCalla *et al*. suggested that peroxo-like species formed below 4.3 V will be stable against the formation of oxygen gas.[138] This was not the case in this study, as the oxygen redox did not occur until around 4.5 V, further disputing reversible oxygen oxidation for these materials.

If oxygen redox does not form peroxo-like species, the oxygen undergoes an irreversible oxidation resulting in the formation of oxygen gas, which is then lost.[136] Fig. 3.14 suggests that this was the case. When 1st cycle differential capacity vs. voltage shows a large peak around 4.5 V but subsequent cycles do not, it suggests that the peak was due to an irreversible process, likely stemming from oxygen loss.[139,140] The loss of oxygen may have locked the affected CoO_2 slabs in position, preventing the slabs to shift to the O1 structure. Small numbers of oxygen deficient CoO_2 slabs may still allow the formation of the O6 phase while preventing O1 phase formation. Perhaps this can explain the trend seen in Fig. 3.12 where the dq/dV vs. V peak corresponding to the O6-O1 transition disappeared before change became noticeable for the O3-O6 transition.

3.3.3 Long Term Cycling Performance

Figure 3.15 shows long term cycling data (discharge capacity (a), relative discharge capacity (b), and ΔV at top of charge (c) as a function of cycle number). Relative discharge capacities (Fig. 3.15b) were calculated relative to the first discharge capacity. ΔV_{TOC} is the change of cell voltage when the cell switched from charge to discharge currents and is used as an indicator of cell resistance. Since the first two cycles used a current corresponding to C/50 while subsequent cycles used a current corresponding to C/5, a decrease of discharge capacities seen at that step is expected. Figs. 3.15a and 3.15b show that adding 1% of Mg/Mn to LCO improved the cycling performance (to 4.7 V) of the material (after 51 cycles, 0% Mg/Mn retained less than 1% of 1st discharge capacity, whereas around 30% capacity was retained for 1% Mg/Mn). However, increasing Mg/Mn substitution above 1% did not seem to compound improvements. Cells with 1-5% Mg/Mn content had similar cycling performance. After 51 cycles, 25-35% capacity was retained with no clear trend. This variation likely stemmed from the nature of coin cell fabrication. Fig 3.15c confirms this data, with 0%

Mg/Mn having experienced a large ΔV_{TOC} of 1.225 V on the 51st cycle while 1-5% Mg/Mn experienced less ΔV_{TOC} (0.408-0.630 V for the 51st cycle).

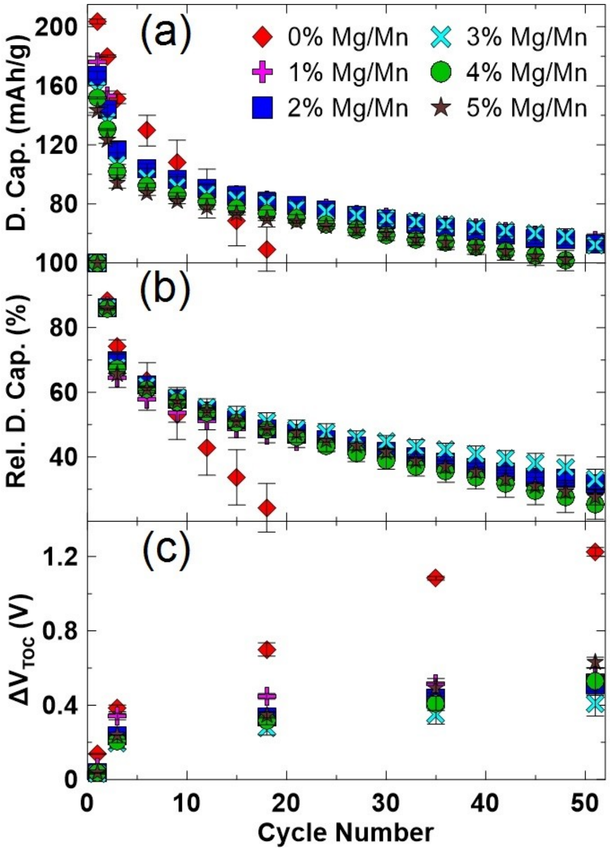

Figure 3.15: Discharge capacity (a), relative discharge capacity (b), and ΔV at top of charge (c) as a function of cycles for MM0-MM5 cells. The data was collected at 30°C using a specific current of ~5 mA/g (C/50) for the first 2 cycles and ~50 mA/g (C/5) for all other cycles.

A closer look at Fig. 3.15c shows that the ΔV_{TOC} of MM0 cells were already larger than other cells after the 1st cycle. SEI formation is associated with an increase in cell resistance,[12,17] and thicker SEI layers with larger increases in cell resistance. This suggests that cells with higher Mg/Mn content did not experience more electrolyte decomposition and SEI formation.

Cycling performance was improved with even 1% Mg/Mn in the material (Fig. 3.15). As seen in Fig. 3.12, materials with 1% Mg/Mn still appeared to be undergoing the O3-O6-O1 phase transitions at low lithium content. The inclusion of any Mg/Mn suppressed the growth of the ΔV_{TOC} experienced by LCO while cycling, which suggests that Mg/Mn improved cycling performance by minimizing the growth of resistance as cells cycled and not by suppressing the O3-O6-O1 phase transitions.

While the improvements in cycling performance were quite significant once any Mg/Mn substitution occurred, all the cells still retained less than 50% capacity after 50 cycles. However, many known protocols to optimize high voltage cycling such as particle properties,[105,106,108] coatings,[24,26,37–39,66,141] and electrolyte optimization[13,15–17,39] were not included in this study which focused on the effects of Mg/Mn substitution.

This initial set of experiments gave valuable insights to how doping LCO with Mg and Mn affected its properties and performance. The next chapter will discuss other investigations that arose after this initial set of experiments.

Chapter 4 – Additional Studies on Mg/Mn Doped LCO

Having learned that the addition of Mg/Mn to LCO improved long term cycling performance, but increased irreversible capacity in Chapter 3, this chapter will discuss further experiments performed to explore the effects of cycling to different upper cutoff voltages (Section 4.1) as well as in situ XRD studies of the samples (Section 4.2).

4.1 Varying the Upper Cutoff Voltage (UCV) of Mg/Mn Doped LCO Coin Cells

Section 3.3 investigated the electrochemical performance of Mg/Mn doped LCO, and it was found that increasing the Mg/Mn content increased the irreversible capacity. The cells were cycled between 3.6 V and 4.7 V, which is an aggressive protocol as discussed in Section 1.4.1. The behavior of LCO and Mg/Mn doped LCO materials as cells experience higher and higher voltages was explored.

Sets of MM0 and MM5 cells were cycled between 3.6 V and various upper cutoff voltages (UCVs, 4.3-4.7 V) at 30°C as described in Section 2.6. The first two cycles used a current corresponding to C/50 while all subsequent cycles used a current corresponding to C/5. Several cells for each UCV were fabricated, but data from only one cell was shown for cell voltage versus capacity and differential capacity versus voltage plots. Table 4.1 lists the theoretical capacities used to determine current densities at which cells will cycle at. Theoretical capacity values were estimated from data in Section 3.3, and LCO literature values were checked for agreement. Once again, results and discussions will be divided into three sections: first cycle data (Section 4.1.1), comparison of first and second cycle (Section 4.1.2) and long term cycling performance (Section 4.1.3).

Table 4.1: A list of theoretical capacities used for calculating MM0 and MM5 current densities.

Upper Cutoff Voltage (V)	**0% Mg/Mn Theoretical Capacitiy (mAh/g)**	**5% Mg/Mn Theoretical Capacity (mAh/g)**
4.7	250	260
4.6	230	240
4.5	190	195
4.4	170	170
4.3	155	155

4.1.1 First Cycle Data

Figure 4.1 shows the cell voltage vs. capacity (a) and the dq/dV vs. voltage (b) for the first cycle of 0% Mg/Mn cells cycling to increasing UCVs. As MM0 cells cycled to higher UCVs, the first cycle charge capacity and irreversible capacity both increased as expected. First cycle data will be discussed further in Figure 4.3. The dq/dV peaks (Fig. 4.1b) corresponding to the insulator-metal transition upon charge and discharge both substantially exceeded the y-axis limit since the axis was limited to a range of -2000 mAh/gV to 2000 mAh/gV to maintain clarity of the high voltage region.

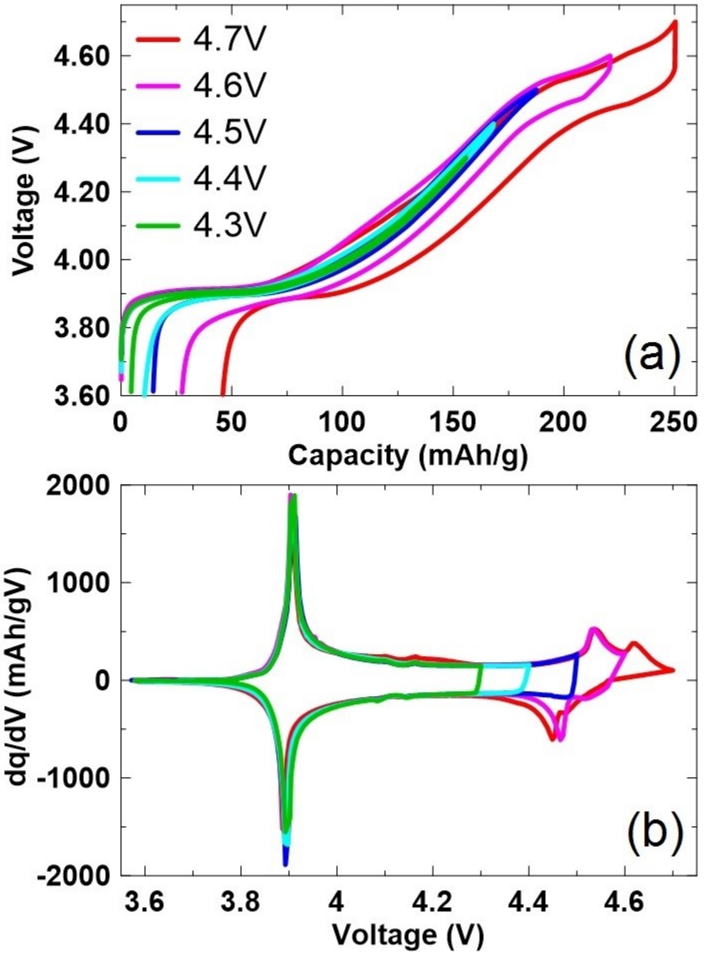

Figure 4.1: First cycle (a) cell voltage vs. capacity and (b) differential capacity vs. voltage for MM0 cells cycled between 3.6 V and 4.3-4.7 V. The data was collected at 30°C using a current corresponding to C/50.

Cells generally followed similar progressions during the first charge as UCVs increased in both Fig 4.1a and Fig. 4.1b. Upon discharge, MM0 cells cycling to a UCV of 4.3-4.5 V had similar dq/dV profiles, and their irreversible capacities were similar. Fig. 4.1a shows that as the UCV increased to 4.6 V and above, the irreversible capacity started to increase significantly. Fig 4.1b shows that these cells experienced the low lithium content phase transitions (O3-O6 phase transitions for cells cycling to 4.6 V, and

O3-O6-O1 phase transitions for cells cycling to 4.7 V). These phase transitions may contribute to the increase of irreversible capacity.

Figure 4.2 shows the cell voltage vs. capacity in panel (a) and the dq/dV vs. voltage in panel (b) for the first cycle of MM5 cells cycling to increasing UCVs. Similar to MM0 cells in Fig. 4.1, MM5 cells cycled to higher UCVs experienced increasing charge capacity and irreversible capacity in the first cycle.

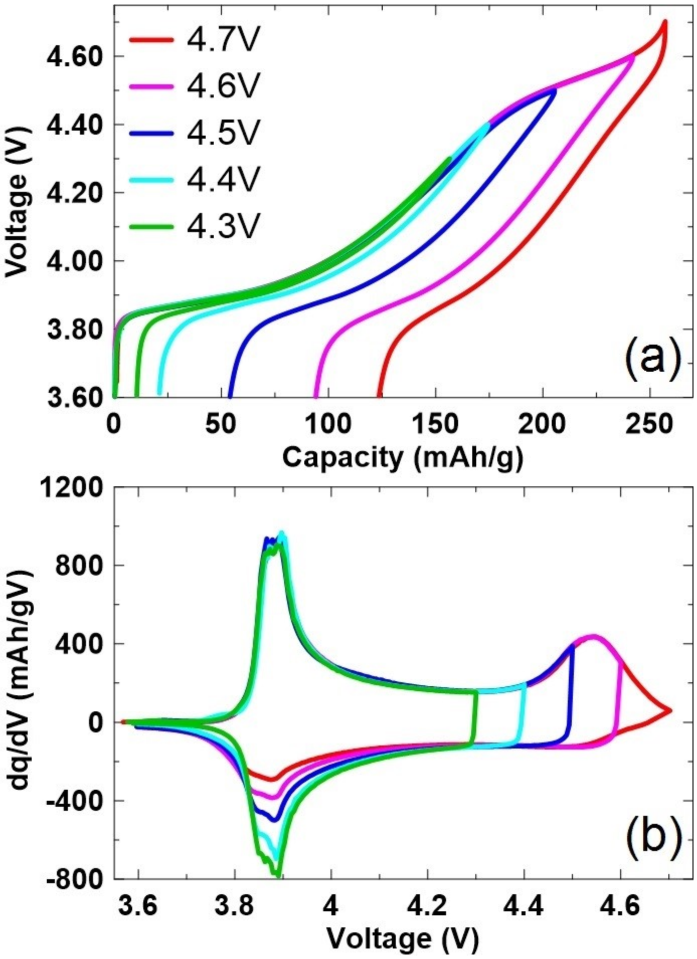

Figure 4.2: First cycle (a) cell voltage vs. capacity and (b) differential capacity vs. voltage for MM5 cells cycled between 3.6 V and 4.3-4.7 V. The data was collected at 30°C using a current corresponding to C/50.

Like 0% Mg/Mn cells, 5% Mg/Mn cells followed similar progressions during the first charge as UCVs increased. However, irreversible capacity started to increase significantly starting at an upper cutoff voltage of 4.5 V. Once again, this increase corresponded to cells traversing the dq/dV peak at high voltage, which was linked to oxygen loss for MM5 cells in Section 3.3.2. While the dq/dV profiles for the first charge were all comparable, the dq/dV peak corresponding to the insulator-metal transition shrank with increasing UCV during discharge. This was not seen in MM0 cells (Fig 4.1b), where there were no noticeable trends. This phenomenon that MM5 cells experienced suggests that relithiation of the positive electrode material progressed through less of the insulator-metal transition as UCV increased. It is uncertain whether this was due to oxygen loss affecting the material or due to relithiation stopping earlier in the transition because of the increasing irreversible capacity.

Figure 4.3 shows the 1st charge capacity (a), 1st discharge capacity (b), and 1st cycle irreversible capacity (c) for MM0 and MM5 cells cycled to different UCVs. Both MM0 and MM5 cells had similar charge capacities at the different UCVs (a maximum difference of 11 mAh/g at 4.7 V). However, their discharge capacities and irreversible capacities started to differentiate at 4.5 V and above (a difference of 5 mAh/g and 3.8% at 4.3 V and a difference of 59 mAh/g and 26% for 4.7 V).

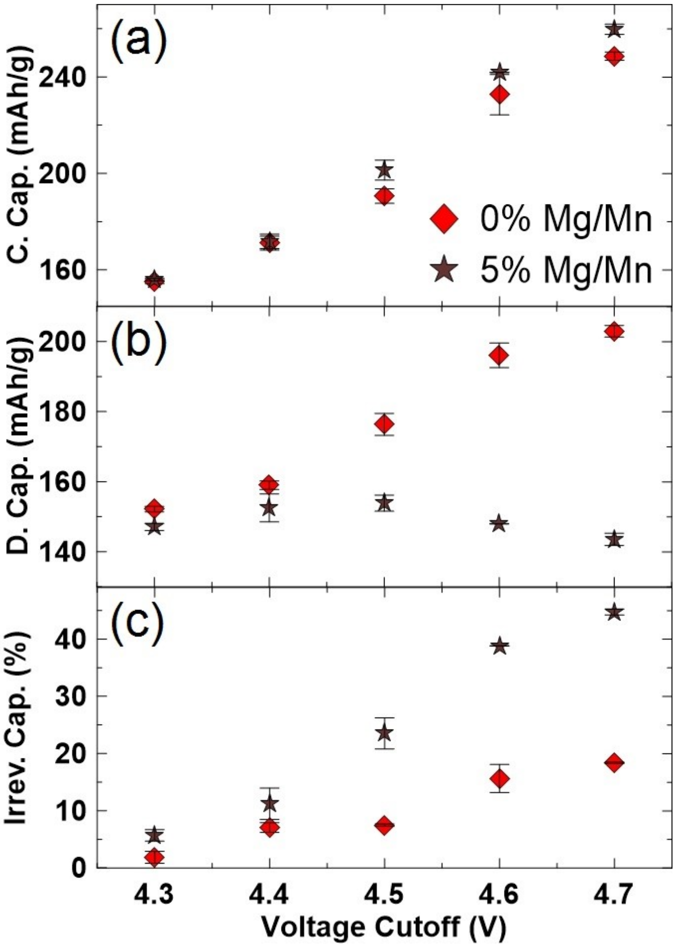

Figure 4.3: First cycle (a) charge capacity, (b) discharge capacity, and (c) irreversible capacity for MM0 and MM5 cells cycled between 3.6 V and various upper cutoff voltages. The data was collected at 30°C using a current corresponding to C/50.

The differences in discharge capacity (Fig. 4.3b) and irreversible capacity (Fig. 4.3c) started to occur around where 5% Mg/Mn cells started experiencing oxygen loss. While 0% Mg/Mn cells also started to experience an increase in irreversible capacity when the O3-O6 phase transition began to occur at 4.6 V, the irreversible capacity experienced by MM0 cells cycling to 4.7 V was less than the irreversible capacity experienced by MM5 cells cycling to 4.5 V. This suggests that the loss of oxygen contributes significantly to limiting the amount of reintercalated lithium.

4.1.2 Comparing Second Cycle Data to First Cycle Data

Figure 4.4 shows cell voltage as a function of capacity for the 1st cycle (solid line) and the 2nd cycle (dashed line) for the set of MM0 cells cycling to various UCVs. Unlike Fig. 3.13, the 5 sets of MM0 cells did not return to similar capacities after the 2nd cycle. While 2nd cycle irreversible capacities were less than that experienced in the 1st cycle, cells cycling to higher UCVs still had more irreversible capacity.

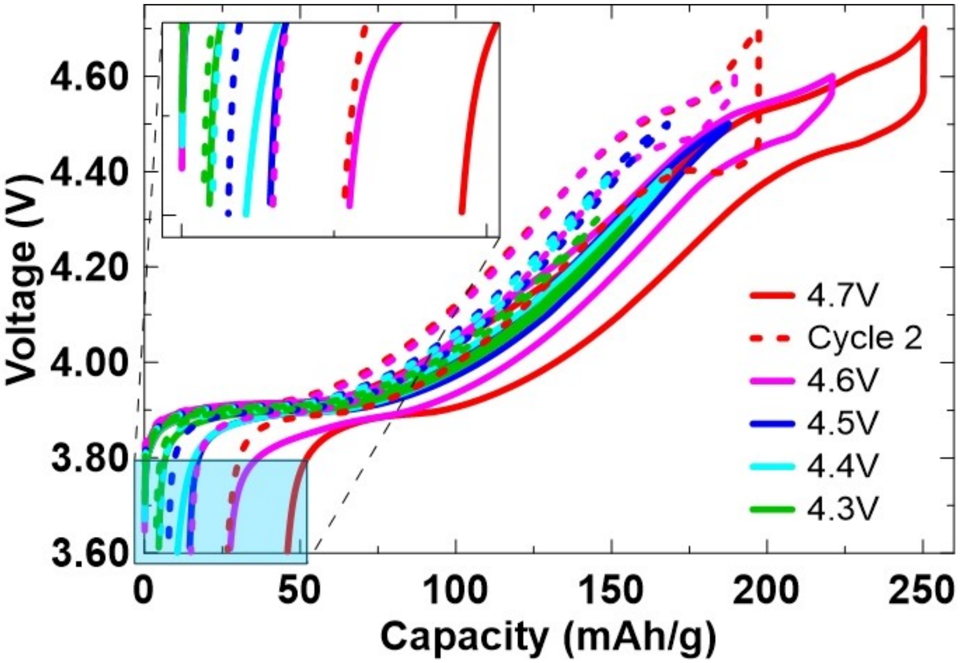

Figure 4.4: Cell voltage as a function of capacity for the first cycle (solid line) and second cycle (dashed line) for MM0 cells cycling to various UCVs. The data was collected at 30°C using a current corresponding to C/50.

Figure 4.5 shows cell voltage as a function of capacity for the 1st cycle (solid line) and the 2nd cycle (dashed line) for the set of MM5 cells cycling to various UCVs. Like MM0 cells (Fig. 4.4), the 5 sets of MM5 cells did not return to similar capacities after the

2^{nd} cycle. Once again, cells cycling to higher UCVs experienced more irreversible capacity.

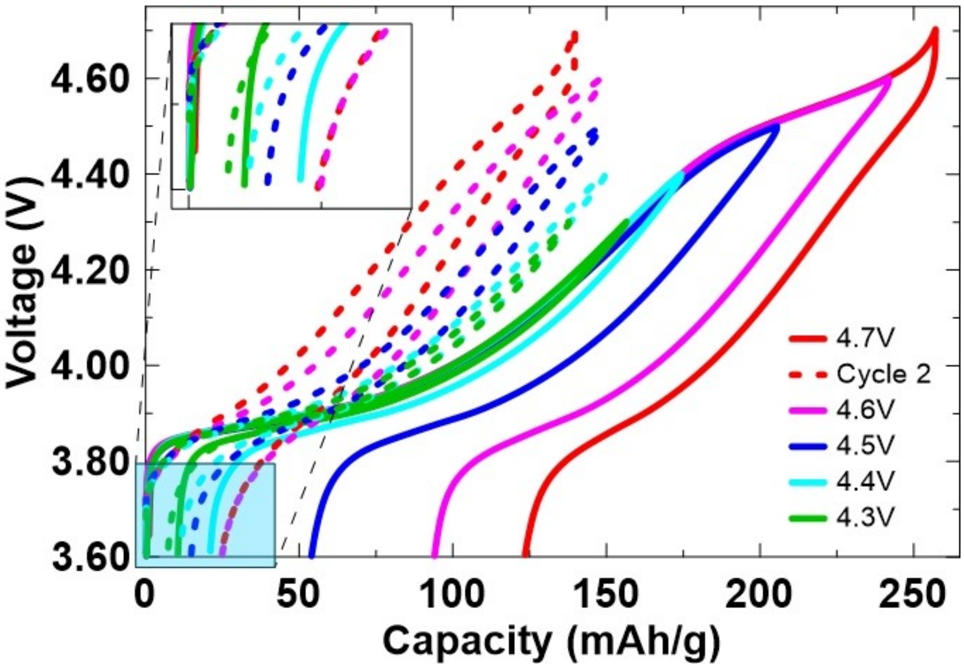

Figure 4.5: Cell voltage as a function of capacity for the first cycle (solid line) and second cycle (dashed line) for MM0 cells cycling to various UCVs. The data was collected at 30°C using a current corresponding to C/50.

Previously in Section 3.3.2, the comparison of second cycle data to first cycle data was used to determine whether electrolyte degradation contributed to differences in irreversible capacity of cells with various Mg/Mn content. In that case, similar irreversible capacities during the 2^{nd} cycle refuted electrolyte degradation as contributing to the differences in irreversible capacities seen in the 1^{st} cycle. Figs. 4.4 and 4.5 show that cells cycling to higher UCVs still experienced more irreversible capacity, so electrolyte degradation cannot be ruled out as a factor. This factor appears to be more pronounced when cells were cycled to 4.6 V or higher, but a more focused investigation is needed to determine when irreversible capacity starts to rapidly increase.

4.1.3 Long Term Cycling Performance

Figure 4.6 shows long term cycling data for 0% Mg/Mn (1) and 5% Mg/Mn (2) cells. Similar to Fig. 3.15, ΔV_{TOC}, shown in Figs. 4.6c1 and 4.6c2, was a good indicator of cycling performance. Cells cycling to 4.6 V experienced an increase in ΔV_{TOC} and their cycling performance worsened compared to cells cycling to a lower voltage. Incorporation of 5% Mg/Mn into LCO did not bring benefits to cycling performance (when compared to LCO cells with the same UCV) until cells cycled to 4.7 V.

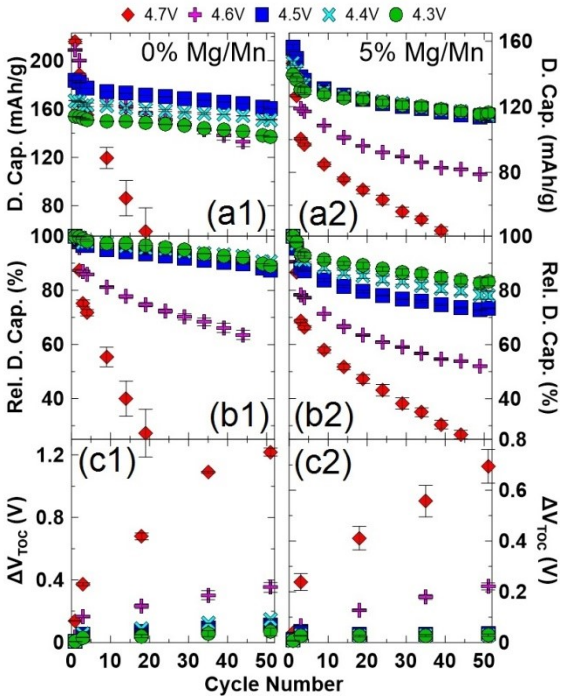

Figure 4.6: Discharge capacity (a), relative discharge capacity (b), and ΔV at top of charge (c) as a function of cycles for MM0 (1) and MM5 (2) cells cycled between 3.6 V and various upper cutoff voltages. The data was collected at 30°C using a current corresponding to C/50 for the first 2 cycles and C/5 for all other cycles.

As seen in Fig. 4.6, 0% Mg/Mn cells cycling at 4.5 V experienced a ΔV_{TOC} of 0.004 V and retained 87% of 1st discharge capacity after 51 cycles, while cells cycled to 4.6 V experienced a ΔV_{TOC} of 0.35 V and retained 63% capacity after 46 cycles (ΔV_{TOC} of 0.036 V and 73% capacity at 4.5 V and ΔV_{TOC} of 0.22 V and 52% capacity at 4.6 V for 5% Mg/Mn cells). Testing to 4.7 V further increased ΔV_{TOC} and worsened cycling performance (Figs. 3.15 and 4.6). At every UCV, MM5 cells experienced smaller ΔV_{TOC} than MM0 cells.

While 5% Mg/Mn cells cycling to 4.5 V started to experience more irreversible capacity, only a slight decrease of cycling performance (Fig. 4.6b2) and no significant increase in ΔV_{TOC} was observed (Fig. 4.6c2). This suggests that first cycle irreversible capacity may not be an indicator of long term cycling performance. Both MM0 and MM5 cell cycling performance deteriorated starting at an upper cutoff voltage of 4.6 V, which was when MM0 started to undergo its O3-O6 phase transition (Fig. 4.1b) and MM5 was in the middle of its oxygen loss dq/dV peak (Fig. 4.2b). While it was suggested that 5% Mg/Mn cells start experiencing oxygen loss at 4.5 V (Fig. 4.2b), it is uncertain these events cause the growth of ΔV_{TOC} and cycling performance deterioration. Perhaps another mechanism, such as electrolyte degradation or structural instability, may be the reason for this decline in cycling performance at 4.6 V. The next section investigates the structural changes of the positive electrode material during cycling to 4.7 V.

4.2 In Situ XRD Study of Mg/Mn Doped LCO Coin Cells

Section 4.1 investigated the effect of varying upper cutoff voltages on first cycle irreversible capacity and long term cycling performance. While electrolyte degradation was ruled out as a factor for increasing irreversible capacity with increasing Mg/Mn content (Section 3.3.2), it cannot be ruled out as a factor for increasing irreversible capacity with increasing UCVs (Section 4.1.2). While a likely contributor to cycling performance deterioration, it is uncertain if it is the only factor. Structural instability from cycling may also impact cycling performance, so in situ XRD experiments were carried out as described in Section 2.7.1. In situ XRD measurements were made for 0%, 2%, and 5% Mg/Mn cells to track lattice parameters and phases present throughout the delithiation and lithiation processes of the positive electrodes. In situ XRD studies of MM0, MM2 and MM5 cells will be discussed in Sections 4.2.1-3 and Section 4.2.4 will compare all three studies together.

4.2.1 In Situ XRD Study of 0% Mg/Mn

Figure 4.7 shows (a) the in situ XRD scans of an MM0 cell along with the corresponding voltages at which the scans took place along with (b) an expanded view of the (003) reflection in the high voltage region (> 4.5 V). The (003) reflection had a disproportionately high number of counts, so it is reported in counts per second while all other panels are reported in total counts. As the material entered the high voltage region, the O3-O6-O1 phase transitions that occur were easily discernable in the XRD scans, with the reflections showing a noticeable shift. These shifts reversed during discharge and were seen again on the 2nd charge, indicating the reversibility of the transitions. Looking at Fig. 4.7b, the O6 peak (*) developed clearly but the O1 peak (v) was just starting to emerge as the cell switched from charge to discharge. This was due to the charging protocol not allowing for full delithiation, so only a portion of the material was delithiated enough to transition into the O1 phase.

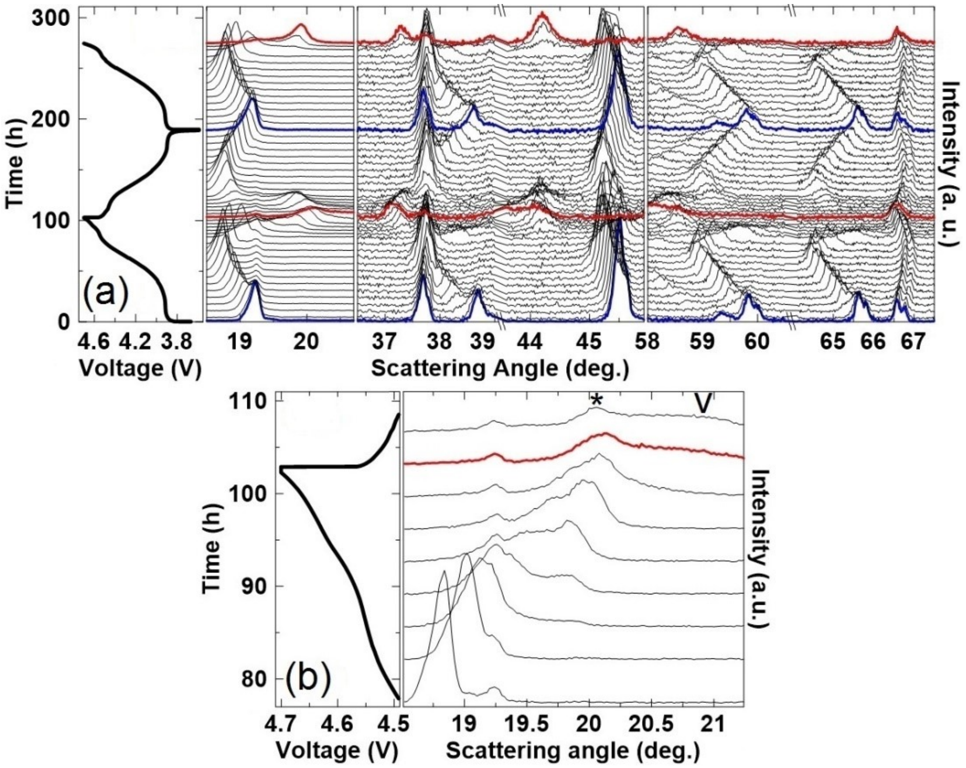

Figure 4.7: Cell voltages and in situ XRD patterns (Cu K_α radiation) of MM0. Panel a shows the full experiment while panel b shows an expanded view of the (003) reflection at high voltage (> 4.5 V) for the first cycle. Every 2^{nd} is shown except at high voltage (> 4.5 V) where every scan is shown. (*) shows the emergence of the O6 phase while (v) shows the emergence of the O1 phase. The data was collected at room temperature using a specific current of ~2.5 mA/g (C/100).

The X-ray beam width at lower scattering angles was slightly wider than the electrode size, which affected the intensity of the (003) peak compared to the rest of scattering angle regions. The stationary peak around a scattering angle of 19.25° (Fig.

4.7b) was observed because the X-ray beam footprint was wide at low scattering angles. Unused electrode on the edges, due to being electrically disconnected, was measured at low scattering angles but not higher angles due to the decreasing size of the X-ray footprint on the sample as the scattering angle increased.

The phases were refined as described in Section 2.7.2 with the exception of the O1 phase, which did not appear enough to be refined. The O3 phase was refined in the $R\bar{3}m$ space group, Li was assumed to occupy the 3a sites (lithium layer) while the 3b sites (metal layer) contained only Co and oxygen occupied the 6c sites. An unused electrode phase, which was the O3 phase refined for the 1st scan, was included when two (003) reflection peaks could be seen. Only the phase scale and preferred orientation were varied for the unused electrode phase. For the O6 phase (still $R\bar{3}m$ space group), Li was assumed to occupy the 3a sites, with Co and two oxygens occupying the 6c site (starting z = 0.42, 0.27, and 0.11 respectively). The monoclinic phase was in the C2 space group, with Li occupying 2a and 4c sites, Co occupying 2b and 4c sites, and three oxygens occupying 4c sites.[71] For all phases, Li occupations were not refined as Li is not a strong scatterer. Li occupancies were assumed to be 1 for O3, 0.5 for monoclinic, and 1/6 for O6 phases. Due to the beam width issue discussed above, preferred orientation of the (003) reflection was also refined ((006) reflection for O6 phase).

Figure 4.8 shows the measured and calculated XRD patterns for selected scans seen in Fig. 4.7. The scans shown are scans corresponding to the first scan and 1st bottom of charge (scan 1), a scan showing the unused phase (scan 10), the monoclinic phase (scan 18), the O6 phase and 1st top of charge (Scan 31), the 2nd bottom of charge (scan 60), and the 2nd top of charge (scan 84). Due to measuring only selected ranges, the quality of the fits did not match those in Chapter 3. However, fitting the in situ XRD patterns sequentially helped maintained stability while refining. .

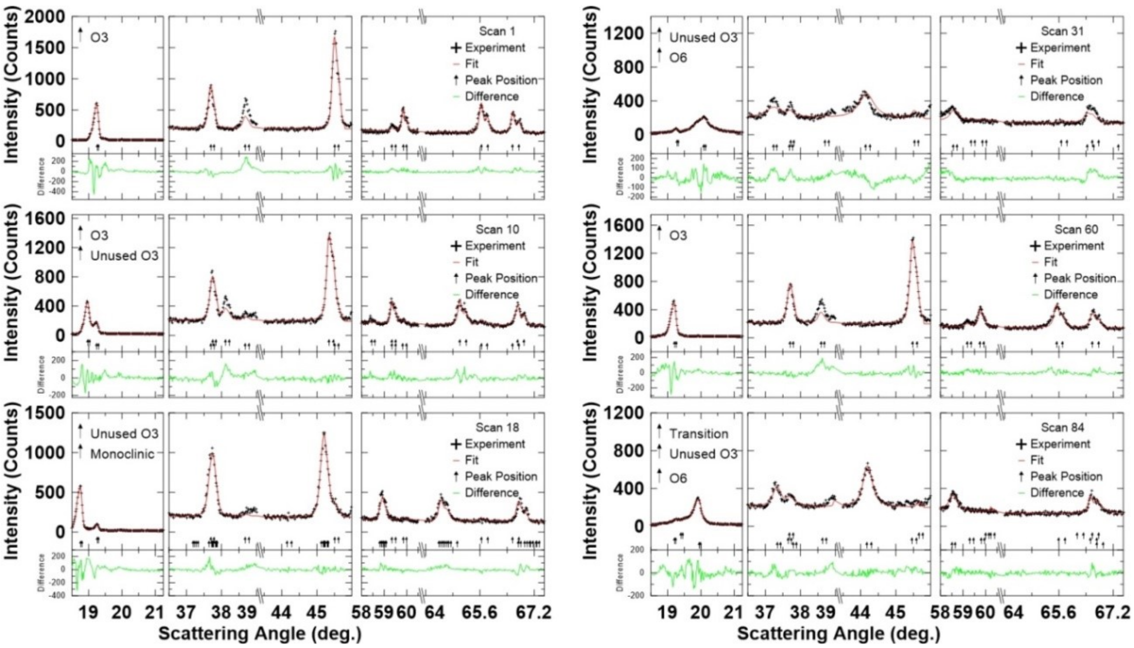

Figure 4.8: In situ XRD Rietveld refinement pattern fitting for MM0. Only selected scans and reflections are shown in this figure. (003) reflection peaks are depicted as counts per seconds, but the calculated differences were kept as total counts. The peak positions of the different phases are ordered from top to bottom with the phases indicated in the left panel of each scan.

Scan 84 contains a “transition” phase, which was used to fit the broad O3-O6 transition. Lattice parameters were not reported for the “transition” phase, which was used in scans 34 and 84. Just like in Fig. 4.7, the (003) reflection is reported in counts per seconds, but Rietveld refinement was conducted in total counts, and the difference reported is kept in total counts. A table of Rietveld refinement results for MM0 can be found in Appendix B. Table B.1 details the phases present, their scale factors and lattice parameters as well as the Bragg R-factors of each scan shown in Fig. 4.7a.

Figure 4.9 shows Rietveld refinement results for 0% Mg/Mn from the in-situ XRD experiment. The top panels show cell voltage as a function of time, and the bottom 3 panels show the corresponding phase weight fractions and lattice parameters as a function of scan number.

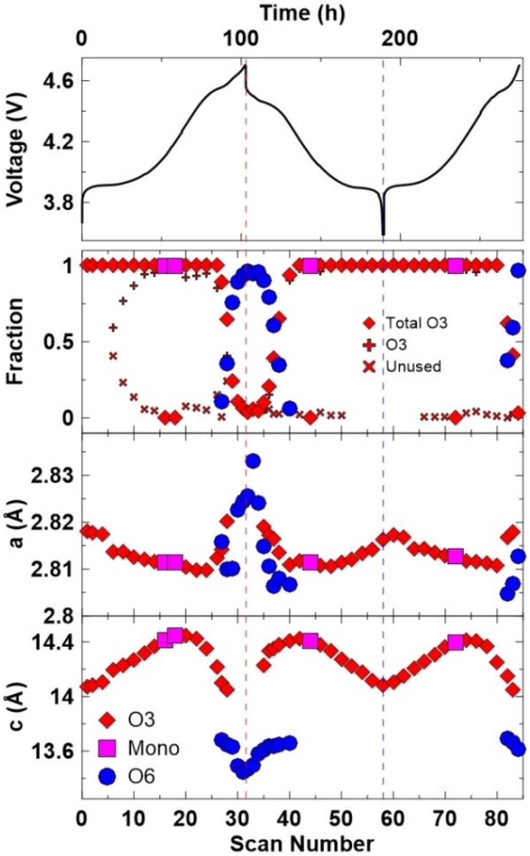

Figure 4.9: Cell voltage, phase weight fractions, *a*-axis, and *c*-axis are shown versus scan number for the MM0 in situ XRD experiment. Results from every 2^{nd} scan are shown except at high voltage (> 4.5 V) where results from every scan are shown. Lattice parameters reported have been converted to the O3 unit cell. The data was collected at room temperature using a specific current of ~2.5 mA/g (C/100). Error bars were not included in the figure for clarity, but can be found in Table B.1.

The lattice parameters reported for the different phases were converted to the O3 unit cell as described in Section 2.7.2. The monoclinic phase lattice parameters were very similar to the O3 phases of similar composition. The emergence of the O6 phase coincided with an increase in the *a*-axis and a large decrease in the *c*-axis, which was unsurprising due to the alternating empty Li layers of the O6 phase. Both the monoclinic phase and the O6 phases were present during the subsequent charge, indicating that these phase transitions are reversible.

Lattice parameter variation and phase presence for 0% Mg/Mn (Fig. 4.9) match well qualitatively with past results.[68,71] The O1 phase can be seen emerging in Fig. 4.7b, but could not be refined. The expectation is for the *c*-axis to experience another decrease as the material transitions to the O1 phase,[74] and Fig. 4.7b shows the (003) reflection of the O1 phase to appear at a higher angle than the O6 phase, corroborating the expectation. The inclusion of the unused electrode phase meant that the 2-phase insulator-metal transition at high lithium concentrations[71,74] could not be investigated as the insulator phase lattice constants do not vary,[71] hiding it within the unused electrode phase.

4.2.2 In Situ XRD Study of 2% Mg/Mn

Figure 4.10 shows the in situ XRD scans of an MM2 cell along with the corresponding voltages at which the scans took place (a) along with an expanded view of the (003) reflection in the high voltage region (b). Similar to Fig. 4.7, as the material entered the high voltage region, the (003) reflection showed a shift associated with the

O3-O6-O1 phase transitions (Fig. 4.10b). However, this shift was not as noticeable as Fig. 4.7b, and Fig. 4.10b only shows the appearance of the O6 peak (*) but no O1 peak.

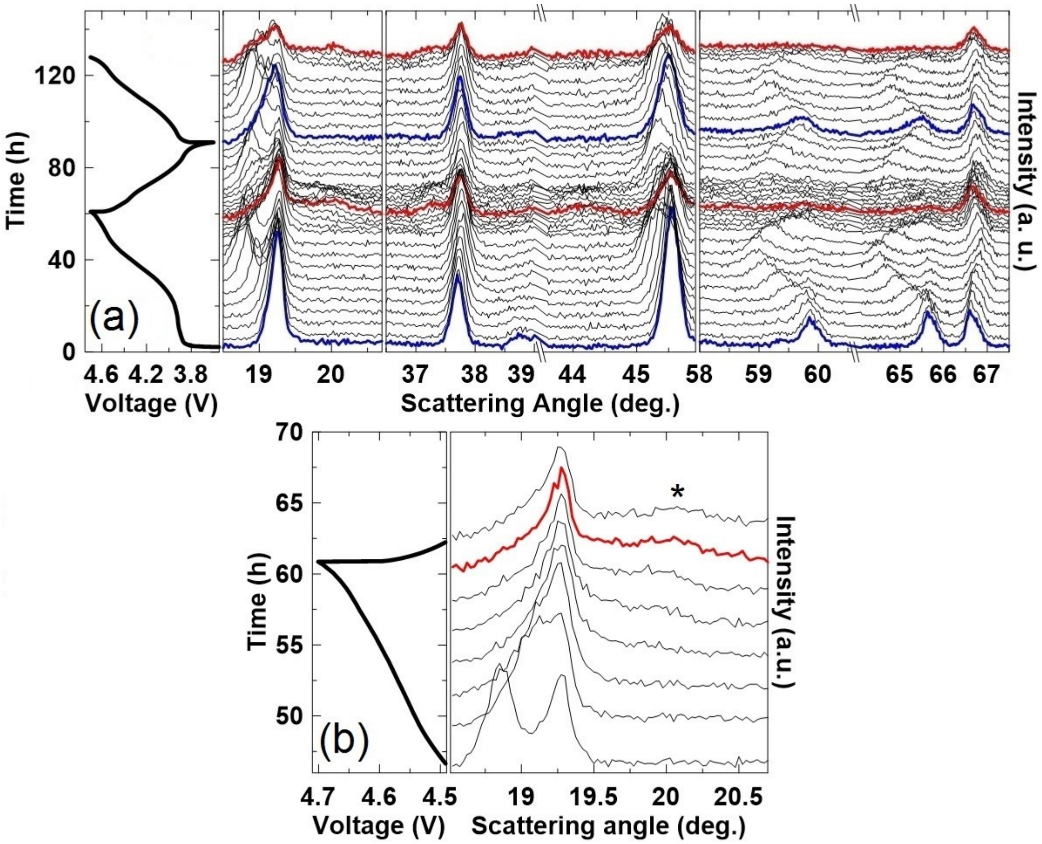

Figure 4.10: Cell voltages and in situ XRD patterns (Cu K$_\alpha$ radiation) of MM2. Panel a shows the full experiment while panel b shows an expanded view of the (003) reflection at high voltage (> 4.5 V) for the first cycle. Every 3rd scan is shown except at high voltage (> 4.5 V) where every scan is shown. (*) shows the emergence of the O6 phase. The data was collected at room temperature using a specific current of ~5 mA/g (C/50).

The in situ XRD study of MM2 showed large amounts of unused electrode, larger charge, and irreversible capacity than was expected (Fig. 4.10a) and O6 phase formation was slightly delayed (Fig. 4.10b). This is likely due to imperfect cell fabrication. The combination of unexpectedly large charge capacity and smaller discharge capacity suggests the MM2 cell shorted during the fabrication process. Shorting of cells will be discussed later in Chapter 5. Possible shorting of the MM2 cell may impact quantitative analysis, but the qualitative trends hold.

Rietveld refinements were conducted as previously described (Section 2.7.2 and Section 4.2.1). Figure 4.11 shows the XRD patterns as well as the pattern fitting for selected scans seen in Fig. 4.10. The scans shown are scans corresponding to the first scan and 1st bottom of charge (scan 1), a scan showing the unused phase (scan 15), the O6 phase and 1st top of charge (Scan 36), the 2nd bottom of charge (scan 55), and the 2nd top of charge (scan 76).

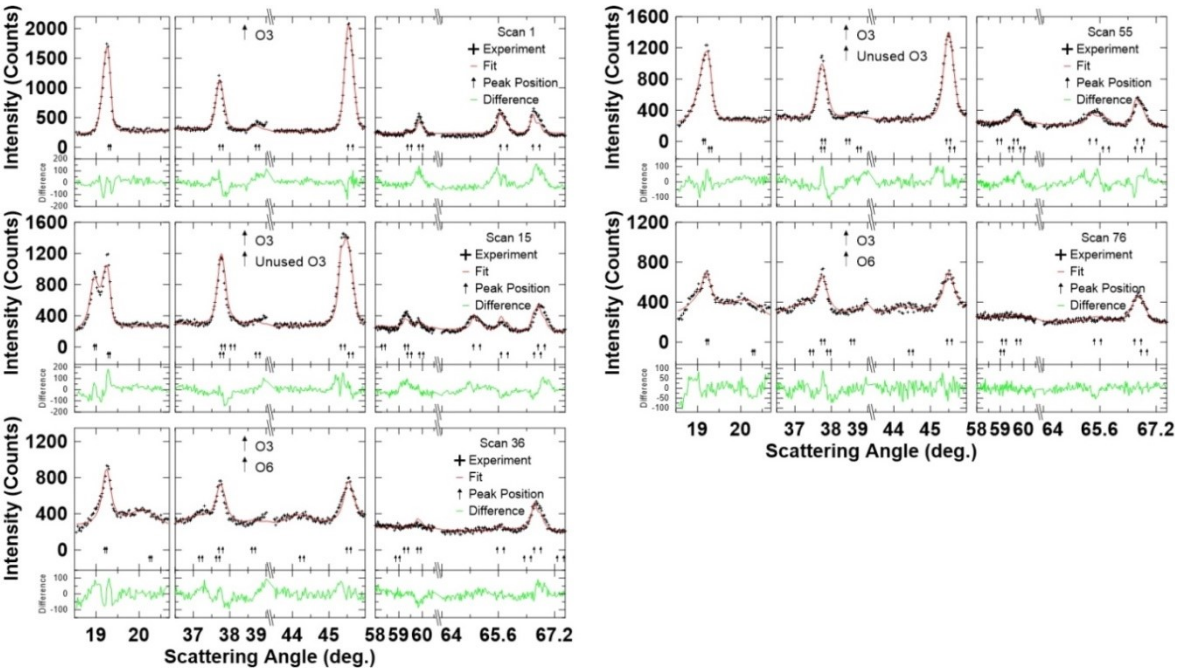

Figure 4.11: In situ XRD Rietveld refinement pattern fitting for MM2. Only select scans and reflections are shown in this figure. The peak positions of the different phases are ordered from top to bottom with the phases indicated in the center panel of each scan.

The unused O3 phase was not refined when only one O3 phase was discernable in the (003) reflection at high voltage due to the instability of refining both the O3 phase and the unused O3 phase together in one peak. It is very likely that both phases contribute to the single O3 (003) reflection peak at high voltage, since some amount of unused O3 (003) reflection can still be seen throughout the experiment (Fig. 4.10). Refinement of the O6 phase in this experiment was more difficult due to broad and indistinct O6 reflections. A table of Rietveld refinement results for MM2 can be found in Appendix B. Table B.2 details the phases present, their scale factors and lattice parameters as well as the Bragg R-factors of each scan shown in Fig. 4.10a.

Figure 4.12 shows Rietveld refinement results for the MM2 in-situ XRD experiment. The top panels show cell voltage vs. time, and the bottom 3 panels show the corresponding phase weight fractions and lattice parameters as a function of scan number. The lattice parameters reported for the O6 phase were converted to the O3 unit cell as described in Section 2.7.2. Similar to MM0, the emergence of the O6 phase coincided with an increase in the *a*-axis and a large decrease in the *c*-axis. The O6 phase was present during the subsequent charge, indicating that this phase transition maintains reversibility. The monoclinic phase was not observed as expected based on the data from Section 3.3.1.

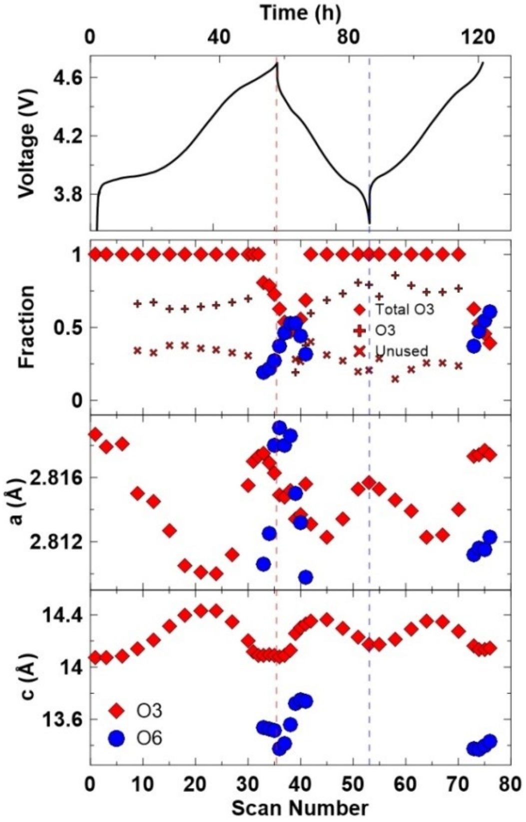

Figure 4.12: Cell voltage, phase weight fractions, *a*-axis, and *c*-axis are shown versus scan number for the MM2 in situ XRD experiment. Results from every 3rd scan are shown except at high voltage (> 4.5 V) where results from every scan are shown. Lattice parameters reported have been converted to the O3 unit cell. The data was collected at room temperature using a specific current of ~5 mA/g (C/50). Error bars were not included in the figure for clarity, but can be found in Table B.2.

The MM2 lattice parameter variation (Fig. 4.12) trended similarly to 0% Mg/Mn (Fig. 4.9) during the 1st charge, but the range of variation decreased afterwards. The reduced lattice parameter variation after the 1st charge will be discussed in more detail later in Section 4.2.4. O6 phase formation occurred at a comparable voltage to MM0, but MM2 did not fully convert to the O6 phase even with the unused electrode phase taken into account. Once again, the 2 phase region of the insulator-metal transition could not be investigated because of the presence of the unused electrode.

One issue seen in Fig. 4.12 is that the phase fractions showed a significant fraction of unused electrode, but the first charge still took ~60 h and the discharge took ~30 h. With around 30% unused electrode (unused phase fractions ranged from 14-40%), the material was expected to take ~20 h to complete the 1st discharge. This is likely due to an overestimation of the unused electrode fraction. It maybe be possible for small portions of unused electrode at the edges of the electrode or closer to the Be window to be overrepresented in the XRD pattern, especially at lower scattering angles. As mentioned in Section 2.7.2, phase fraction analyses in this work were qualitative, not quantitative. Based on a discharge time of ~30 h, it is estimated that the cell contains ~8-10% unused electrode.

However, a cell with 10% unused electrode is expected to take 45 h for its first charge, but this cell took around 60 h. This is likely due to the shorting of the in situ cell during assembly. As will be discussed in Section 5.4, shorted cells were shown to have a larger 1st charge capacity and irreversible capacity. While the relationship between 1st charge capacity, irreversible capacity and duration/extent of cell shorting was not investigated, it may be plausible that more severe instances of cell shorting will lead to larger increases in both the 1st charge capacity and the irreversible capacity. This cell experienced ~50% irreversible capacity, while non-shorted MM2 cells experienced ~35% irreversible capacity (Fig. 3.11). From the large extent of irreversible capacity increase, it is expected that the shorting of this in situ cell contributed to the cell taking 60 h for its first charge.

4.2.3 In Situ XRD Study of 5% Mg/Mn

Figure 4.13 shows the in situ XRD scans of an MM5 cell along with the corresponding voltages at which the scans took place (a) along with an expanded view of the (003) reflection in the high voltage region (b). No shifts associated with the O3-O6-O1 phase transitons were observed in the scans during high voltage.

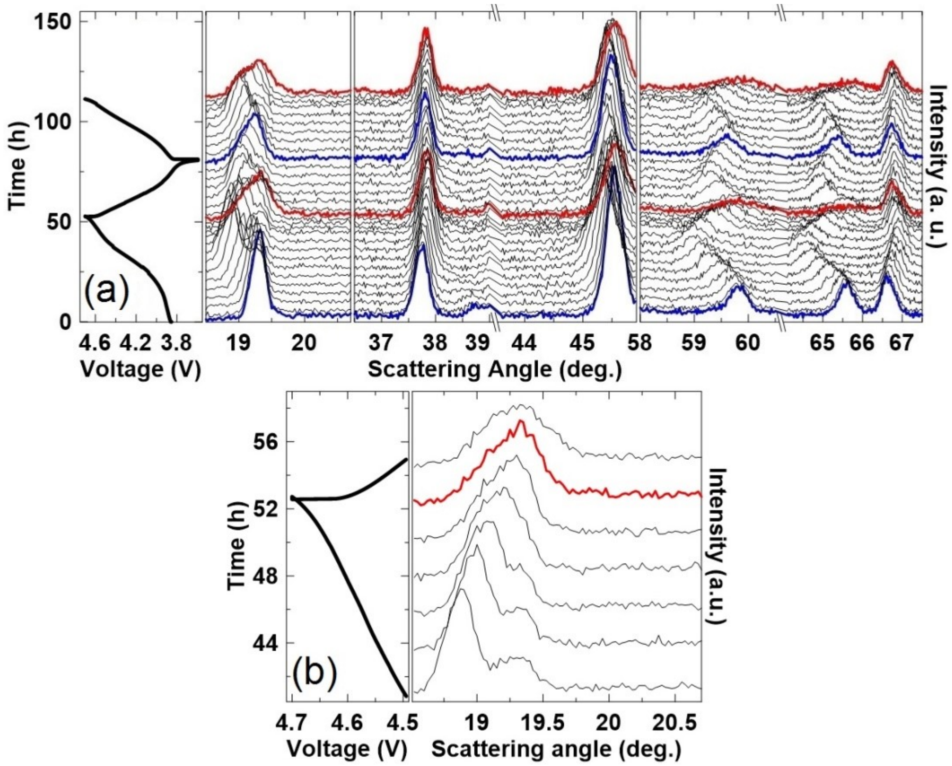

Figure 4.13: Cell voltages and in situ XRD patterns (Cu K_α radiation) of MM5. Panel a shows the full experiment while panel b shows an expanded view of the (003) reflection at high voltage (> 4.5 V) for the first cycle. Every 2nd scan is shown except at high voltage (> 4.5 V) where every scan is shown. The data was collected at room temperature using a specific current of ~5 mA/g (C/50).

Rietveld refinements were conducted as previously described (Section 2.7.2, Section 4.2.1 and Section 4.2.2). Figure 4.14 shows the measured and calculated XRD patterns for selected scans seen in Fig. 4.13. The scans shown are scans corresponding to the first scan and 1st bottom of charge (scan 1), a scan showing the unused phase (scan 14), the 1st top of charge (Scan 25), the 2nd bottom of charge (scan 39), and the 2nd top of charge (scan 52).

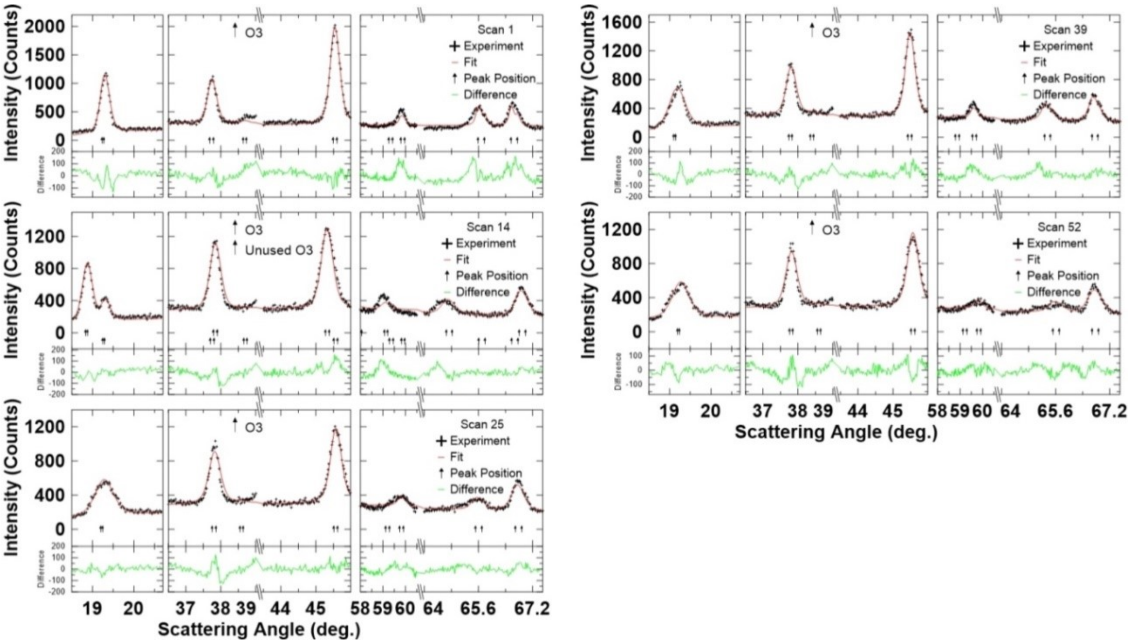

Figure 4.14: In situ XRD Rietveld refinement pattern fitting for MM5. Only select scans and reflections are shown in this figure. The peak positions of the different phases are ordered from top to bottom with the phases indicated in the center panel of each scan.

The unused O3 phase was refined only during the 1st charge when two O3 peaks were observed in the (003) reflection. Even when the unused O3 phase was being refined, the preferred orientation was fixed at 0.2 since peaks were only observed at low angles (compare the right panel of scan 14 of Fig. 4.14 to scan 15 of Fig. 4.11). This suggests only small amounts of unused O3 were present in the MM5 cell, and mainly on the edges of the electrode. In Fig. 4.14, other than scan 14 which contained the O3 and unused O3 phases, scans shown were refined with only the O3 phase. A table of Rietveld refinement results for MM5 can be found in Appendix B. Table B.3 details the phases present, their scale factors and lattice parameters as well as the Bragg R-factors of each scan shown in Fig. 4.13a.

Figure 4.15 shows Rietveld refinement results for 5% Mg/Mn from the in-situ XRD experiment. The top panels show cell voltage as a function of time, and the bottom 3 panels show the corresponding phase weight fractions and lattice parameters as a function of scan number.

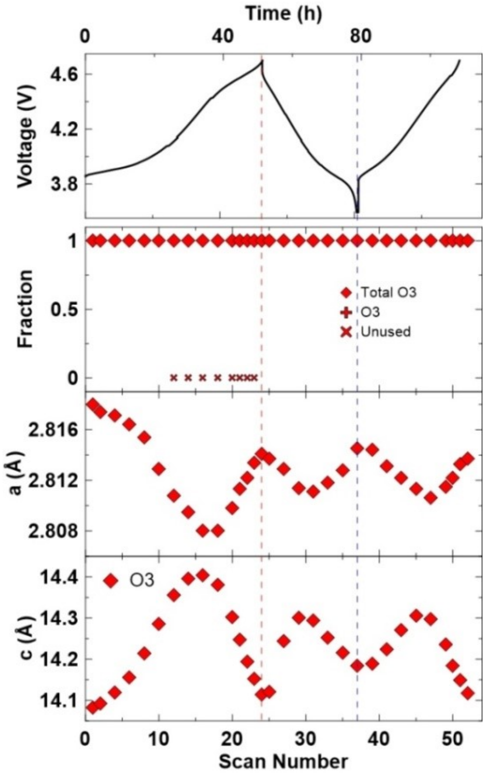

Figure 4.15: Cell voltage, phase weight fractions, *a*-axis, and *c*-axis are shown versus scan number for the MM5 in situ XRD experiment. Results from every 2nd scan are shown except at high voltage (> 4.5 V) where results from every scan are shown. The data was collected at room temperature using a specific current of ~5 mA/g (C/50). Error bars were not included in the figure for clarity, but can be found in Table B.2.

Unlike MM0 and MM2, no other phases were observed at high voltage. However, the increase in the *a*-axis and large decrease in the *c*-axis was still observed as the MM5 cell approached the top of charge.

The lattice parameter variation of 5% Mg/Mn (Fig. 4.15) trended similarly to MM0 and MM2 (Figs. 4.9 and 4.12) during the 1st charge, but the range of variation was suppressed afterwards, similar to the behavior observed with MM2. This suppression of variation range was even more pronounced than MM2, and this will be discussed in the next section. Once again, the region of the insulator-metal transition could not be investigated because of the presence of the unused electrode.

Using the saved refinement input files, Mg occupancy in the lithium layer was investigated. Refinements were conducted using constraints to either stoichiometry (Mg entering the Li layer was offset by Li entering the metal layer to replace the Mg) or a fixed Mg content (Mg entering the Li layer was only offset by reducing the amount of Mg in the metal layer). Neither method gave satisfactory results, likely due to insufficient number of peaks measured in each scan. Figure 4.16 shows the results from refining with a fixed Mg content. The range of Mg occupancy that was physically possible was between an occupancy of 0 and 0.05 for MM5.

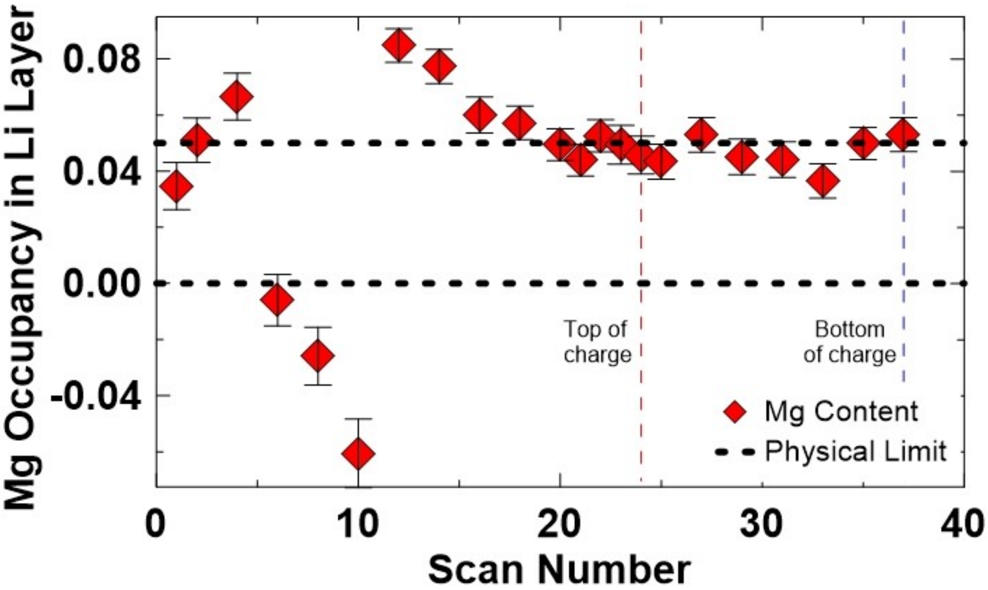

Figure 4.16: Mg occupancy in the Li layer versus scan number for the MM5 in situ XRD experiment. Results from every 2nd scan are shown except at high voltage (> 4.5 V) where results from every scan are shown. The data was collected at room temperature using a specific current of ~5 mA/g (C/50).

As seen in Fig. 4.16, results varied from significant migration and negative migration, including numerous scans with migration amounts that were not physically possible. For the most part, the Mg occupancy hovered around the physical maximum starting near the end of the 1st charge and after. However, owing to the volatility of the results of the first 20 scans, the results from this method were considered inconclusive. The migration of Mg^{+2} ions to the lithium layer would not be surprising due to their similarity in ionic radii ($r_{Li^{+1}}$ = 0.76Å; $r_{Mg^{+2}}$ = 0.72Å)[133] and has been reported before in other materials[55,56] but not in LCO. On the contrary, a few studies have reported no Mg migration in LCO after cycling.[37,85] It is plausible that the migration of Mg into the Li layer during cycling may occur along with the loss of oxygen to restrict Li relithiation and/or suppress the range of lattice parameter variation.

4.2.4 Comparison of the In Situ XRD Studies

Since separate in situ XRD experiments (Sections 4.2.1-3) are hard to compare, this section will compare the three materials and discuss the implications of increasing Mg/Mn doping in LCO. Figure 4.17 shows a compilation of Figs 4.7, 4.10, and 4.13. Arrows were added to the high voltage scans to emphasize the differences in material behavior as the Mg/Mn content progresses from 0% to 2% and 5%.

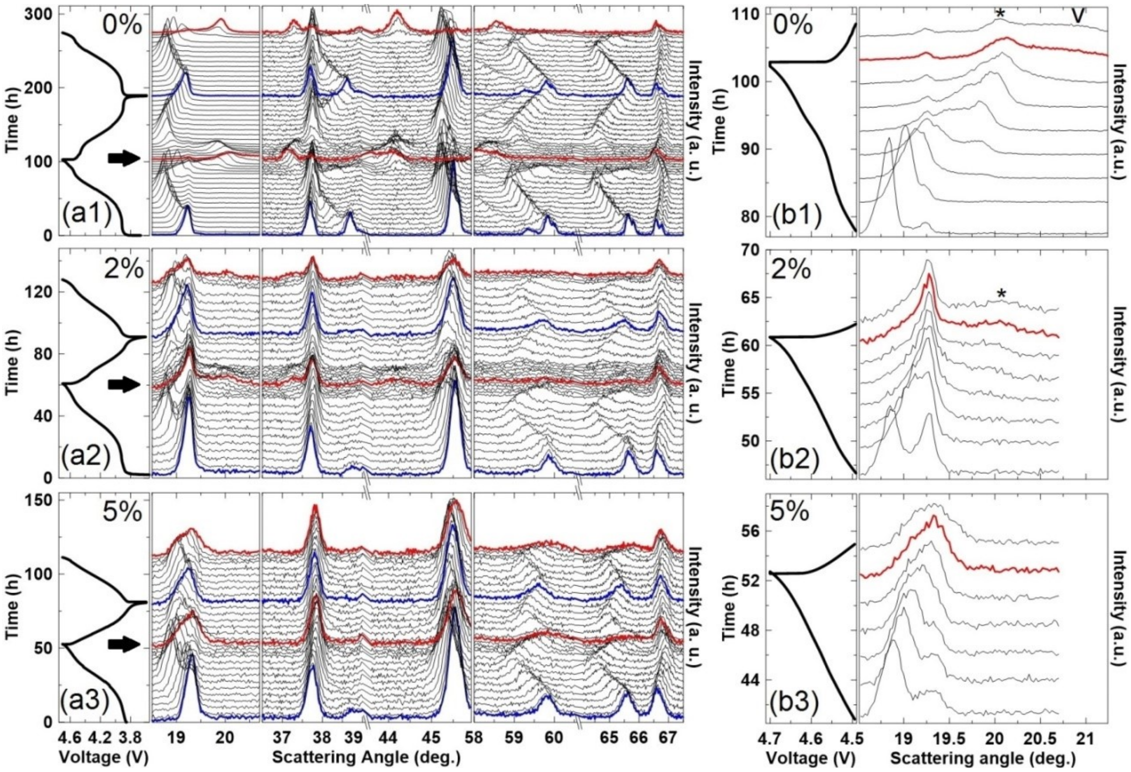

Figure 4.17: Cell voltages and in situ XRD patterns (Cu K_α radiation) of MM0 (1), MM2 (2), and MM5 (3). (a) shows the full experiment while (b) shows an expanded view of the (003) reflection at high voltage (> 4.5 V) for the first cycle. Every 2nd or 3rd scan is shown except at high voltage (> 4.5 V) where every scan is shown. (*) shows the emergence of the O6 phase while (v) shows the emergence of the O1 phase. The data was collected at room temperature using a specific current of ~2.5 mA/g (C/100) for MM0 and ~5 mA/g (C/50) for MM2 and MM5.

The phase transitions that occur at high voltage were very apparent in MM0, while they were muted for MM2 and undetectable for MM5 (Fig. 4.17a). A closer look (Fig. 4.17b) shows a clear O6 phase and emerging O1 phase for 0% Mg/Mn (Fig. 4.17b1), a broad O6 phase and no signs of the O1 phase for 2% Mg/Mn (Fig. 4.17b2), and no O6 or O1 phases for 5% Mg/Mn (Fig. 4.17b3).

Figure 4.18 compares the Rietveld refinement results for the three materials (Figs 4.9, 4.12 and 4.15). Fig. 4.18a shows the comparison of the *a*-axes, while Fig. 4.18b shows the *c*-axes, and Fig. 4.18c shows the cell volumes. The top panels compare the cells as a function of state of charge, while the bottom 3 panels show each individual material as a function of lithium content and differentiated by charge/discharge steps.

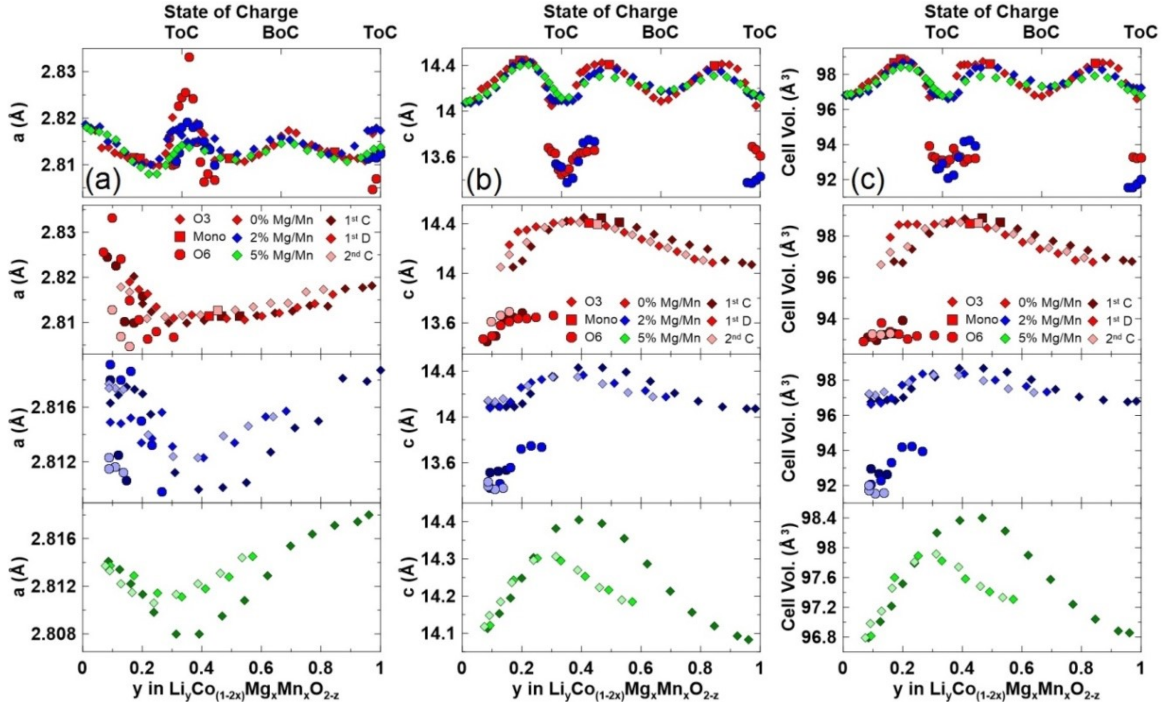

Figure 4.18: Comparison of *a*-axis (a), *c*-axis (b), and unit cell volume (c) of MM0 (red), MM2 (blue), and MM5 (green)) by state of charge (top graph) or y in $Li_yCo_{(1-2x)}Mg_xMn_xO_{2-z}$ (bottom 3 graphs). z = O loss, varies with x after 1st charge.

The effect of Mg/Mn substitution is best illustrated in Fig. 4.18 when comparing 0% Mg/Mn (in red) and 5% Mg/Mn (in green). For 0% Mg/Mn, lattice parameter variation was reversible from the 1st charge (shaded dark) to the 1st discharge (shaded normal) to the 2nd charge (shaded light). The *a* and *c* lattice parameter variations remained consistent for 0% the Mg/Mn sample. For the 5% Mg/Mn cell, however, the 1st charge (dark) behaved differently than the 1st discharge (normal) and 2nd charge (light). The lattice variations do not follow the variations seen in the 1st charge, which suggests a change of structure after the 1st charge. This is an indicator that irreversible changes, presumably the loss of oxygen, occurred during the 1st charge. These irreversible changes also limited the *a* and *c* lattice parameter variation for subsequent cycles, causing less volume change. Volume changes during cycling may infer structural instability, a possible factor in cycling performance as discussed in Section 1.4.1.[28–30,67,68] However, these two variables are determined to be independent with Fig. 3.15 showing that the cycling performance of MM2 was improved even with Fig. 4.18 showing that the recurring O3-O6 phase transitions observed in MM2 continued to induce large volume changes for the material.

Figure 4.19a shows approximate phase diagrams of the three materials as determined by the in situ XRD and electrochemical experiments. Lithium content was determined using coin cell data from the corresponding material. Phase presences were established from the in situ XRD experiments with the exception of the insulator-metal transition, which was determined from coin cell data. Fig. 4.19b shows the effect of Mg/Mn substitution on the O3 lattice parameter variation and on O6 phase formation. O3 volume changes remained consistent during charge/discharge for 0% Mg/Mn, but were suppressed after the first charge for 2% and 5% Mg/Mn. O6 phase formation was also suppressed as Mg/Mn doping increased, with partial O6 formation for 2% Mg/Mn, and no O6 formation for 5% Mg/Mn.

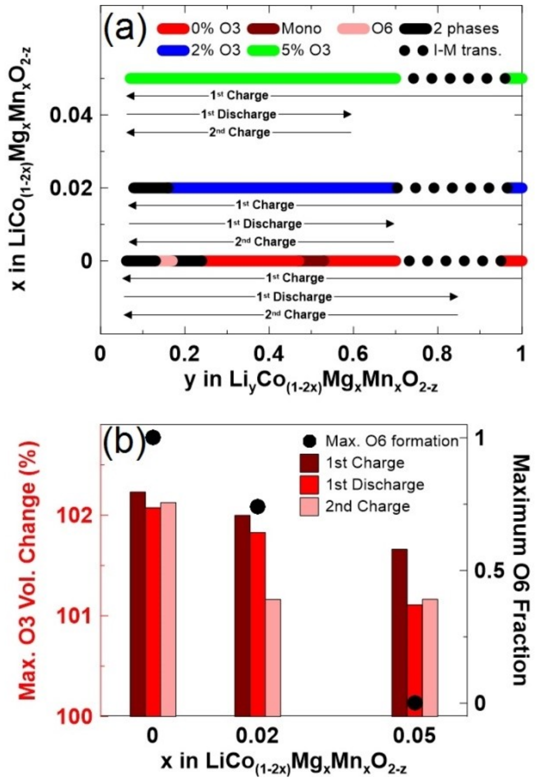

Figure 4.19: (a) shows the phases present as a function of y in $Li_yCo_{(1-2x)}Mg_xMn_xO_{2-z}$ as well as the span of y for each charge/discharge step. (b) shows maximum O6 weight fraction and maximum O3 volume change as a function of x in $LiCo_{1-2x}Mg_xMn_xO_{2-z}$. z = oxygen loss, varies with x after 1st charge.

Fig. 4.19 shows that as the Mg/Mn content increased, fewer and fewer distinct phases formed, from the disappearance of the monoclinic and O1 phases at 2% Mg/Mn to the disappearance of all but the O3 phase at 5% Mg/Mn. MM0 underwent the insulator-metal transition from a Li content of 0.95 to 0.70, then the order-disorder transition occurred between Li contents of 0.53-0.47. The O6 phase started to appear at 0.24 Li before O3 completely disappeared at 0.17 Li. Only O6 was present from then until a Li content of 0.13, which indicates that the O6 phase stability is centered at about 0.15 Li. After 0.13 Li, the O1 phase emerged and the electrode remained two-phase until it finished its charge at a Li content of 0.06. The 2% Mg/Mn sample experienced the insulator-metal transition between about 0.96-0.70 Li, and stayed as the O3 phase until a Li content of 0.16, at which point the O6 phase emerged. The sample remained two-phase until the end of charge at 0.08 Li. MM5 underwent the insulator-metal transition from 0.96 Li to 0.70 Li, after which it continued to stay as O3 until the end of charge at a Li content of 0.07.

From the in situ XRD studies, it is clear that the incorporation of Mg and Mn into the material suppressed the O3-O6-O1 phase transitions. However, the cell with 2% Mg/Mn was confirmed to still show the O3-O6 phase transition, as was suggested by dq/dV results (Figs. 3.12 and 3.14), meaning that the improved (but still poor) cycling performance from Mg/Mn substitution did not stem from the suppression of phase transitions or from increased structural stability. The suppression of phase transitions likely stemmed from the oxygen loss as discussed in Section 3.3.2, which might lock the material in the O3 phase and prevent the facile shifting of the CoO_2 slabs to form firstly O1, then O6 as the Mg/Mn content increased. Another consequence of increasing Mg/Mn content in LCO was the irreversible structure change caused by the first charge which restricted unit cell shifts upon subsequent lithiation or delithiation (Fig. 4.18). It is uncertain whether the irreversible structure change stemmed from just oxygen loss or if other processes, such as Mg migration into the lithium layer (pillar effect),[56,91] also contributed.

Chapter 5 – Miscellaneous Investigations of Mg/Mn Doped LCO

There were opportunities to carry out studies which were not directly related to the scope of this thesis, and these miscellaneous investigations will be discussed in this chapter. This chapter will explore various synthesis procedures (Section 5.1), the effect of precursor oxidation on electrochemical performance (Section 5.2), the role of Li content in LCO with 5% Mg/Mn (Section 5.3), and the effects of cell shorting during fabrication (Section 5.4).

5.1 Evaluation of Synthesis Procedures

Initially, it was thought that the Mg/Mn doped LCO materials could be synthesized simply via a solid state route. However, this project has undergone several iterations of the synthesis procedure in the progression up to the final method as detailed in Section 2.1. This section will first discuss solid state synthesis (Section 5.1.1) before examining co-precipitation in air (Section 5.1.2). A trial run using a continuously stirred tank reactor will also be examined (Section 5.1.3).

5.1.1 Solid State Synthesis

While there are numerous techniques to synthesize LCO, the simplest method is the solid state synthesis,[23,24,27,29,37,40,41] which consists of mixing appropriate ratios of Li and Co containing powders before heating at a high temperature. Due to its simplicity, solid state synthesis using carbonate salts of Li, Co, Mg, and Mn was carried out. Appropriate ratios of each carbonate salt was mixed, ground together, and heated as described in Section 2.1.2. Figure 5.1 shows the XRD patterns (collected as described in

Section 2.3.1) of LCO with 0-5% Mg/Mn except 4% Mg/Mn, which was not measured due to issues discussed later. An expanded view of the region around 43° is included. Reflections, as indexed in the R$\bar{3}$m space group, are labeled in the figure as well.

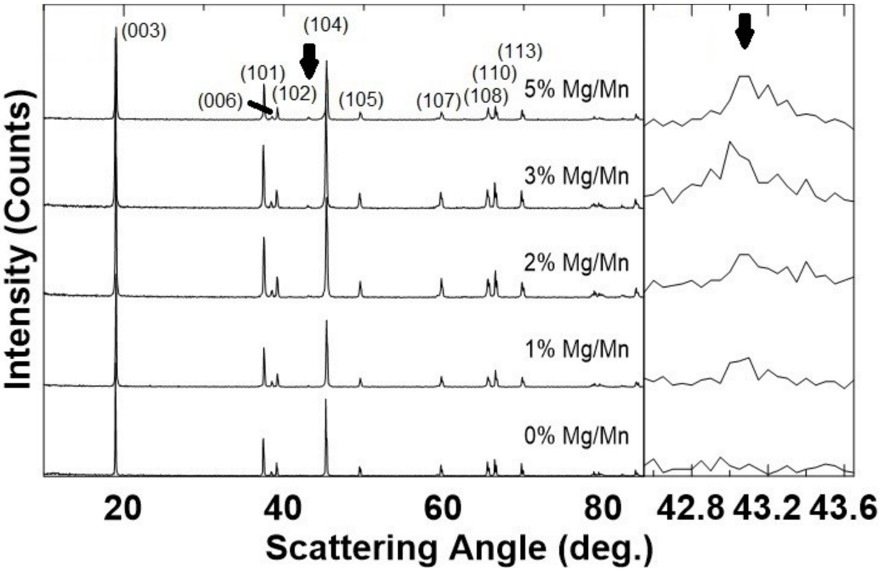

Figure 5.1: XRD patterns (Cu Kα radiation) of solid state synthesized samples collected from 10°–85°, along with reflections indexed in the R$\bar{3}$m space group and an expanded view of the 43° region. (↓) shows the emergence of the MgO phase.

As Mg/Mn content increased, a new phase, determined to be MgO (JCPDS card, No. 00-078-0430),[121] was observed and is denoted by the (↓) symbol in Fig. 5.1. This indicates that Mg was not fully integrating into the LCO material. This would be problematic for examining the effects of Mg/Mn doping in LCO. To study if it was possible to improve Mg integration into LCO, the 3% Mg/Mn material was crushed and ground using a mortar and pestle before being reheated in the same manner as described in Section 2.1.2. The MgO XRD peak at 43° decreased after the first round of crushing and grinding. The same sample was then subjected to a total of 3 rounds of grinding then heating. The time and force of each round of grinding was not controlled, but each round consisted of around 20-30 minutes of grinding under a significant portion of body weight. Figure 5.2 shows the 43° region of the XRD patterns of 3% Mg/Mn after 0-3 rounds of grinding and heating (a) and the peak height of each pattern at 43° (b).

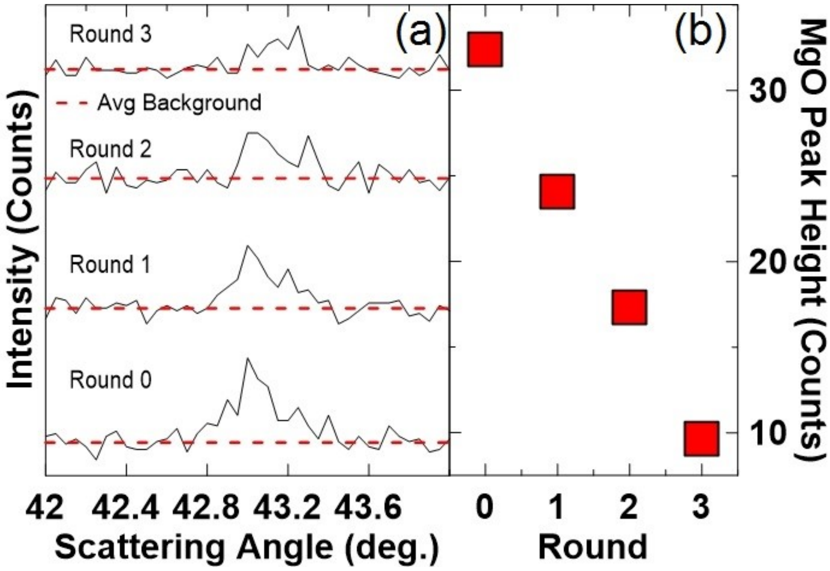

Figure 5.2: XRD patterns (Cu Kα radiation) of 3% Mg/Mn samples after 0-3 rounds of grinding and heating. Patterns were collected from 10°–85°, but only the 43° region (a) is shown. The peak height at 43° (b) is also shown.

Fig. 5.2 indicates that the MgO peak at 43° decreased after each round of grinding and heating. Sample loss was minimal (less than 1.5% by weight per round), so the reduction of MgO likely suggests the reintegration of Mg into the LCO material. Further studies were not conducted as this procedure was deemed too costly in time (each round includes overnight heating at 900°C) and synthesis by co-precipitation was explored (Section 5.1.2). Many questions remain unanswered, such as the Li content after rounds of heating, the Mg/Mn distribution in the material, and the optimal synthesis conditions.

5.1.2 Co-precipitation in Air

After determining that solid state synthesis (Section 5.1.1) was too time-intensive, synthesis via co-precipitation was explored. The setup was identical to that described in Section 2.1.1, with the only difference being the reaction occurred without being under a N_2 atmosphere. Figure 5.3 shows a photo of the set of precursor materials co-precipitated in air (top) and under N_2 atmosphere (bottom). As seen in the image, the two sets of precursor materials were visually different. Precursors co-precipitated in air were all black, while precursors co-precipitated under N_2 atmosphere were various shades of pink.

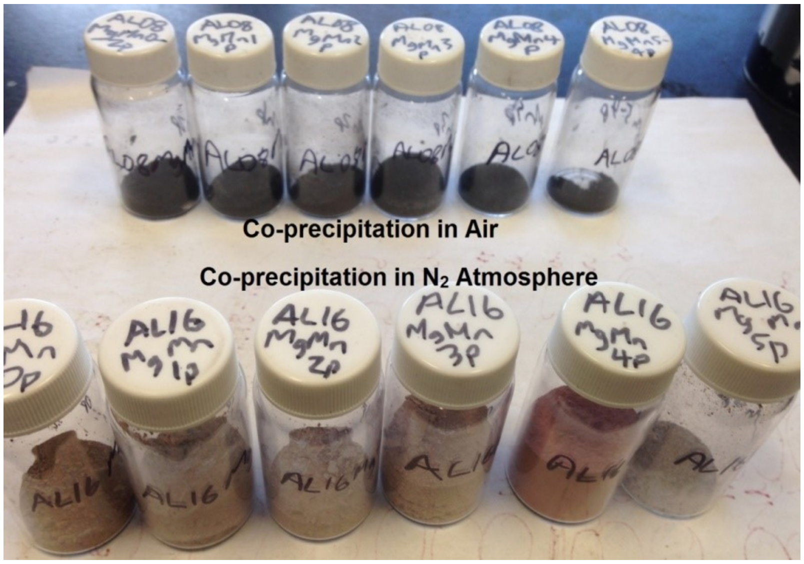

Figure 5.3: Precursor materials synthesized by co-precipitation. The precursors in the top row were co-precipitated in air, and the precursors in the bottom row were co-precipitated under N_2 atmosphere.

XRD patterns were collected (as described in Section 2.3.1) to investigate if the differing appearances stemmed from differing structures or phases. Figure 5.4 shows the XRD patterns of the precursors co-precipitated in air. Also shown in Fig. 5.4 are the peak positions of $Co(OH)_2$ and two species associated with the oxidation of the cobalt hydroxide, Co(OOH), and Co_3O_4 (JCPDS cards, No. 00-074-1057, No. 00-073-1213, and No. 00-074-2120, respectively).[121]

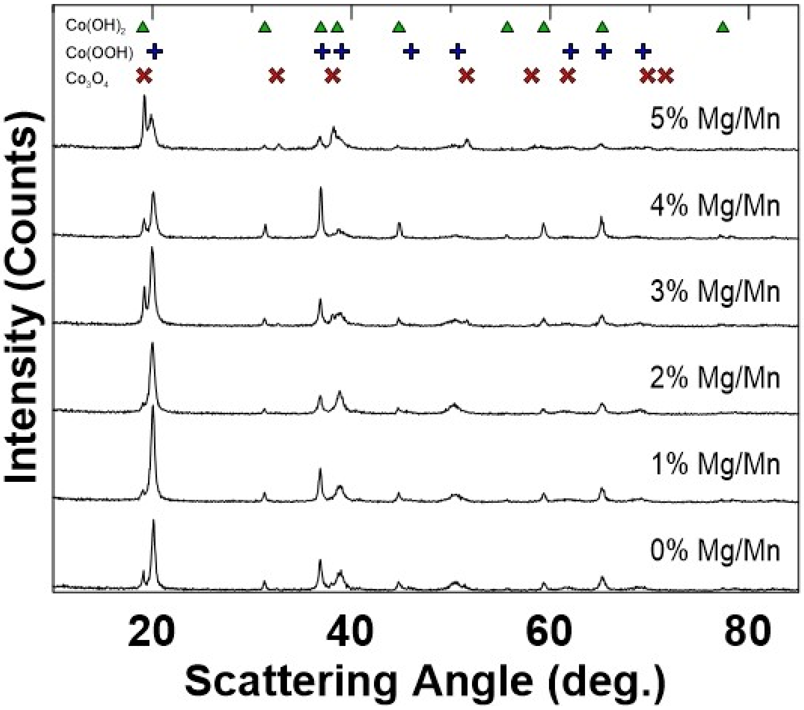

Figure 5.4: XRD patterns (Cu Kα radiation) of 0-5% Mg/Mn precursors co-precipitated in air collected from 10°–85°. Peak positions of $Co(OH)_2$, Co(OOH), and Co_3O_4 (JCPDS cards, No. 00-074-1057, No. 00-073-1213, and No. 00-074-2120, respectively) are shown above the patterns.[121]

Fig. 5.4 clearly demonstrates that the precursor samples underwent oxidation during the co-precipitation process. Presence of all three ($Co(OH)_2$, Co(OOH), and Co_3O_4) phases were observed in varying amounts. While Rietveld refinements on these XRD patterns were not performed, refinements would allow for the quantification of each phase.[125,142,143] XRD patterns collected and Rietveld refinement of precursors co-precipitated under N_2 atmosphere were discussed in Section 3.1.2, and it was shown that those precursors contain only the $Co(OH)_2$ phase with no signs of the oxidized species.

The set of precursors co-precipitated in air were lithiated as detailed in Section 2.l.2 and characterized. Figure 5.5 shows the XRD patterns (Section 2.3.1) of the lithiated samples collected in panel a while panels b, c, and d show lattice constants and unit cell volume vs. expected Mg/Mn content. Reflections, as indexed in the $R\overline{3}m$ space group, are labeled in the Fig 5.5a. Lattice constants were obtained from Rietveld refinement (Section 2.3.2) and cell volumes was calculated from the lattice constants. Rietveld refinement results of samples lithiated from precursors co-precipitated under N_2 atmosphere (Tab. 3.6 and Fig. 3.9) are included in Fig. 5.5b-d for comparison.

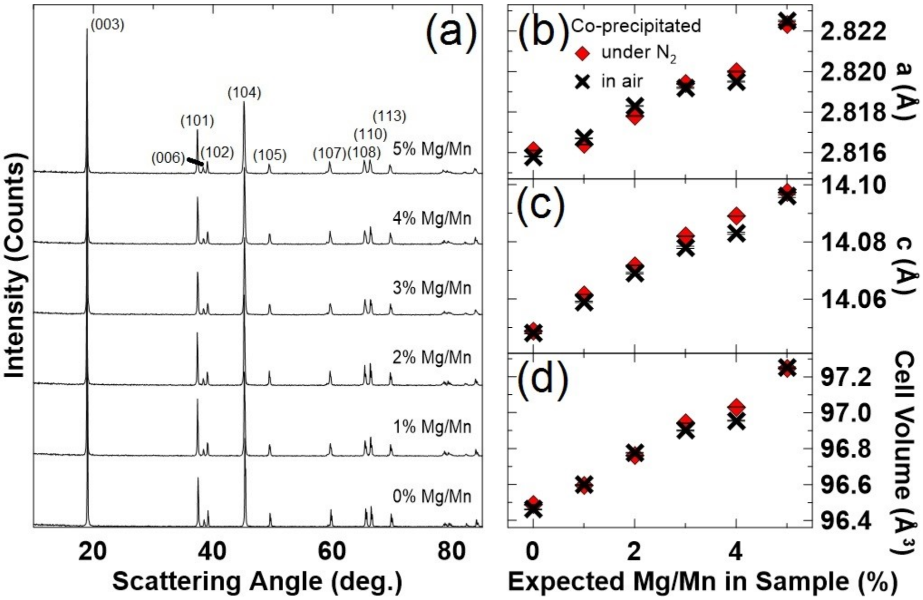

Figure 5.5: XRD patterns (Cu Kα radiation) of 0-5% Mg/Mn LCO samples prepared from precursors co-precipitated in air (a). Also shown are lattice constants (panels b and c) and unit cell volume (d) obtained from Rietveld refinements of XRD patterns of samples prepared from both precursors co-precipitated in air and under N_2 atmosphere.

Interestingly, Fig. 5.5 suggests that 0-5% Mg/Mn LCO samples prepared from precursors co-precipitated in air were comparable to samples prepared from precursors co-precipitated under N_2 atmosphere. XRD patterns (Fig. 5.5a) showed only a single phase, suggesting that the presence of oxidation in precursors (Fig. 5.4) did not introduce new, unwanted compounds. SEM (Section 2.4) and ICP-OES (Section 2.2) characterization was also carried out. Figure 5.6 shows the SEM images of the precursors co-precipitated in air (a) and the lithiated samples (b), as well as the metal ratios of the precursor and lithiated samples as determined by ICP-OES (c).

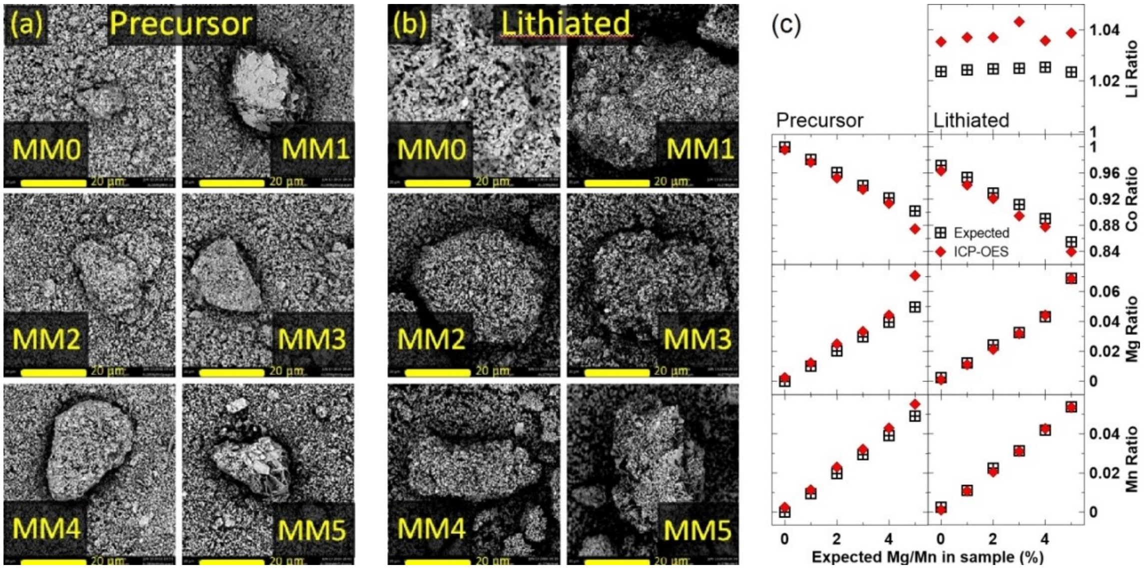

Figure 5.6: SEM images of precursors co-precipitated in air (a) and the lithiated samples (b) magnified at 5000x. Panel c shows metal atomic ratios as determined by ICP-OES for precursor and lithiated materials. Ratios were normalized to 1 for precursor materials and 2 for lithiated samples.

SEM images (Fig 5.6a and b) show both precursors co-precipitated in air and their lithiated samples consisted of mostly small particles, similar to their counterparts co-precipitated under N_2 (Figs 3.5 and 3.10). Metal atomic ratios as determined from ICP-OES results for the precursors co-precipitated in air were close to the expected ratios. The Mg ratio for 5% Mg/Mn was higher than expected, but all other results suggest this can be attributed to experimental error. Metal ratios for lithiated samples were also close to the expected ratios. However, Li ratios were higher than expected, which differed from results for co-precipitation under N_2 (Fig. 3.6) which had lower Li contents than calculated.

The increased Li content likely stemmed from precursor oxidation, but it is uncertain why samples had more Li than expected. $Co(OH)_2$ contains 63.4% Co by weight while Co(OOH) contains 64.1% Co and Co_3O_4 contains 73.4% Co, so samples lithiated from oxidized precursors should contain less Li than calculated, which was not the case. Another considered possibility was that one of the oxidized phases was incompatible in forming LCO. Both $Co(OH)_2$ and Co(OOH) have a layered structure while Co_3O_4 has a spinel structure,[125,143] so Co_3O_4 was scrutinized further. While not quantified, Co_3O_4 seemed to be present in low amounts, with 3% Mg/Mn and 5% Mg/Mn showing a more distinct Co_3O_4 peak than the other samples (Fig. 5.4), which might explain the Li content trend seen in Fig. 5.6c. However, since Co_3O_4 is a common precursor for solid state synthesis of LCO,[24,27,29,37,40,41] it is uncertain why it would be incompatible in forming LCO, and thus casts doubt on this hypothesis.

Co-precipitation synthesis in air forms precursor materials that were in various states of oxidation (Fig. 5.4), but LCO samples prepared from these precursors (Figs. 5.5

and 5.6) did not seem to differ much from LCO samples prepared from precursors co-precipitated under N_2 atmosphere (Section 3.2). The electrochemical performance of LCO materials prepared from precursors co-precipitated in air will be discussed later in Section 5.2. Syntheses were adjusted so the co-precipitation occurred under N_2 atmosphere (Section 2.1.1) to avoid the uncertainty of having precursors with an unknown distribution of oxidized precursors, and those results were discussed in Ch. 3 and 4.

5.1.3 Synthesis Using a Continuously Stirred Tank Reactor (CSTR)

While the majority of this thesis focused on 0-5% Mg/Mn LCO samples synthesized as described in Section 2.1, a trial run with the continuously stirred tank reactor (CSTR) was carried out to investigate synthesis in a more controlled manner. The setup and procedure was described in Section 2.1.3. Only one 5% Mg/Mn batch was run due to the large amount of samples synthesized. Precursors were lithiated as described in Section 2.1.2. Both precursors and lithiated samples were characterized by SEM and XRD as described in Sections 2.4 and 2.3, respectively. Figure 5.7 shows the SEM images of both precursor and lithiated samples. The SEM images show that particles produced from the CSTR (Section 2.1.3, Fig. 5.7)) differed noticeably from particles produced as described in Section 2.1.1 (Figs. 3.5 and 3.10), with the exception of 4% Mg/Mn. These images showed that the material consisted of larger particles than seen in Figs. 3.5 and 3.10 with more uniform particle sizes. CSTR precursors did not aggregate to form clusters upon lithiation, unlike as observed in Fig. 3.10.

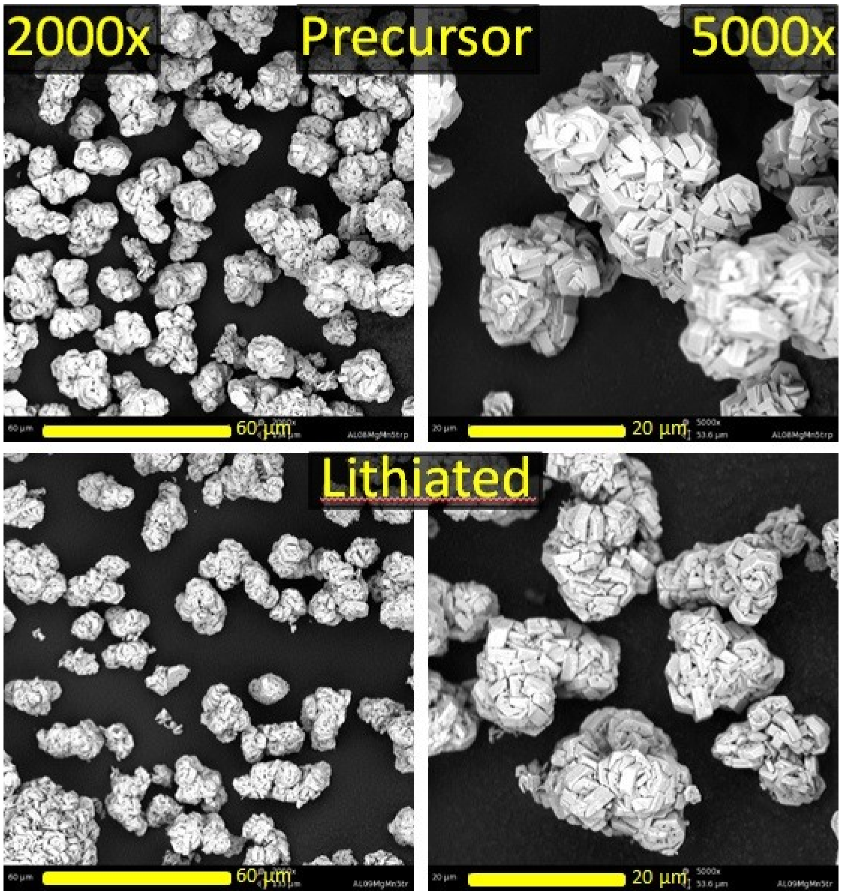

Figure 5.7: SEM images of CSTR precursors (top) and the lithiated samples (bottom) magnified at 2000x (left) and 5000x (right).

Figure 5.8 shows the XRD patterns (collected as described in Section 2.3.1) of the CSTR precursor and lithiated 5% Mg/Mn samples. Also shown are the counterparts co-precipitated under N_2. Reflections are indexed in the $P\overline{3}m1$ space group for precursor materials and the $R\overline{3}m$ space group for lithiated materials. The comparison of the two precursor and lithiated samples show no significant differences.

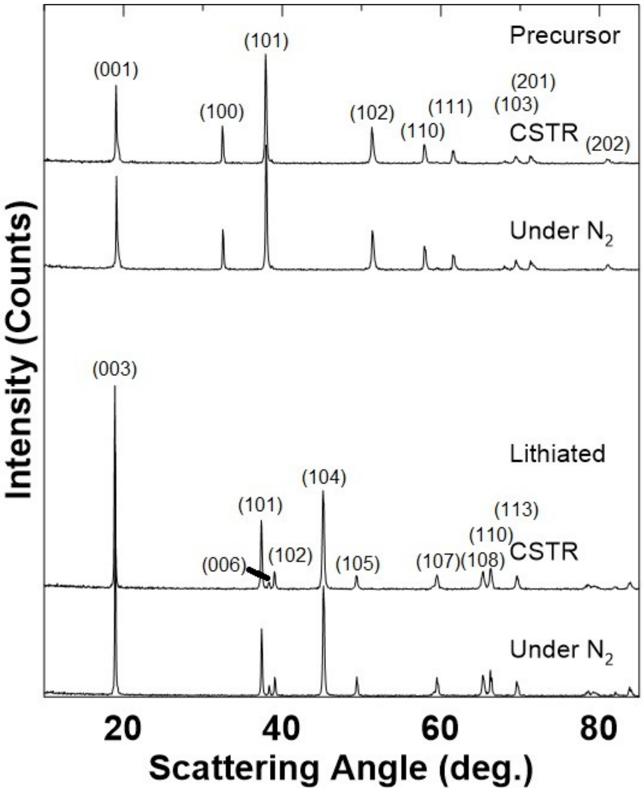

Figure 5.8: A comparison of XRD patterns (Cu Kα radiation) of CSTR precursor and lithiated samples and precursor and lithiated samples co-precipitated under N_2 atmosphere, collected from 10°–85°, along with reflections indexed in the $P\overline{3}m1$ (precursor) or $R\overline{3}m$ (lithiated) space groups.

As noted in Chapter 3 and observed here with CSTR synthesis, the synthesis of particles with uniform particle sizes (Fig. 5.7) is possible under certain, undetermined reaction conditions. Although not investigated in this thesis, synthesis with the CSTR will allow for control of many different variables, enabling the optimization of reaction conditions. However, each CSTR synthesis batch produces an amount of sample that exceed the amount needed for material characterization and coin cell study (such as those discussed in Ch. 3), so only one trial run was carried out. The excess produced from this batch was then used to study the effect of Li content, and that study will be discussed in Section 5.3.

5.2 The Effect of Oxidized Precursor Materials on Electrochemical Performance

As Section 5.1.2 showed, Mg/Mn doped LCO prepared from oxidized precursors seemed to be similar to Mg/Mn doped LCO prepared from $M(OH)_2$ (M = Co, Mg, Mn) precursors. While precursors co-precipitated in air (Fig. 5.4) were undoubtedly different from precursors co-precipitated under N_2 (Fig. 3.2), both lithiated samples seemed similar when examining XRD analyses (Fig. 3.7 and Fig. 5.5) and SEM images (Fig. 3.10 and Fig. 5.6b). One difference observed during characterization was the metal atomic ratios as determined by ICP-OES, where Mg/Mn doped LCO prepared from $M(OH)_2$ (M = Co, Mg, Mn) precursors had a lower Li ratio than expected based on calculations (Fig. 3.6) and samples prepared from oxidized precursors had a higher Li ratio than expected (Fig. 5.6c).

Mg/Mn doped LCO cells were fabricated (Section 2.5) and cycled (Section 2.6) to determine if differences could be detected in the electrochemical performance of the materials. Figure 5.9 shows first cycle cell voltage as a function of capacity and dq/dV as a function of voltage. Unlike their counterparts that were prepared from precursors co-precipitated under N_2 (Section 3.3), sets of cells were not consistent enough to show only data from only one cell and so Fig. 5.9 shows separate panels for each set of Mg/Mn content.

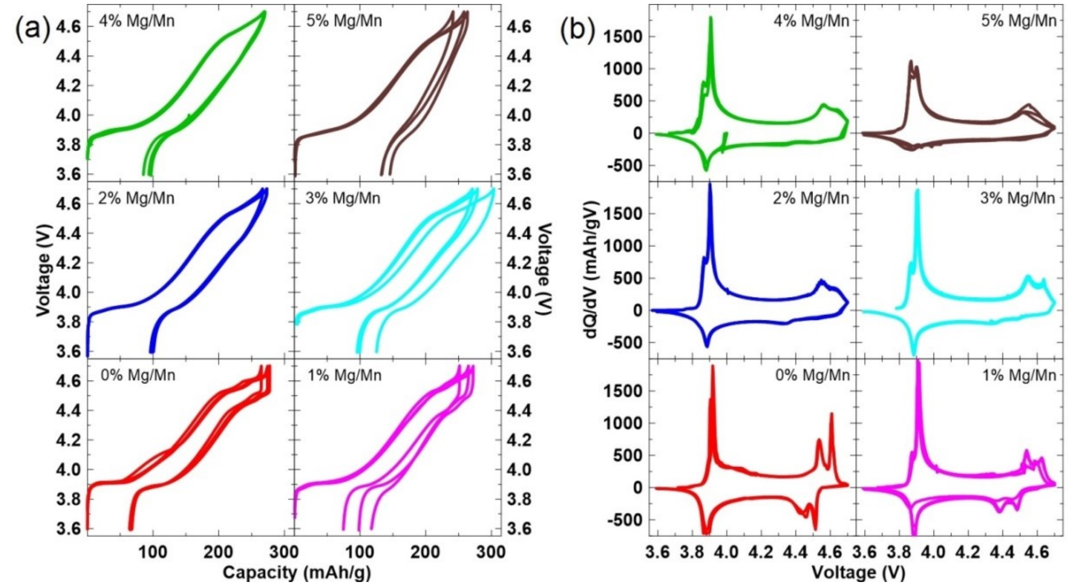

Figure 5.9: First cycle (a) cell voltage as a function of capacity and (b) differential capacity (dq/dV) as a function of voltage for MM0-MM5 cells prepared from precursors co-precipitated in air. Cells were cycled between 3.6 V and 4.7 V at 30°C using a specific current of ~5 mA/g (C/50).

For the most part, cells retained similar features and trends discussed in Fig. 3.12. Like cells prepared from $M(OH)_2$ (M = Co, Mg, Mn) precursors, trends such as the broadening of the dq/dV peak of the insulator-metal transition and the shifting of the 2 high voltage dq/dV peaks to one broad peak were observed. However, the order-disorder transition at 0.5 Li was already scarcely observable for the MM0 cells prepared from oxidized precursors. This suggests that the preparation of LCO from oxidized precursors will synthesize a material containing some degree of structural defects.[144]

As mentioned, sets of cells were less consistent when the materials were prepared from precursors co-precipitated in air. With the exception of MM2 and perhaps MM4, cells were distinctly different in Fig. 5.9a. First charge capacities also seemed larger than observed in Fig. 3.11, so first cycle data for the two sets of samples were compiled.

Figure 5.10 shows the comparison of first cycle data of cells prepared from precursors co-precipitated either under N_2 or in air. On the whole, cells prepared from precursors co-precipitated in air had larger first cycle charge capacities (Fig. 5.10a). The cells did not display the stepwise discharge and irreversible capacity trends observed for cells prepared from $M(OH)_2$ (M = Co, Mg, Mn) precursors (Fig. 5.10b and c).

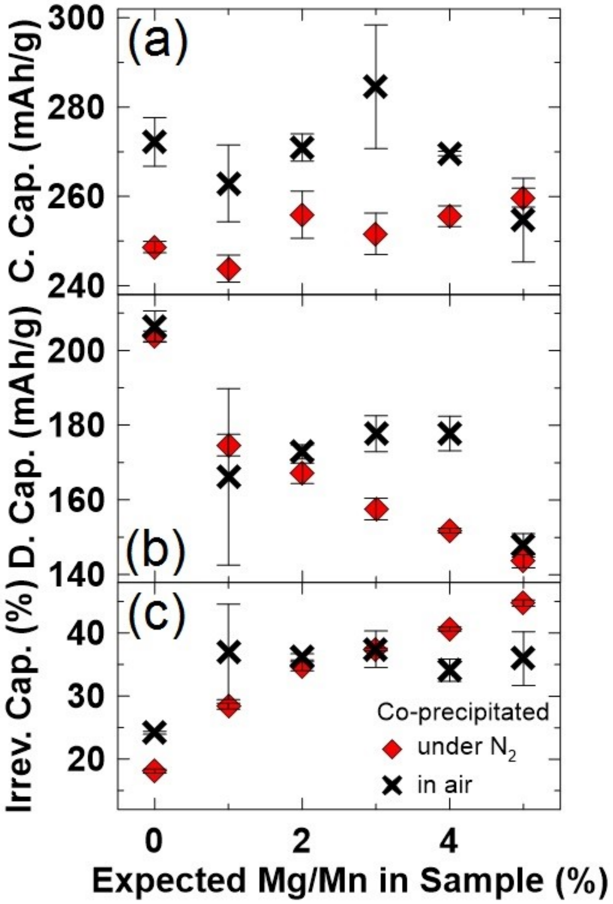

Figure 5.10: First cycle (a) charge capacity, (b) discharge capacity, and (c) irreversible capacity for MM0-MM5 cells prepared from precursors co-precipitated either under N_2 or in air. Cells were cycled between 3.6 V and 4.7 V at 30°C using a specific current of ~5 mA/g (C/50).

The higher first cycle charge capacities (Fig. 5.10a) observed may be connected to the higher Li ratio as seen in Fig. 5.6c. As discussed in Section 3.3.2, if cells underwent full delithiation, it would explain the charge capacity trend observed in Fig. 3.11b. Extending that consideration to this case, delithiation of 1.04 Li would increase the capacity by around 11 mAh/g, which is still less than the increase in first charge capacity observed when comparing to cells with precursors co-precipitated under N_2 (Fig. 5.10a). It is also uncertain why a trend of increasing first cycle discharge capacity is observed from 1%-4% Mg/Mn.

While there are still many unanswered questions as to exactly how preparing samples from oxidized precursors affected electrochemical performance, this study seemed to suggest that an increase in variation of the material may be an issue. Since there were an unknown magnitude and distribution of the oxidized phases in the precursor, the homogeneity of the material and consistency of electrodes prepared from the material were questionable.

5.3 Varying Li Content in LCO with 5% Mg/Mn

The trial CSTR synthesis batch (Section 5.1.3) produced an amount of material that exceeds the amount needed for characterization and basic electrochemical characterization. With excess precursor materials available, this section characterizes and evaluates 5% Mg/Mn lithiated with a varying amount of Li. Table 5.1 lists the lithiated materials prepared by their target Li ratio, their sample designations and their expected compositions based on masses used in the lithiation process. Li contents were chosen based on the amount in excess of an equivalent Li and M ratio (M = Co, Mg, Mn) and expected compositions were calculated assuming Li + M = 2.

Table 5.1: List of 5% Mg/Mn samples synthesized with varying Li content. M = Co, Mg, Mn.

Target Li Ratio	**Designation**	**Expected Compositions**
$Li_{1.01} : M_1$	Li1	$Li_{1.006}Co_{0.896}Mg_{0.049}Mn_{0.049}O_2$
$Li_{1.03} : M_1$	Li3	$Li_{1.015}Co_{0.887}Mg_{0.049}Mn_{0.048}O_2$
$Li_{1.05} : M_1$	Li5	$Li_{1.025}Co_{0.879}Mg_{0.048}Mn_{0.048}O_2$
$Li_{1.07} : M_1$	Li7	$Li_{1.034}Co_{0.870}Mg_{0.048}Mn_{0.047}O_2$
$Li_{1.10} : M_1$	Li10	$Li_{1.048}Co_{0.858}Mg_{0.047}Mn_{0.047}O_2$
$Li_{1.15} : M_1$	Li15	$Li_{1.069}Co_{0.839}Mg_{0.046}Mn_{0.046}O_2$
$Li_{1.20} : M_1$	Li20	$Li_{1.090}Co_{0.820}Mg_{0.045}Mn_{0.045}O_2$
$Li_{1.25} : M_1$	Li25	$Li_{1.110}Co_{0.802}Mg_{0.044}Mn_{0.044}O_2$

ICP-OES (Section 2.2) was used to determine the cation concentrations of the lithiated samples and converted to a normalized ratio of 2, assuming the formula unit $Li_yM_xO_2$ ($x + y = 2$; M = Co, Mg, Mn). Figure 5.11 shows the expected cation ratios and the ratios as determined by ICP-OES. As observed before, lower Li ratios than expected was due to lithium loss during the heating step, which is known to occur but not accounted for in the calculation of the expected ratio.

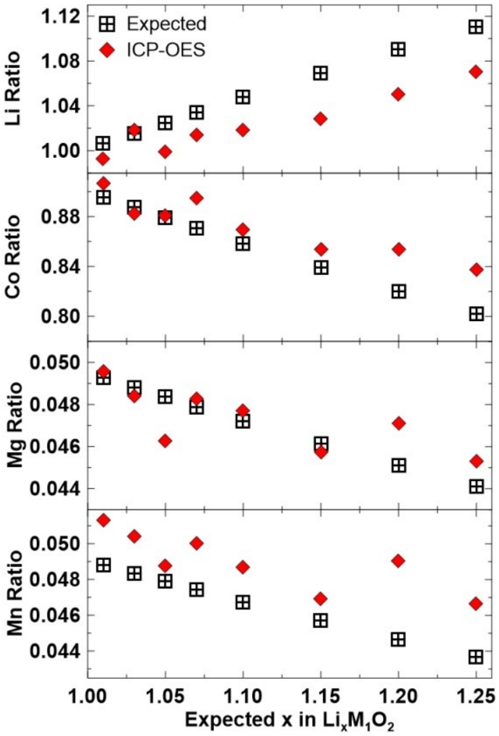

Figure 5.11: Metal atomic ratios as determined by ICP-OES for CSTR samples lithiated with varying amounts of Li. Ratios were normalized to 2.

Since all these materials were prepared from the same precursor sample, it was expected that the ratios of Co, Mg, and Mn would be consistent for all the samples. Indeed, a quick calculation of the 8 samples showed standard deviations that were 0.14% of the average ratio for Co, 1.37% for Mg, and 1.30% for Mn, which fell within the 2% uncertainty of the method.

XRD patterns of the lithiated samples were collected (Section 2.3.1) and Rietveld refinements of the XRD patterns were performed (Section 2.3.2). Figure 5.12 shows the XRD patterns of the samples (a) as well as Li content (b), lattice constants (c and d), and unit cell volume (e) as determined from Rietveld refinements. Reflections, as indexed in the $R\bar{3}m$ space group, are labeled in Fig. 5.12 as well. All the XRD patterns showed only a single phase, although it is acknowledged that a small amount of a lithium-rich phase may not be easily visible with the XRD pattern collection protocol used in these scans, which only scanned for 3 s per step. An inspection for lithium carbonate reflection peaks did not find any discernable peaks.

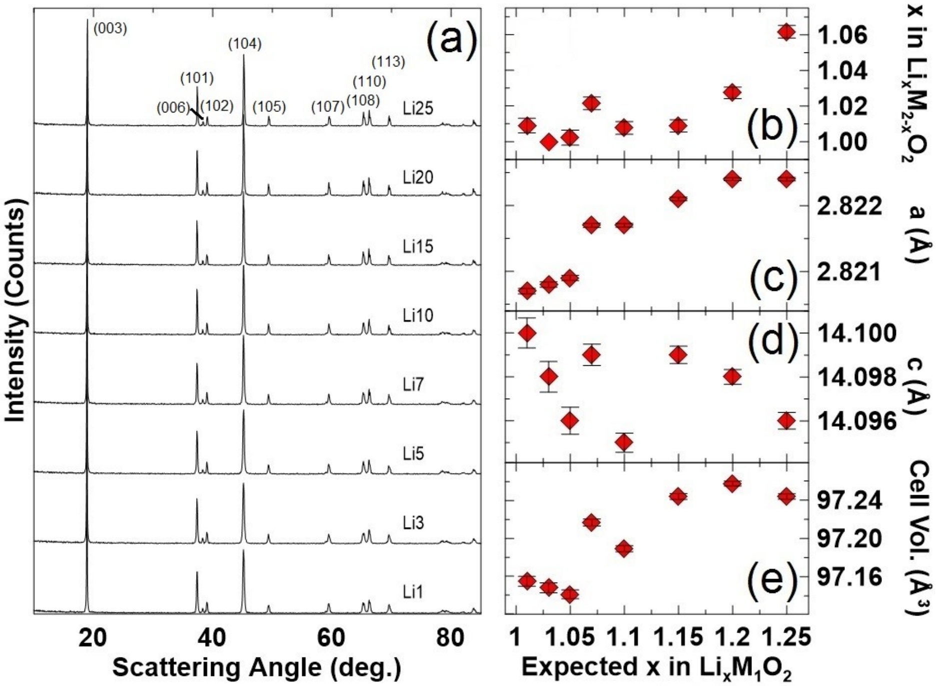

Figure 5.12: (a) XRD patterns (Cu Kα radiation) of CSTR samples, lithiated with varying amounts of Li, collected from 10°–85° along with reflections indexed in the $R\overline{3}m$ space group and Rietveld refinement data (Li content (b), lattice constants (c and d), and unit cell volume (e)) of the XRD patterns.

Li content was determined by allowing excess Li to migrate into the M layer. Li content determined from this method showed the same trend as results determined from ICP-OES, although values differed by as much as 0.023 (Li20 had a value of $Li_{1.050}$ from ICP-OES and $Li_{1.027}$ from Rietveld refinement). Given that Li is a weak scatterer of X-rays, it is believed that Li content determination by the Rietveld refinement method actually contained a higher degree of uncertainty than generated by the Rietica software. As seen in Fig. 5.12c-e, unit cell volume slightly increased with increasing Li content. This seems to stem from an increasing *a* lattice constant, as the *c* lattice constant decreased slightly.

Figure 5.13 shows the SEM images of the lithiated samples. Images were magnified at 10000x to closely examine the particles. For the most part, the morphology of the particles did not seem different. However, at higher lithium contents (Li20 and Li25), a different substance could be distinguished by a darker contrast. This unknown substance is expected to be a lithium-rich material, perhaps excess lithium carbonate that remained after the lithiation process.

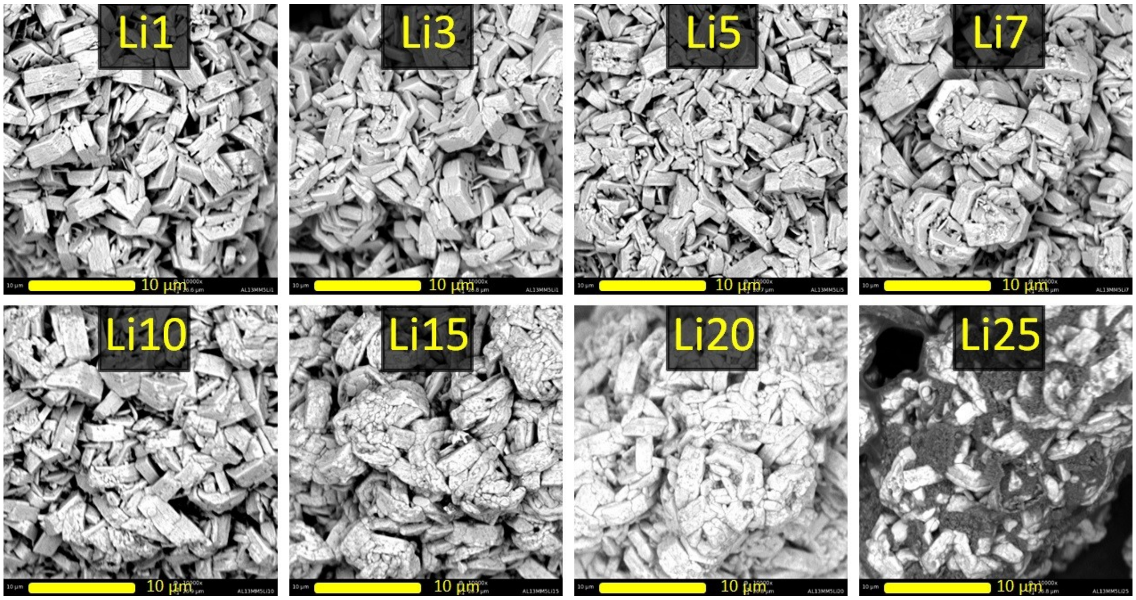

Figure 5.13: SEM images of CSTR samples lithiated with varying amounts of Li magnified at 10000x.

Electrochemical characterization of four samples (Li5, Li7, Li10, and Li15) was carried out (Sections 2.5-6). Figure 5.14 shows the voltage curves, differential capacity plots, and first cycle capacity data. Several of the cells showed an anomalous dq/dV bump around 4-4.3 V, which is denoted in Fig. 5.14 as either a black curve (Fig. 5.14a and b) or a black X symbol (Fig. 5.14c). Li5 did not have any cells which showed the dq/dV bump, and Li15 did not have any cells which did not show the bump.

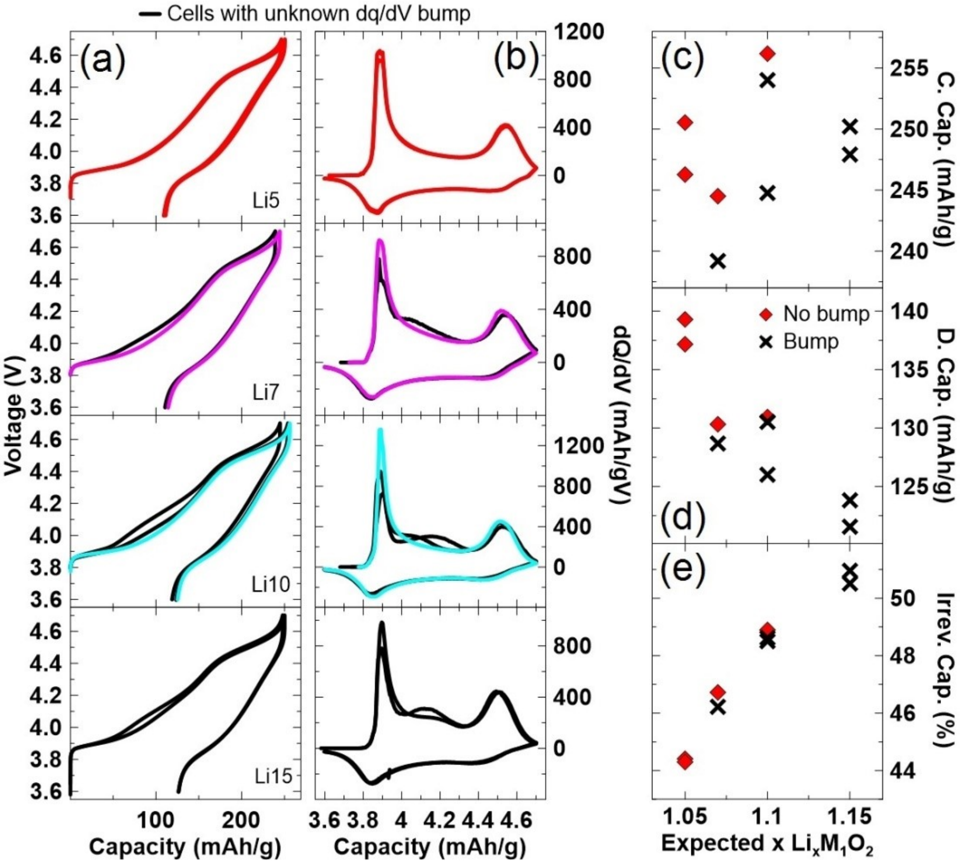

Figure 5.14: First cycle (a) cell voltage as a function of capacity, (b) dq/dV as a function of voltage, (c) charge capacity, (d) discharge capacity, and (e) irreversible capacity for MM5 cells prepared from CSTR samples of varying Li content. Cells were cycled between 3.6 V and 4.7 V at 30°C using a specific current of ~5 mA/g (C/50).

Fig. 5.14c shows that as samples were synthesized with more lithium, the first cycle charge capacity was unaffected and the discharge capacity decreased, increasing the irreversible capacity. Cells which showed the anomalous bump exhibited the same trends, although at a slightly decreased capacity upon both charge and discharge.

It is suspected that the source of the anomalous dq/dV bump is some impurity, likely stemming from the excess lithium carbonate used in the lithiation process. However, the dq/dV bump occurred over various voltages, hinting at a process that may be less definite than a single impurity. Additionally, if any unknown components were electrochemically inactive or even less active than the synthesized 5% Mg/Mn material, that may resolve the slightly decreased specific capacities observed from cells with the anomalous bump since that would not be accounted for when calculating the active mass.

Long term cycling performance (Section 2.6) was then characterized for these samples to see if the increase in lithium content, or cells with the anomalous dq/dV bump, affected cycling. The anomalous dq/dV bump did not reappear after the first cycle. Figure 5.15 shows the discharge capacity as well as ΔV at top of charge as a function of cycle number. The graphs on the left show data from individual cells, with an X symbol denoting cells showing the anomalous bump on the first cycle. The graphs on the right show average results of cells with different lithium content.

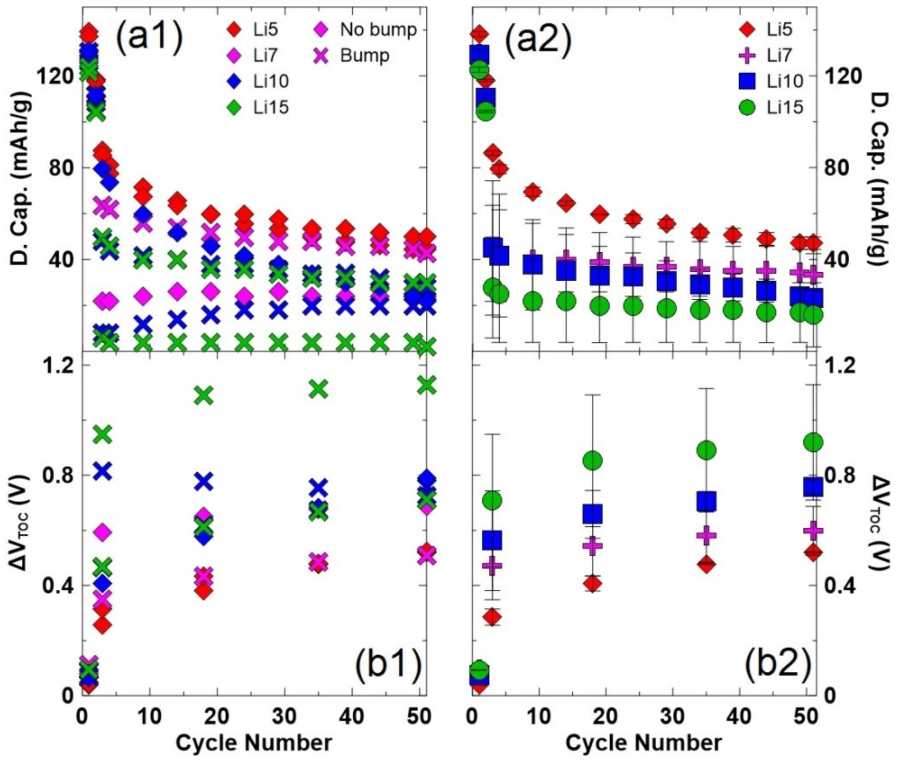

Figure 5.15: Discharge capacity (a) and ΔV_{TOC} (b) as a function of cycle number for MM5 cells prepared from CSTR samples of varying Li content. Graphs on the left show individual results (1), including a distinction of whether a dq/dV bump was observed during the first cycle, while the right shows average results (2). The data was collected at 30°C using a specific current of ~5 mA/g (C/50) for the first 2 cycles and ~50 mA/g (C/5) for all other cycles.

It was expected that all cells with the anomalous dq/dV bump would be affected in the same manner, so it was surprising to see that not all cells with the anomalous dq/dV bump cycled similarly when compared to cells without the bump. As seen in Fig. 5.15a1, Li10 cells with the bump had worse cycling performance than without the bump, but the Li7 cell with the bump cycled better than without the bump. ΔV_{TOC} data correlated well with cycling results, with cells that experience less resistance growth cycling better. Since the anomalous dq/dV bump only occurred during the first charge, it is possible that cell cycling performance was not strongly impacted by this bump.

Out of the cells in this study, Li5 cells cycled the best over 51 cycles. One Li7 cell retained a similar amount of capacity after 51 cycles, but the other did not perform as well. Cells with a higher Li content did not cycle as well as Li5 cells, and some cells exhibited a much larger capacity drop once a higher current rate was used (cycle 3 and after). The suspected presence of impurities, as discussed previously, likely contributed to the decrease in capacity in two possible ways. The first way would be if the impurities were electrochemically inactive or less active than the synthesized material. The second way would be if the impurity was less conductive than the synthesized material, then portions of the electrode material may not be fully delithiated before the cell voltage reached the upper cutoff voltage. It is unknown why certain cells experienced a large drop in capacity in the early cycles but recovered some of the capacity later on.

Average cycling data is shown in Fig. 5.15a2 and b2. The fluctuations within sets of cells containing more Li than Li5 made for large uncertainty, but all 3 sets of cells (Li7, Li10, and Li15) had worse cycling performance than Li5.

With this batch of 5% Mg/Mn sample synthesized by CSTR, increasing Li content, past a certain amount, resulted in the presence of impurities. Impurities were not discernable in XRD patterns, but were visible in SEM images (Fig. 5.13) with more Li than Li15. Coin cells with more Li than Li5 sometimes showed an anomalous dq/dV bump around 4-4.3 V, which seem to indicate the presence of impurities as well. Long term cycling performance for cells with more Li than Li5 were more irregular amongst the set of cells, and were generally cycling poorer than Li5 cells.

5.4 Effect of Cell Shorting During Fabrication

During the work of this thesis, the crimper used for coin cell fabrication (Section 2.5.2) sometimes malfunctioned and caused cell shorting during crimping. 0-5% Mg/Mn LCO/Li coin cells that were properly assembled generally had an open circuit voltage of around 3 V, but coin cells fabricated with the faulty crimper had open circuit voltages consistently below 2.2 V, with several even under 1.5 V. A voltmeter brought into the glove box confirmed that cell shorting occurred during the crimping process. While coin cell data (Section 2.6) using shorted cells were not included in this thesis (with the exception of the in situ XRD study of MM2 in Section 4.2.2), a trend was observed and this section will discuss the effects of cycling coin cells shorted during fabrication. This section will only discuss data from Ch. 3 and Ch. 4 cells that were shorted as a result of the fabrication process but were able to recover and cycle as programmed.

Figure 5.16 shows the 1st cycle cell voltage vs. capacity (a) and first cycle charge capacity vs. irreversible capacity (b) of 0% (1) and 5% (2) Mg/Mn cells that were shorted and not shorted. Shorted cells consistently had a larger first cycle capacity than non-shorted cells, and usually had a larger irreversible capacity as well (Fig. 5.9a). Fig. 5.16b demonstrates the inconsistency of shorted cells, as their spread was larger than non-shorted cells.

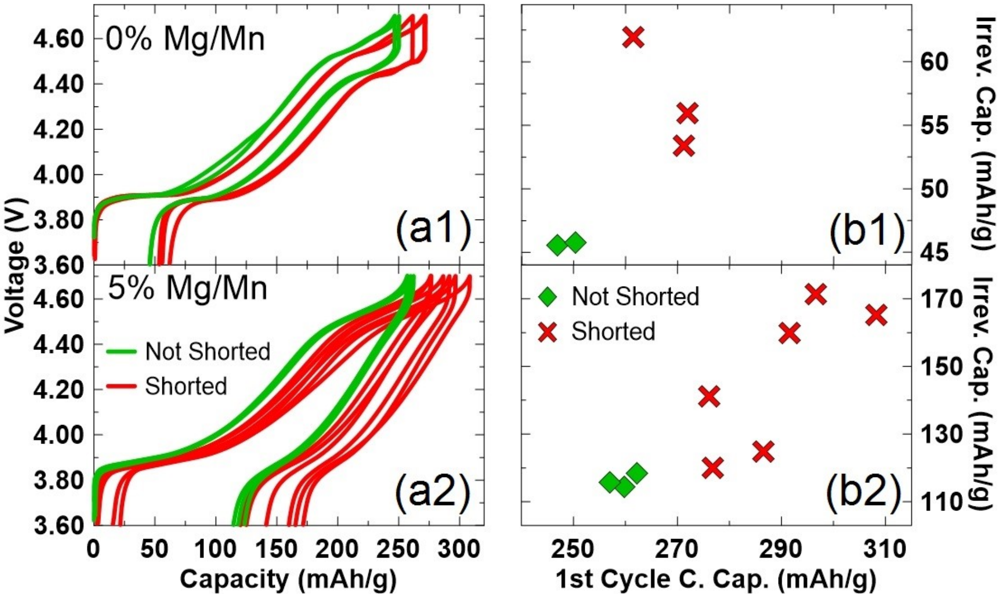

Figure 5.16: First cycle (a) cell voltage vs. capacity and (b) charge capacity vs. irreversible capacity for MM0 (1) and MM5 (2) shorted and non-shorted cells cycled between 3.6 V and 4.7 V. The data was collected at 30°C using a specific current of ~5 mA/g (C/50).

When cells are shorted, electrons and Li ions flow into the positive electrode, increasing the Li content in the positive electrode. This may be similar to the situation discussed earlier with cells prepared from oxidized precursors (Section 5.2) and may be able to explain the increase in first cycle charge capacity. Shorting the cells also introduced another uncontrolled variable, and the decrease in consistency can be seen in Fig. 5.16b.

Figure 5.17 shows discharge capacity (a) and ΔV at top of charge (b) as a function of cycle number for MM0 (1) and MM5 (2) shorted and non-shorted cells. Only two of the shorted MM5 cells were programmed for long term cycling. The cycling performance (Fig. 5.17a) of shorted cells was worse than non-shorted cells for MM5 cells but was slightly better for MM0 cells. ΔV_{TOC} data (Fig. 5.17b) agreed with cycling performance, with shorted MM0 cells having similar or slightly lower ΔV_{TOC} than non-shorted cells and shorted MM5 cells having higher ΔVs.

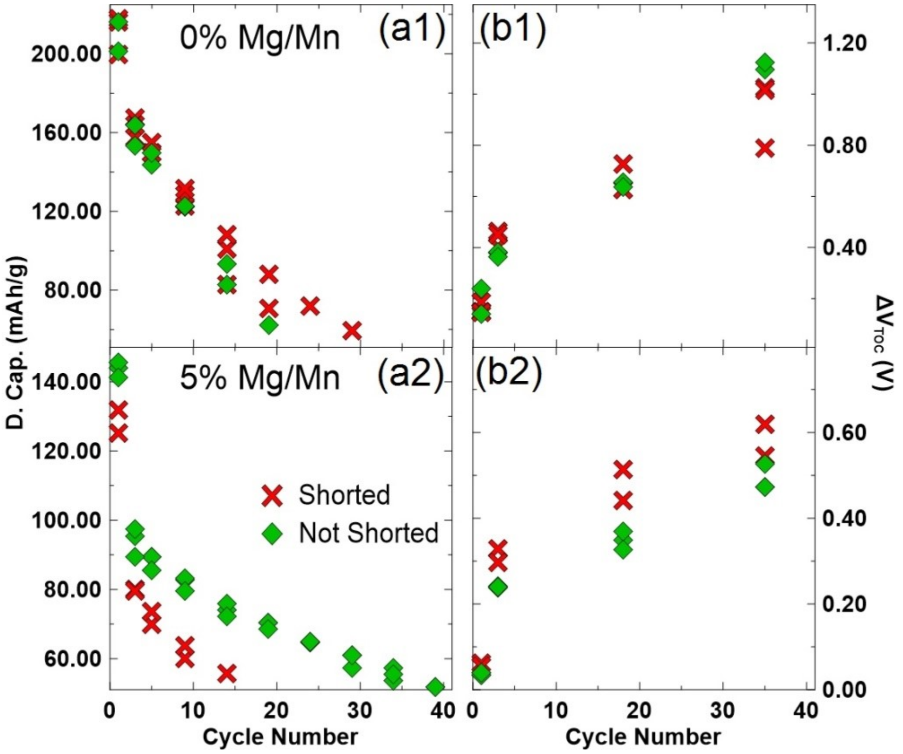

Figure 5.17: Discharge capacity (a) and ΔV_{TOC} (b) as a function of cycle number for shorted and non-shorted LCO cells with (1) 0% and (2) 5% Mg/Mn. The data was collected at 30°C using a specific current of ~5 mA/g (C/50) for the first 2 cycles and ~50 mA/g (C/5) for all other cycles

The impact of shorted cells on cycling performance was different for MM0 and MM5 cells. For MM5 cells, the cycling performance of the shorted cells was distinctly worse, while the shorted MM0 cells cycled similarly, or even perhaps slightly better than non-shorted cells. ΔV_{TOC} results showed similar trends. This may suggest that cell shorting is affected by Mg/Mn content, but more research is required before drawing conclusions. The duration and extent of cell shorting were not measured, and it is unknown whether the crimper shorted cells in a consistent manner or not. It is uncertain why the cycling performance of shorted 0% Mg/Mn cells was not negatively affected, even though both shorted MM0 and shorted MM5 cells showed larger first cycle charge and irreversible capacities (Fig. 5.16).

While any data from cells that experienced shorting were already omitted in the work of this thesis (with the exception of Section 4.2.2), this study gave even more justification for the omission. Shorted cells showed a larger 1st cycle charge capacity but more irreversible capacity as well as less consistency (Figs. 5.16). It is also unknown how much impact cell shorting will have on the cycling performance of cells, as shorted 5% Mg/Mn cells cycled noticeably worse, but shorted 0% Mg/Mn cells had similar, if not slightly better, cycling performance (Fig. 5.17). This unquantified impact introduces more uncertainty, warranting omission of shorted cell data.

Chapter 6 – Conclusions and Future Work

From the studies done in Chapters 3-5, there were various insights gained and lessons learned. This chapter will first summarize the conclusions about the synthesis of materials used in this work (Section 6.1), then the effects of Mg/Mn doping in the electrochemical performance of LCO will be reviewed (Section 6.2), and finally the various directions that future work can go to build on this work will be discussed (Section 6.3)

6.1 Materials Synthesis

Several methods were evaluated in Chapter 5 to synthesize Mg/Mn doped LCO. Co-precipitation under N_2 atmosphere, as described in 2.1, was the chosen method to prepare the electrode materials required in this work. This method fully incorporated the dopants into the structure, unlike the solid state route which resulted in the presence of an MgO phase (Section 5.1.1). Precursors synthesized using this method remained single phased with the $Co(OH)_2$ structure, unlike co-precipitation in air which resulted in the oxidation of some precursor material to Co(OOH) and Co_3O_4 phases (Sections 5.1.2). Since the degree and distribution of precursor oxidation was unknown, lithiated materials prepared from these oxidized precursors, as well as coin cells fabricated from these lithiated materials, produced results with questionable consistency (Sections 5.1.2 and 5.2). Cells containing electrode material prepared from precursors co-precipitated under N_2 produced more reliable data, as long as the cells were not shorted during the fabrication process (Section 5.4). A trial run with the continuously stirred tank reactor (CSTR) was also carried out to investigate synthesis in a more controlled manner

(Section 5.1.3). SEM images showed the materials from CSTR synthesis had a much narrower size distribution and XRD patterns were similar to those of their counterparts prepared as described in Section 2.1.

A series of $Co_{1-2x}Mg_xMn_x(OH)_2$ ($0 \leq x \leq 0.05$) precursor materials was synthesized according to the selected method above, from which $LiCo_{1-2x}Mg_xMn_xO_2$ ($0 \leq x \leq 0.05$) samples were prepared and characterized by ICP-OES, XRD, and SEM. For the most part, metal atomic ratios as determined by ICP-OES were very close to the calculated expected ratios for both precursor and lithiated samples (Sections 3.1.1 and 3.2.1). Discrepancies between measured and expected ratios for the lithiated samples were attributed to lithium loss during the heating step. XRD analyses showed the expansion of both the precursor and lithiated material unit cell as the Mg/Mn content increased (Sections 3.1.2 and 3.2.2), which was expected due to the average sizes of ions involved. For the most part, SEM images showed small precursor particles, which then aggregated and clustered together during lithiation. 4% Mg/Mn precursor particles were larger than the other Mg/Mn contents when co-precipitated as described in Section 2.1.1, but this was attributed to certain reaction conditions as the 5% Mg/Mn co-precipitated in the CSTR (Section 2.1.3) also formed as larger particles.

6.2 Effects of Mg/Mn Doping in LCO on Electrochemical Performance

In cycling coin cells prepared from the series of $LiCo_{1-2x}Mg_xMn_xO_2$ ($0 \leq x \leq 0.05$) electrode materials, it was found that increasing the Mg/Mn content slightly increased the 1st charge capacity, decreased the 1st discharge capacity, and increased the 1st cycle irreversible capacity (Section 3.3.1). Analysis of dq/dV as a function of voltage showed a broadening of the peak corresponding to the insulator-metal transition as the Mg/Mn content increased and the disappearance of the peaks corresponding to the order-disorder transition after 1% Mg/Mn. As the Mg/Mn content increased, the pair of peaks corresponding to the O3 to O6 to O1 phase transitions were converted to a single broad peak. A comparison of the first two cycles refuted the possibility of electrolyte decomposition and supported the likelihood of oxygen loss being the main consequence of increasing Mg/Mn content (Section 3.3.2). The incorporation of even just 1% Mg/Mn into the LCO material significantly improved the cycling performance to 4.7 V and suppressed the growth of cell resistance, but further increases in Mg/Mn content did not compound these improvements and those cells cycled similarly to 1% Mg/Mn (Section 3.3.3).

Further studies suggested that the first cycle charge and discharge capacities of the materials with 0% and 5% Mg/Mn started to differentiate at 4.5 V, which was where the broad dq/dV peak likely corresponding to oxygen loss began to occur (Section 4.1.1). However, improvements to cycling performance imparted by 5% Mg/Mn were not realized until cycling to an upper cutoff voltage of 4.7 V (Section 4.1.3). In situ XRD experiments showed clearly the gradual suppression of the O3-O6-O1 phase transitions at high voltage as the Mg/Mn content increased (Section 4.2). The oxygen loss mechanism is believed to have caused this suppression, as it might lock CoO_2 slabs in place and prevent the shift from O3 to O6 to O1. Mg/Mn substitution was shown to cause an irreversible structural change upon the first charge to 4.7 V, and this restricted the range of unit cell variation after (Section 4.2.4). However, observation of the O3-O6 phase transition in 2% Mg/Mn indicated that the improved cycling performance imparted by

Mg/Mn substitution (Fig. 3.15) was not related to the volume changes associated with these phase transitions (Fig. 4.18).

Mg/Mn doping in LCO was shown to improve cycling performance at 4.7 V, but at a cost of lower reversible capacity during the first cycle. The cause of this improved cycling performance was not due to the suppression of the O3-O6-O1 phase transitions at high voltage, but due to the suppression of cell resistance growth during cycling. While these materials are not suitable for use in commercial lithium ion batteries as is, this work contributed to understanding high voltage cycling and its difficulties. This understanding will aid in the design of future high voltage lithium ion batteries.

6.3 Future work

In this work, it was shown that as Mg/Mn content increased, the O3-O6-O1 phase transitions at high voltage were gradually supplanted by another mechanism, likely oxygen loss (Section 3.3.2). While oxygen loss can explain the suppression of the O3-O6-O1 phase transitions as well as the irreversible structure change caused by the first charge and subsequent restriction of unit cell variation for cells with 2% and 5% Mg/Mn (Section 4.2), it is uncertain whether oxygen loss is the only mechanism contributing to these developments. Mg migration into the Li layer, if confirmed, may also be a factor. While previous studies have reported no Mg migration when cycling Mg doped LCO,[37,85] Rietveld refinement of the 5% Mg/Mn in situ XRD experiment (Fig 4.16) showed the inconclusive possibility of Mg occupation in the Li layer. The results were inconclusive due to an insufficient number of peaks scanned, leading to refinement instability and Mg occupations that were sometimes not physically possible. More thorough scans of the electrode at various stages of cycling may allow Rietveld refinement to accurately determine Mg occupation in the Li layer. Additionally, O occupancy may also be investigated from these scans to confirm the loss of oxygen during the first charge.

The improvements to cycling performance at 4.7 V in Mg/Mn doped LCO were through the suppression of cell resistance growth during cycling (Fig. 3.15). The mechanism of this resistance growth and how Mg/Mn doping suppresses this growth is still uncertain. Analyzing cells after the completion of cycling may yield more insights. ICP-OES may be used to determine if there are differences in Co dissolution.[29,30,34,37,65] Another end-of-life analysis technique is X-ray photoelectron spectroscopy (XPS), which can probe the thickness and chemical composition differences of the electrode SEI.[145–148] Understanding this resistance-growth mechanism may help steer future studies towards the appropriate approach in high voltage cycling.

This work focused on the effects of Mg/Mn in LCO and did not include known protocols to improve high voltage cycling. Some of these protocols include the optimization of particle properties through the control of reaction conditions afforded by the use of the CSTR,[105,106,108] positive electrode surface coatings,[24,26,37–39,66,141] and appropriate selection of electrolytes and electrolyte additives.[13,15–17,39] Recent work frequently coupled Mg doping with coating of the electrode material,[37–39] and a well-designed cell will certainly see a dramatically improved performance compared to the performance of the coin cells in this work.

There has been a widespread desire to decrease the amount of Co in lithium ion batteries, for cost[45,46] and sourcing[44,45] reasons, by utilizing other positive electrode materials such as NMC and NCA. There has been some work on Mg doping in NMC[95–97] and NCA[60,98–100] with NCA studies in particular also showing less unit cell variation[60] and requiring just 1% Mg to improve cycling performance.[100] However, to the best of the author's knowledge, no studies have investigated the long term cycling performance of these materials at high voltage as this work did for LCO. Further work may reveal whether Mg/Mn doping affects these materials in the same way as LCO is affected at high voltage.

References

(1) United States Department of Energy. *EV Everywhere Grand Challenge Blueprint*; Office of Energy Efficiency and Renewable Energy (EERE), 2013.

(2) United States Department of Energy. *FY 2014 Annual Progress Report - Energy Storage R&D*; 2015.

(3) EVVA. Panasonic NCR18650G 3600mAh Li-ion Battery Cell. http://www.evva-tech.com/plus/view.php?aid=111&tid=27 (accessed May 17, 2017).

(4) Reddy, T. B. *Linden's Handbook of Batteries*; 4th Ed. McGraw-Hill, 2011.

(5) McKinsey & Company. *Electrifying insights: How automakers can drive electrified vehicle sales and profitability*; Advanced Industries, 2017.

(6) Nelson, P. A.; Ahmed, S.; Gallagher, K. G.; Dees, D. W. *J. Power Sources* **2015**, *283*, 506–516.

(7) Streetinsider.com. UBS Sees Telsa's (TSLA) Model 3 As Unprofitable. https://www.streetinsider.com/Analyst+Comments/UBS+Sees+Telsas+%28TSLA%29+Model+3+As+Unprofitable/11540932.html?si_client=st (accessed May 16, 2017).

(8) Tesla. Tesla | Model S, Tesla | Model 3. https://www.tesla.com/en_CA (accessed May 17, 2017).

(9) Google Maps. Halifax, Nova Scotia. https://www.google.ca/maps/place/Sir+James+Dunn+Bldg,+Halifax,+NS+B3H+4J5/@44.6378192,-65.8346514,7z/data=!4m5!3m4!1s0x4b5a222447b85cc7:0x94d7687d7bdb38f2!8m2!3d44.6378279!4d-63.5934248 (accessed May 18, 2017).

(10) Peled, E. *J. Electrochem. Soc.* **1979**, *126*, 2047–2051.

(11) Fong, R.; von Sacken, U.; Dahn, J. R. *J. Electrochem. Soc.* **1990**, *137*, 2009–2013.

(12) Peled, E.; Golodnitsky, D.; Ardel, G. *J. Electrochem. Soc.* **1997**, *144*, L208–L210.

(13) Zuo, X.; Fan, C.; Xiao, X.; Liu, J.; Nan, J. *J. Power Sources* **2012**, *219*, 94–99.

(14) Nie, M.; Chalasani, D.; Abraham, D. P.; Chen, Y.; Bose, A.; Lucht, B. L. *J. Phys. Chem. C* **2013**, *117*, 1257–1267.

(15) Hu, M.; Pang, X.; Zhou, Z. *J. Power Sources* **2013**, *237*, 229–242.

(16) Xu, K. *Chem. Rev.* **2014**, *114*, 11503–11618.

(17) Xia, J.; Nelson, K. J.; Lu, Z.; Dahn, J. R. *J. Power Sources* **2016**, *329*, 387–397.

(18) Mizushima, K.; Jones, P. C.; Wiseman, P. J.; Goodenough, J. B. *Mater. Res. Bull.* **1980**, *15*, 783–789.

(19) Goodenough, J. B.; Mizushima, K. Electrochemical Cell with New Fast Ion Conductors. US4302518, 1981.

(20) Ozawa, K. *Solid State Ionics* **1994**, *69*, 212–221.

(21) Pillot, C. The Rechargeable Battery Market and Main Trends 2015-2025. Presented at the the 18th International Meeting on Lithium Batteries, Chicago, USA, 2016.

(22) Orman, H. J.; Wiseman, P. J. *Acta Crystallogr. Sect. C Cryst. Struct. Commun.* **1984**, *40*, 12–14.

(23) Tukamoto, H.; West, A. R. *J. Electrochem. Soc.* **1997**, *144*, 3164–3168.

(24) Cho, J.; Kim, G. *Electrochem. solid-state Lett.* **1999**, *2*, 253-255.

(25) Chen, Z.; Dahn, J. R. *Electrochem. Solid-State Lett.* **2004**, *7*, A11–A14.

(26) Chen, Z.; Dahn, J. R. *Electrochim. Acta* **2004**, *49*, 1079–1090.

(27) Zou, M.; Yoshio, M.; Gopukumar, S.; Yamaki, J. I. *Electrochem. Solid State Lett.* **2004**, *7*, A176–A179.

(28) Xia, H.; Lu, L.; Meng, Y. S.; Ceder, G. *J. Electrochem. Soc.* **2007**, *154*, A337–A342.

(29) Takahashi, Y.; Tode, S.; Kinoshita, A.; Fujimoto, H.; Nakane, I.; Fujitani, S. *J. Electrochem. Soc.* **2008**, *155*, A537–A541.

(30) Sun, Y. K.; Yoon, C. S.; Myung, S. T.; Belharouak, I.; Amine, K. *J. Electrochem. Soc.* **2009**, *156*, A1005–A1010.

(31) Valanarasu, S.; Chandramohan, R.; Thirumalai, J.; Vijayan, T. A.; Srikumar, S. R.; Mahalingam, T. *J. Mater. Sci. Mater. Electron.* **2010**, *21*, 827–832.

(32) Lee, J. N.; Han, G. B.; Ryou, M. H.; Lee, D. J.; Song, J. C.; Choi, J. W.; Park, J. K. *Electrochim. Acta* **2011**, *56*, 5195–5200.

(33) Yin, R. Z.; Kim, Y. S.; Shin, S. J.; Jung, I.; Kim, J. S.; Jeong, S. K. *J. Electrochem. Soc.* **2012**, *159*, A253–A258.

(34) Li, X.; Liu, J.; Meng, X.; Tang, Y.; Banis, M. N.; Yang, J.; Hu, Y.; Li, R.; Cai, M.; Sun, X. *J. Power Sources* **2014**, *247*, 57–69.

(35) Guan, T.; Zuo, P.; Sun, S.; Du, C.; Zhang, L.; Cui, Y.; Yang, L.; Gao, Y.; Yin, G.; Wang, F. *J. Power Sources* **2014**, *268*, 816–823.

(36) Fathi, R.; Burns, J. C.; Stevens, D. A.; Ye, H.; Hu, C.; Jain, G.; Scott, E.; Schmidt, C.; Dahn, J. R. *J. Electrochem. Soc.* **2014**, *161*, A1572–A1579.

(37) Wang, Z.; Wang, Z.; Guo, H.; Peng, W.; Li, X. *Ceram. Int.* **2015**, *41*, 469–474.

(38) Shim, J. H.; Lee, J. H.; Han, S. Y.; Lee, S. H. *Electrochim. Acta* **2015**, *186*, 201–208.

(39) Shim, J. H.; Han, J. M.; Lee, J. H.; Lee, S. H. *ACS Appl. Mater. Interfaces* **2016**, *8*, 12205–12210.

(40) Zou, M.; Yoshio, M.; Gopukumar, S.; Yamaki, J. I. *Chem. Mater.* **2003**, *15*, 4699–4702.

(41) Wang, Z.; Wang, Z.; Peng, W.; Guo, H.; Li, X.; Wang, J.; Qi, A. *Ionics (Kiel).* **2014**, *20*, 1525–1534.

(42) MacNeil, D. D.; Dahn, J. R. *J. Electrochem. Soc.* **2002**, *149*, A912–A919.

(43) MacNeil, D. D.; Lu, Z.; Chen, Z.; Dahn, J. R. *J. Power Sources* **2002**, *108*, 8–14.

(44) Amnesty International. *“This is what we die for”: Human rights abuses in the Democratic Republic of the Congo power the global trade in cobalt*; AFR 62/3183/2016, 2016.

(45) United States Geological Survey. *Mineral Commodity Summaries 2017*; 2017.

(46) InfoMine. Commodity and Metal Prices http://www.infomine.com/investment/metal-prices/ (accessed May 20, 2017).

(47) Ohzuku, T.; Kitagawa, M.; Hirai, T. *J. Electrochem. Soc.* **1990**, *137*, 769–775.

(48) Geller, S.; Durand, J. L. *Acta Cryst.* **1960**, *13*, 325–331.

(49) Julien, C.; Mauger, A.; Zaghib, K.; Groult, H. *Inorganics* **2014**, *2*, 132–154.

(50) Ohzuku, T.; Makimura, Y. *Chem. Lett.* **2001**, *30*, 642–643.

(51) Lu, Z.; MacNeil, D. D.; Dahn, J. R. *Electrochem. Solid-State Lett.* **2001**, *4*, A200–A203.

(52) MacNeil, D. D.; Lu, Z.; Dahn, J. R. *J. Electrochem. Soc.* **2002**, *149*, A1332.

(53) Rozier, P.; Tarascon, J. M. *J. Electrochem. Soc.* **2015**, *162*, A2490–A2499.

(54) Li, J. Study and Development of Layered Li-Ni-Mn-Co Oxide Positive Electrode Materials for Lithium Ion Batteries. PhD Thesis, Dalhousie University, 2016.

(55) Pouillerie, C.; Croguennec, L.; Biensan, P.; Willmann, P.; Delmas, C. *J. Electrochem. Soc.* **2000**, *147*, 2061–2069.

(56) Pouillerie, C.; Croguennec, L.; Delmas, C. *Solid State Ionics* **2000**, *132*, 15–29.

(57) Pouillerie, C.; Perton, F.; Biensan, P.; Pérès, J. P.; Broussely, M.; Delmas, C. *J. Power Sources* **2001**, *96*, 293–302.

(58) Madhavi, S.; Rao, G. V. S.; Chowdari, B. V. R.; Li, S. F. Y. *J. Power Sources* **2001**, *93*, 156–162.

(59) Chen, C. H.; Liu, J.; Stoll, M. E.; Henriksen, G.; Vissers, D. R.; Amine, K. *J. Power Sources* **2004**, *128*, 278–285.

(60) Sasaki, T.; Godbole, V.; Takeuchi, Y.; Ukyo, Y.; Novák, P. *J. Electrochem. Soc.* **2011**, *158*, A1214–A1219.

(61) Lee, M. J.; Lee, S.; Oh, P.; Kim, Y.; Cho, J. *Nano Lett.* **2014**, *14*, 993–999.

(62) National Petroleum Council. *Advancing Technology for America's Transportation Future*; 2012.

(63) Vertiv. *The Emergence of Lithium Ion Batteries Within the Data Center*; SL-24692, 2017.

(64) Padhi, A. K.; Nanjundaswamy, K. S.; Goodenough, J. B. *J. Electrochem. Soc.* **1997**, *144*, 1188–1194.

(65) Amatucci, G. G.; Tarascon, J. M.; Klein, L. C. *Solid State Ionics* **1996**, *83*, 167–173.

(66) Wang, Z.; Wu, C.; Liu, L.; Wu, F.; Chen, L.; Huang, X. *J. Electrochem. Soc.* **2002**, *149*, A466--A471.

(67) Ueda, A.; Ohzuku, T. *J. Electrochem. Soc.* **1994**, *141*, 2972.

(68) Amatucci, G. G.; Tarascon, J. M.; Klein, L. C. *J. Electrochem. Soc.* **1996**, *143*, 1114–1123.

(69) Li, B.; Wang, Y.; Lin, H.; Liu, J.; Xing, L.; Xu, M.; Li, W. *Electrochim. Acta* **2014**, *141*, 263–270.

(70) Kim, Y. J.; Cho, J.; Kim, T. J.; Park, B. *J. Electrochem. Soc.* **2003**, *150*, A1723–A1725.

(71) Reimers, J. N.; Dahn, J. R. *J. Electrochem. Soc.* **1992**, *139*, 2091–2907.

(72) Chen, Z.; Lu, Z.; Dahn, J. R. *J. Electrochem. Soc.* **2002**, *149*, A1604–A1609.

(73) Van der Ven, A.; Aydinol, M. K.; Ceder, G. *J. Electrochem. Soc.* **1998**, *145*, 2149–2155.

(74) Van der Ven, A.; Aydinol, M. K.; Ceder, G.; Kresse, G.; Hafner, J. *Phys. Rev. B* **1998**, *58*, 2975–2987.

(75) Cho, J.; Lee, J. G.; Kim, B.; Park, B. *Chem. Mater.* **2003**, *15*, 3190–3193.

(76) Kim, J.; Noh, M.; Cho, J.; Kim, H.; Kim, K. B. *J. Electrochem. Soc.* **2005**, *152*, A1142–A1148.

(77) Hu, G.; Cao, J.; Peng, Z.; Cao, Y.; Du, K. *Electrochim. Acta* **2014**, *149*, 49–55.

(78) Abe, K.; Hattori, T.; Kawabe, K.; Ushigoe, Y.; Yoshitake, H. *J. Electrochem. Soc.* **2007**, *154*, A810–A815.

(79) Abe, K.; Miyoshi, K.; Hattori, T.; Ushigoe, Y.; Yoshitake, H. *J. Power Sources* **2008**, *184*, 449–455.

(80) Wu, B.; Ren, Y.; Mu, D.; Liu, X.; Yang, G.; Wu, F. *RSC Adv.* **2014**, *4*, 10196–10203.

(81) Yang, J.; Zhao, P.; Shang, Y.; Wang, L.; He, X.; Fang, M.; Wang, J. *Electrochim. Acta* **2014**, *121*, 264–269.

(82) Xia, L.; Xia, Y.; Liu, Z. *Electrochim. Acta* **2015**, *151*, 429–436.

(83) Wang, X.; Xing, L.; Liao, X.; Chen, X.; Huang, W.; Yu, Q.; Xu, M.; Huang, Q.; Li, W. *Electrochim. Acta* **2015**, *173*, 804–811.

(84) Zhao, M.; Zuo, X.; Ma, X.; Xiao, X.; Yu, L.; Nan, J. *J. Power Sources* **2016**, *323*, 29–36.

(85) Levasseur, S.; Ménétrier, M.; Delmas, C. *J. Power Sources* **2002**, *112*, 419–427.

(86) Luo, W.; Li, X.; Dahn, J. R. *J. Electrochem. Soc.* **2010**, *157*, A782–A790.

(87) Luo, W.; Li, X.; Dahn, J. R. *J. Electrochem. Soc.* **2010**, *157*, A993–A1001.

(88) Reddy, M. V.; Jie, T. W.; Jafta, C. J.; Ozoemena, K. I.; Mathe, M. K.; Nair, A. S.; Peng, S. S.; Idris, M. S.; Balakrishna, G.; Ezema, F. I.; Chowdari, B. V. R. *Electrochim. Acta* **2014**, *128*, 192–197.

(89) Cheng, J. H.; Pan, C. J.; Nithya, C.; Thirunakaran, R.; Gopukumar, S.; Chen, C. H.; Lee, J. F.; Chen, J. M.; Sivashanmugam, A.; Hwang, B. J. *J. Power Sources* **2014**, *252*, 292–297.

(90) Myung, S. T.; Kumagai, N.; Komaba, S.; Chung, H. T. *Solid State Ionics* **2001**, *139*, 47–56.

(91) Kim, H. S.; Ko, T. K.; Na, B. K.; Cho, W. Il; Chao, B. W. *J. Power Sources* **2004**, *138*, 232–239.

(92) Holzapfel, M.; Strobel, P.; Wright, J.; Morcrette, M.; Chappel, E.; Anne, M. *J. Mater. Chem.* **2004**, *14*, 94–101.

(93) Needham, S. A.; Wang, G.; Liu, H.; Drozd, V. A.; Liu, R. S. *J. Power Sources* **2007**, *174*, 828–831.

(94) Valanarasu, S.; Chandramohan, R. *Cryst. Res. Technol.* **2010**, *45*, 835–839.

(95) Luo, W.; Zhou, F.; Zhao, X.; Lu, Z.; Li, X.; Dahn, J. R. *Chem. Mater.* **2010**, *22*, 1164–1172.

(96) Luo, W.; Li, X.; Dahn, J. R. *Chem. Mater.* **2010**, *22*, 5065–5073.

(97) Huang, Z.; Li, X.; Liang, Y.; He, Z.; Chen, H.; Wang, Z.; Guo, H. *Solid State Ionics* **2015**, *282*, 88–94.

(98) Muto, S.; Tatsumi, K.; Kojima, Y.; Oka, H.; Kondo, H.; Horibuchi, K.; Ukyo, Y. *J. Power Sources* **2012**, *205*, 449–455.

(99) Tavakoli, A. H.; Kondo, H.; Ukyo, Y.; Navrotsky, A. *J. Electrochem. Soc.* **2013**, *160*, A302–A305.

(100) Huang, B.; Li, X.; Wang, Z.; Guo, H.; Xiong, X. *Ceram. Int.* **2014**, *40*, 13223–13230.

(101) Santana, J. A.; Kim, J.; Kent, P. R. C.; Reboredo, F. A. *J. Chem. Phys.* **2014**, *141*, 164706.

(102) Yoshio, M.; Brodd, R. J.; Kozawa, A. *Lithium-Ion Batteries: Science and Technologies*; Springer Science & Business Media, 2009.

(103) Lee, K. S.; Myung, S. T.; Moon, J. S.; Sun, Y. K. *Electrochim. Acta* **2008**, *53*, 6033–6037.

(104) Zhou, F.; Zhao, X.; van Bommel, A.; Rowe, A. W.; Dahn, J. R. *Chem. Mater.* **2010**, *22*, 1015–1021.

(105) van Bommel, A.; Dahn, J. R. *J. Electrochem. Soc.* **2009**, *156*, A362–A365.

(106) van Bommel, A.; Dahn, J. R. *Chem. Mater.* **2009**, *21*, 1500–1503.

(107) van Bommel, A. Lithium-rich Transition Metal Oxides as Positive Electrode Materials in Lithium-ion Batteries. PhD Thesis, Dalhousie University, 2010.

(108) Camardese, J.; Abarbanel, D.; McCalla, E.; Dahn, J. R. *J. Electrochem. Soc.* **2014**, *161*, A890–A895.

(109) Camardese, J. Core-Shell Materials as Positive Electrodes in Lithium-Ion Batteries. PhD Thesis, Dalhousie University, 2015.

(110) Boss, C. B.; Fredeen, K. J. *Concepts, Instrumentation and Techniques in Inductively Coupled Plasma Optical Emission Spectrometry*; 3rd Ed. PerkinElmer Life and Analytical Sciences, 2004.

(111) Brundle, C. R.; Evans, C. A.; Wilson, S. *Encyclopedia of Materials Characterization*; Butterworth-Heinemann, 1992.

(112) Cullity, B. D.; Stock, S. R. *Elements of X-Ray Diffraction*; 3rd Ed. Prentice Hall, 2001.

(113) Warren, B. E. *X-Ray Diffraction*; Dover Ed. Dover Publications, 1990.

(114) Rietveld, H. M. *J. Appl. Crystallogr.* **1969**, *2*, 65–71.

(115) Kriegner, D.; Matej, Z.; Kuzel, R.; Holy, V. *J. Appl. Crystallogr.* **2015**, *48*, 613–618.

(116) Widjonarko, N. *Coatings* **2016**, *6*, 54.

(117) National Institute of Standards and Technology. X-Ray Form Factor, Attenuation, and Scattering Tables. https://www.nist.gov/pml/x-ray-form-factor-attenuation-and-scattering-tables (accessed Apr 27, 2017).

(118) Brett A Hunter. *Rietica for Windows*; Version 2.1, 2007.

(119) Hunter, B. A. *Int. Union Crystallogr. Comm. Powder Diffr. Newsl.* **1998**, *20*, 21.

(120) Brett A Hunter, CJ Howard. *A Computer Program for Rietveld Analysis of X-Ray and Neutron Powder Diffraction Patterns*; Australian Nuclear Science and Technology Organization, 2000.

(121) Crystal Impact. *Match!*; Version 1.11h, 2013.

(122) The International Centre for Diffraction Data. ICDD Products - PDF-4+. http://www.icdd.com/products/pdf4.htm (accessed Apr 28, 2017).

(123) Wyckoff, R. W. G. *Crystals Structures*; Interscience Publishers, 1958.

(124) Peng, L.-M.; Ren, G.; Dudarev, S. L.; Whelan, M. J. *Acta Crystallogr. Sect. A Found. Crystallogr.* **1996**, *52*, 456–470.

(125) Yang, J.; Liu, H.; Martens, W. N.; Frost, R. L. *J. Phys. Chem. C* **2010**, *114*, 111–119.

(126) Toby, B. H. *Powder Diffr.* **2006**, *21*, 67–70.

(127) Skoog, D. A.; Holler, F. J.; Crouch, S. R. *Principles of Instrumental Analysis*; 6th Ed. Brooks/Cole, 2007.

(128) Marks, T.; Trussler, S.; Smith, A. J.; Xiong, D.; Dahn, J. R. *J. Electrochem. Soc.* **2011**, *158*, A51–A57.

(129) Glazier, S. Investigating Disordered Positive Electrode Materials for Lithium-Ion Batteries With Li(1+x)Ti2xFe(1-3x)O2. MSc Thesis, Dalhousie University, 2015.

(130) Li, J.; Shunmugasundaram, R.; Doig, R.; Dahn, J. R. *Chem. Mater.* **2016**, *28*, 162–171.

(131) RB Von Dreele, AC Larson. *General Structure Analysis System*; 2001.

(132) Toby, B. H. *J. Appl. Crystallogr.* **2001**, *34*, 210–213.

(133) Shannon, R. D. *Acta Crystallogr. Sect. A* **1976**, *32*, 751–767.

(134) Selwyn, L. S.; McKinnon, W. R.; Dahn, J. R.; Le Page, Y. *Phys. Rev. B* **1986**, *33*, 6405–6414.

(135) Reimers, J. N.; Dahn, J. R. *J. Electrochem. Soc.* **1993**, *140*, 2752–2754.

(136) Saubanère, M.; McCalla, E.; Tarascon, J. M.; Doublet, M. L. *Energy Environ. Sci.* **2016**, *9*, 984–991.

(137) Seo, D. H.; Lee, J. H.; Urban, A.; Malik, R.; Kang, S. Y.; Ceder, G. *Nat. Chem.* **2016**, *8*, 692–697.

(138) McCalla, E.; Abakumov, A. M.; Saubanere, M.; Foix, D.; Berg, E. J.; Rousse, G.; Doublet, M. L.; Gonbeau, D.; Novak, P.; Van Tendeloo, G.; Dominko, R.; Tarascon, J. M. *Science* **2015**, *350*, 1516–1521.

(139) Lu, Z.; Dahn, J. R. *J. Electrochem. Soc.* **2002**, *149*, A815–A822.

(140) Choi, J.; Manthiram, A. *Electrochem. Solid-State Lett.* **2005**, *8*, C102–C105.

(141) Chen, Z.; Qin, Y.; Amine, K.; Sun, Y. K. *J. Mater. Chem.* **2010**, *20*, 7606–7612.

(142) Butel, M.; Gautier, L.; Delmas, C. *Solid State Ionics* **1999**, *122*, 271–284.

(143) Liu, Z.; Ma, R.; Osada, M.; Takada, K.; Sasaki, T. *J. Am. Chem. Soc.* **2005**, *127*, 13869–13874.

(144) Levasseur, S.; Ménétrier, M.; Shao-Horn, Y.; Gautier, L.; Audemer, A.; Demazeau, G.; Largeteau, A.; Delmas, C. *Chem. Mater.* **2003**, *15* (1), 348–354.

(145) Madec, L.; Xia, J.; Petibon, R.; Nelson, K. J.; Sun, J. P.; Hill, I. G.; Dahn, J. R. *J. Phys. Chem. C* **2014**, *118*, 29608–29622.

(146) Madec, L.; Petibon, R.; Xia, J.; Sun, J. P.; Hill, I. G.; Dahn, J. R. *J. Electrochem. Soc.* **2015**, *162*, A2635–A2645.

(147) Madec, L.; Petibon, R.; Tasaki, K.; Xia, J.; Sun, J. P.; Hill, I. G.; Dahn, J. R. *Phys. Chem. Chem. Phys.* **2015**, *17*, 27062–27076.

(148) Madec, L.; Ma, L.; Nelson, K. J.; Petibon, R.; Sun, J. P.; Hill, I. G.; Dahn, J. R. *J. Electrochem. Soc.* **2016**, *163*, A1001–A1009.

Appendix A – Precursor XRD Patterns with Refinements of Sample Displacement

Table A.1: Rietveld refinement results for precursor XRD patterns with refinements of sample displacement. While the refinements generated large sample displacements for MM0p, MM1p and MM3p, nothing unusual was noted during sample preparation.

Sample	***a* (Å)**	***c* (Å)**	**Vol. (Å^3)**	**Sample Displacement (mm)**	**R$_{\text{Bragg}}$**
MM0p	3.1829	4.6487	40.786	-0.351	2.97
MM1p	3.1803	4.6474	40.708	-0.189	2.28
MM2p	3.1796	4.6472	40.688	-0.001	2.01
MM3p	3.1816	4.6522	40.783	-0.259	2.05
MM4p	3.1795	4.6527	40.734	-0.038	3.03
MM5p	3.1818	4.657	40.830	-0.039	4.15

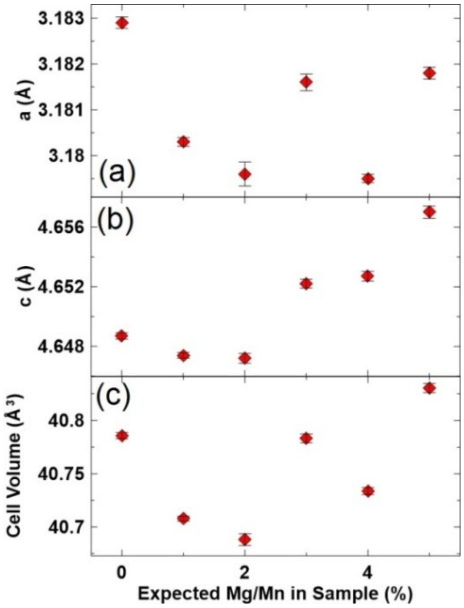

Figure A.1: Lattice constants (panels a and b), obtained from Rietveld refinements of XRD patterns of precursor samples collected, and unit cell volume (c) calculated from the lattice constants. Refinements of sample displacement were included with these refinements.

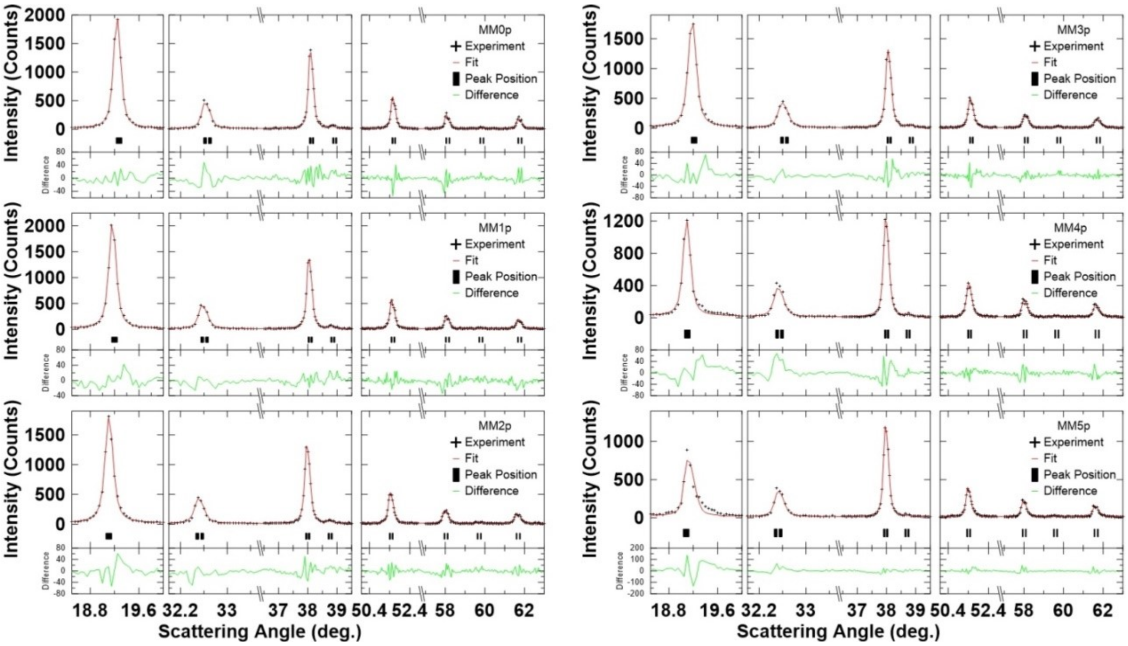

Figure A.2: XRD Rietveld refinement pattern fitting for precursor materials. Only selected reflections are shown in this figure. Refinements of sample displacement were included with these refinements.

Appendix B – Rietveld Refinement Results for In Situ XRD Experiments

Table B.1: Rietveld refinement results for in situ XRD study of MM0. Lattice parameters reported in this table have been converted to the O3 unit cell.

Scan	Phase 1	Phase Scale Factor	a (Å) (± 0.0006 Å)	c (Å) (± 0.0003 Å)	O6 Phase	Phase Scale Factor	a (Å) (± 0.0003 Å)	c (Å) (± 0.002 Å)	Unused Phase	Phase Scale Factor	R_{Bragg}
1	O3	7.26E-06	2.8181	14.0696	N/A				No	N/A	3.30
2	O3	7.36E-06	2.8177	14.0828	N/A				No	N/A	3.84
4	O3	7.38E-06	2.8174	14.1041	N/A				No	N/A	3.10
6	O3	4.36E-06	2.8136	14.1950	N/A				Yes	3.03E-06	2.41
8	O3	5.64E-06	2.8137	14.2281	N/A				Yes	1.71E-06	2.47
10	O3	6.43E-06	2.8125	14.2693	N/A				Yes	1.01E-06	1.81
12	O3	7.10E-06	2.8121	14.3168	N/A				Yes	4.43E-07	2.00
14	O3	7.26E-06	2.8115	14.3695	N/A				Yes	3.64E-07	2.52
16	M	2.55E-04	2.8114	14.4118	N/A				Yes	5.85E-07	2.59
18	M	2.51E-04	2.8114	14.4448	N/A				Yes	6.89E-07	2.65
20	O3	6.85E-06	2.8104	14.4487	N/A				Yes	5.92E-07	5.45
22	O3	7.07E-06	2.8098	14.4215	N/A				Yes	5.15E-07	4.75
24	O3	7.16E-06	2.8098	14.3523	N/A				Yes	4.13E-07	4.66
26	O3	6.05E-06	2.8124	14.2141	N/A				Yes	1.07E-06	4.64
27	O3	6.60E-06	2.8142	14.1015	O6	8.20E-07	2.8158	13.6775	Yes	3.31E-08	3.56
28	O3	2.69E-06	2.8202	14.0494	O6	2.44E-06	2.8086	13.6448	Yes	1.60E-06	1.43
29	N/A				O6	4.45E-06	2.8028	13.6315	Yes	1.36E-06	1.18
30	N/A				O6	5.99E-06	2.8176	13.4924	Yes	6.90E-07	1.71
31	N/A				O6	6.74E-06	2.8226	13.4479	Yes	4.38E-07	1.84
32	N/A				O6	7.09E-06	2.8244	13.4683	Yes	2.66E-07	2.43
33	N/A				O6	6.85E-06	2.8255	13.4935	Yes	3.82E-07	2.43
34	N/A				O6	6.02E-06	2.8241	13.5779	Yes	2.70E-07	2.02
35	O3	3.50E-07	2.8190	14.2290	O6	6.51E-06	2.8148	13.6093	Yes	3.44E-07	2.43
36	O3	1.05E-06	2.8173	14.3351	O6	5.75E-06	2.8105	13.6340	Yes	3.91E-07	1.62
37	O3	2.58E-06	2.8164	14.3486	O6	4.54E-06	2.8063	13.6369	Yes	2.02E-07	0.79
38	O3	4.57E-06	2.8135	14.3774	O6	2.67E-06	2.8080	13.6449	Yes	1.81E-07	0.96
40	O3	6.01E-06	2.8109	14.4051	O6	4.42E-07	2.8067	13.6605	Yes	2.46E-07	2.56
42	O3	6.74E-06	2.8117	14.4223	N/A				Yes	1.41E-07	2.69
44	M	2.58E-04	2.8113	14.4054	N/A				Yes	9.96E-08	1.29
46	O3	6.79E-06	2.8108	14.3807	N/A				Yes	2.53E-07	3.47
48	O3	6.96E-06	2.8106	14.3323	N/A				Yes	1.18E-07	2.43
50	O3	6.59E-06	2.8114	14.2734	N/A				Yes	1.03E-07	2.20
52	O3	6.76E-06	2.8121	14.2197	N/A				No	N/A	2.35
54	O3	7.34E-06	2.8133	14.1769	N/A				No	N/A	1.98
56	O3	7.16E-06	2.8142	14.1164	N/A				No	N/A	1.85
58	O3	7.06E-06	2.8162	14.0842	N/A				No	N/A	2.31
60	O3	6.99E-06	2.8173	14.1051	N/A				No	N/A	2.57
62	O3	7.15E-06	2.8168	14.1507	N/A				No	N/A	1.72
64	O3	7.25E-06	2.8143	14.2054	N/A				No	N/A	2.18
66	O3	7.06E-06	2.8143	14.2553	N/A				Yes	5.42E-08	1.79
68	O3	7.14E-06	2.8135	14.3082	N/A				Yes	4.62E-08	1.64
70	O3	7.30E-06	2.8128	14.3614	N/A				Yes	4.03E-08	4.25
72	M	2.61E-04	2.8126	14.3960	N/A				Yes	1.42E-07	1.86
74	O3	7.06E-06	2.8117	14.4107	N/A				Yes	2.16E-07	3.62
76	O3	7.07E-06	2.8115	14.4072	N/A				Yes	3.24E-07	3.94
78	O3	7.20E-06	2.8113	14.3698	N/A				Yes	1.47E-07	3.39
80	O3	7.09E-06	2.8108	14.2477	N/A				Yes	6.47E-08	1.31
82	O3	4.97E-06	2.8167	14.1516	O6	3.15E-06	2.8067	13.6916	Yes	1.34E-08	1.94
83	O3	2.85E-06	2.8179	14.0488	O6	4.47E-06	2.8061	13.6620	Yes	1.51E-07	1.62
84	N/A				O6	6.11E-06	2.8127	13.6105	Yes	2.01E-07	1.24

Table B.2: Rietveld refinement results for in situ XRD study of MM2. Lattice parameters reported in this table have been converted to the O3 unit cell.

Scan	**Phase 1**	**Phase Scale Factor**	**a (Å) (± 0.0005 Å)**	**c (Å) (± 0.007 Å)**	**O6 Phase**	**Phase Scale Factor**	**a (Å) (± 0.001 Å)**	**c (Å) (± 0.02 Å)**	**Unused Phase**	**Phase Scale Factor**	**R_{Bragg}**
1	O3	6.71E-06	2.8187	14.070	N/A				No	N/A	4.93
3	O3	6.93E-06	2.8179	14.071	N/A				No	N/A	4.47
6	O3	7.00E-06	2.8181	14.086	N/A				No	N/A	4.34
9	O3	5.27E-06	2.8150	14.140	N/A				Yes	2.71E-06	2.81
12	O3	5.54E-06	2.8145	14.207	N/A				Yes	2.71E-06	2.31
15	O3	5.76E-06	2.8127	14.310	N/A				Yes	3.51E-06	5.34
18	O3	5.75E-06	2.8105	14.394	N/A				Yes	3.51E-06	4.77
21	O3	5.94E-06	2.8101	14.432	N/A				Yes	3.35E-06	4.86
24	O3	5.91E-06	2.8100	14.430	N/A				Yes	3.19E-06	5.41
27	O3	6.16E-06	2.8112	14.348	N/A				Yes	3.04E-06	4.03
30	O3	6.17E-06	2.8155	14.203	N/A				Yes	2.73E-06	3.72
31	O3	9.59E-06	2.8170	14.116	N/A				No	N/A	2.65
32	O3	9.08E-06	2.8173	14.089	N/A				No	N/A	2.92
33	O3	7.99E-06	2.8175	14.090	O6	1.97E-06	2.811	13.54	No	N/A	2.14
34	O3	7.18E-06	2.8169	14.094	O6	2.02E-06	2.813	13.52	No	N/A	2.45
35	O3	6.72E-06	2.8163	14.089	O6	2.63E-06	2.818	13.51	No	N/A	2.40
36	O3	5.66E-06	2.8149	14.079	O6	3.47E-06	2.819	13.38	No	N/A	1.62
37	O3	5.08E-06	2.8148	14.091	O6	4.52E-06	2.818	13.41	No	N/A	1.60
38	O3	4.51E-06	2.8152	14.129	O6	5.25E-06	2.819	13.56	No	N/A	1.09
39	O3	2.39E-06	2.8134	14.255	O6	6.81E-06	2.815	13.72	Yes	3.60E-06	1.41
40	O3	3.62E-06	2.8137	14.302	O6	5.80E-06	2.813	13.75	Yes	3.39E-06	0.96
41	O3	3.94E-06	2.8156	14.328	O6	3.43E-06	2.810	13.74	Yes	3.25E-06	1.52
42	O3	4.76E-06	2.8131	14.355	N/A				Yes	3.24E-06	3.61
45	O3	5.77E-06	2.8123	14.363	N/A				Yes	2.67E-06	3.99
48	O3	6.43E-06	2.8134	14.296	N/A				Yes	2.41E-06	5.15
51	O3	6.90E-06	2.8153	14.229	N/A				Yes	1.69E-06	3.72
53	O3	6.93E-06	2.8157	14.175	N/A				Yes	1.83E-06	3.39
55	O3	6.24E-06	2.8153	14.174	N/A				Yes	2.54E-06	3.66
58	O3	7.42E-06	2.8146	14.212	N/A				Yes	1.26E-06	2.78
61	O3	7.06E-06	2.8139	14.289	N/A				Yes	1.93E-06	4.01
64	O3	6.74E-06	2.8123	14.350	N/A				Yes	2.37E-06	4.28
67	O3	6.60E-06	2.8124	14.347	N/A				Yes	2.33E-06	3.87
70	O3	6.74E-06	2.8140	14.272	N/A				Yes	2.06E-06	4.12
73	O3	6.41E-06	2.8173	14.161	O6	3.95E-06	2.811	13.38	No	N/A	1.80
74	O3	5.98E-06	2.8174	14.134	O6	5.50E-06	2.812	13.37	No	N/A	1.91
75	O3	5.41E-06	2.8177	14.136	O6	6.57E-06	2.812	13.40	No	N/A	2.40
76	O3	4.96E-06	2.8174	14.144	O6	7.75E-06	2.812	13.43	No	N/A	1.77

Table B.3: Rietveld refinement results for in situ XRD study of MM5.

Scan	Phase 1	Phase Scale Factor	a (Å) (± 0.0003 Å)	c (Å) (± 0.003 Å)	Phase 2	Phase Scale Factor	a (Å)	c (Å)	Unused Phase	Phase Scale Factor	R_{Bragg}
1	O3	7.88E-06	2.8180	14.083	N/A				No	N/A	3.86
2	O3	7.99E-06	2.8174	14.093	N/A				No	N/A	4.21
4	O3	7.57E-06	2.8171	14.120	N/A				No	N/A	3.57
6	O3	7.37E-06	2.8164	14.156	N/A				No	N/A	2.92
8	O3	7.72E-06	2.8154	14.214	N/A				No	N/A	3.42
10	O3	8.02E-06	2.8129	14.286	N/A				No	N/A	3.27
12	O3	1.06E-05	2.8108	14.355	N/A				Yes	1.36E-08	0.84
14	O3	1.05E-05	2.8095	14.395	N/A				Yes	1.41E-08	0.28
16	O3	1.05E-05	2.8080	14.405	N/A				Yes	1.46E-08	0.73
18	O3	1.05E-05	2.8080	14.381	N/A				Yes	1.36E-08	0.74
20	O3	1.04E-05	2.8098	14.303	N/A				Yes	1.12E-08	1.17
21	O3	1.03E-05	2.8113	14.247	N/A				Yes	4.84E-09	1.27
22	O3	1.03E-05	2.8122	14.194	N/A				Yes	3.71E-10	1.45
23	O3	1.00E-05	2.8134	14.152	N/A				Yes	8.9E-10	1.35
24	O3	1.07E-05	2.8141	14.113	N/A				No	N/A	2.65
25	O3	9.90E-06	2.8137	14.121	N/A				No	N/A	2.90
27	O3	9.27E-06	2.8129	14.244	N/A				No	N/A	3.15
29	O3	9.53E-06	2.8114	14.301	N/A				No	N/A	3.28
31	O3	9.71E-06	2.8111	14.294	N/A				No	N/A	3.18
33	O3	1.04E-05	2.8118	14.252	N/A				No	N/A	3.42
35	O3	1.08E-05	2.8128	14.216	N/A				No	N/A	4.00
37	O3	1.01E-05	2.8145	14.184	N/A				No	N/A	3.85
39	O3	1.02E-05	2.8144	14.189	N/A				No	N/A	4.20
41	O3	1.03E-05	2.8131	14.224	N/A				No	N/A	4.23
43	O3	1.04E-05	2.8122	14.270	N/A				No	N/A	3.97
45	O3	1.02E-05	2.8113	14.306	N/A				No	N/A	3.05
47	O3	1.03E-05	2.8106	14.297	N/A				No	N/A	2.65
49	O3	1.01E-05	2.8115	14.236	N/A				No	N/A	2.94
50	O3	9.84E-06	2.8122	14.185	N/A				No	N/A	2.27
51	O3	9.51E-06	2.8133	14.149	N/A				No	N/A	2.94
52	O3	9.45E-06	2.8137	14.117	N/A				No	N/A	2.58